Spectrometers based on Kinetic Inductance Detectors

Usasi Chowdhury

THÈSE

Pour obtenir le grade de

DOCTEUR DE L'UNIVERSITÉ GRENOBLE ALPES

École doctorale : PHYS - Physique
Spécialité : Nanophysique
Unité de recherche : Institut Néel

Spectromètres basés sur des détecteurs à inductance cinétique

Spectrometers based on Kinetic Inductance Detectors

Présentée par :

Usasi CHOWDHURY

Direction de thèse :

Alessandro MONFARDINI DIRECTEUR DE RECHERCHE, CNRS DELEGATION ALPES	Directeur de thèse
Florence LEVY-BERTRAND CHARGEE DE RECHERCHE, Université Grenoble Alpes	Co-encadrante de thèse
Martino CALVO	Co-encadrant de thèse

Rapporteurs :

FAOUZI M. BOUSSAHA
INGENIEUR DE RECHERCHE HDR, OBSERVATOIRE DE PARIS
CLAIRE MARRACHE-KIKUCHI
MAITRESSE DE CONFERENCES HDR, UNIVERSITE PARIS-SACLAY

Thèse soutenue publiquement le **13 novembre 2023**, devant le jury composé de :

FAOUZI M. BOUSSAHA INGENIEUR DE RECHERCHE HDR, OBSERVATOIRE DE PARIS	Rapporteur
CLAIRE MARRACHE-KIKUCHI MAITRESSE DE CONFERENCES HDR, UNIVERSITE PARIS-SACLAY	Rapporteure
MICHEL PIAT PROFESSEUR DES UNIVERSITES, UNIVERSITE PARIS CITE	Examinateur
FRANÇOIS-XAVIER DESERT ASTRONOME, UNIVERSITE GRENOBLE ALPES	Examinateur
HERVE GEOFFRAY DOCTEUR EN SCIENCES, CNES TOULOUSE	Examinateur
KLAUS HASSELBACH DIRECTEUR DE RECHERCHE, CNRS DELEGATION ALPES	Président

Spectrometers based on Kinetic Inductance Detectors

Usasi Chowdhury

Supervisors

Alessandro Monfardini
Florence Levy-Bertrand
Martino Calvo

Reporters

Faouzi M. Boussaha
Claire Marrache-Kikuchi

Jury Members

Klaus Hasselbach
François-Xavier Désert
Michel Piat
Herve Geoffray

Doctoral Thesis, L'université Grenoble Alpes, 2023

Contents

Acknowledgements

To all women before me who have sacrificed everything to live a decent life

I extend my deepest thanks to Alessandro Monfardini, Florence Levy Bertrand, and Martino Calvo for allowing me into your professional lives over the past three years. I consider myself fortunate to have been under your guidance. Everything I have been able to accomplish, I attribute to you. Thank you very much. Alessandro and Martino, you have taught me everything I know about KIDs, mm-wave astronomy, cleanroom, cryogenics, French administration, Italian cuisine, sports and almost everything around... I thank you. Florence, I thank you for assisting me from the initial interview to overcoming the hurdles of visa approval and securing a scholarship for my initial three-month stay. You have taught me to be strong, consistent, organized and proud of myself (I am still working on it). I thank you all for being there as a source of comfort during moments of stress, handling tantrums, and supporting me through mental breakdowns and celebrating with me during my happy moments.

I would like to thank Johannes Goupy for the lessons and tips in the clean room and for your grand presence whenever you were around and Gregory Greg for bringing all the mechanical designs to life.

Thank you to the reporters, Faouzi M. Boussaha and Claire Marrache-Kikouchi, and the Jury members Francois-Xavier DeSERT, Herve GEOFFRAY, Michel PIAT, and Klaus HASSELBACH.

Thanks to the establishments Neel Institut and the cleanroom, PTA in CEA and Nanofab in CNRS for letting me work.

My heartfelt thanks go to my parents, Ma and Baba, for their sacrifices and lessons on resilience. Ma, your selfless sacrifices and enduring pains for others have been a profound source of inspiration for me. Baba, your insistence on finding joy even after disappointments has reminded me that life is worth living in every circumstance.

To Bor Thakuma and Ranga Thakuma, I owe my gratitude for instilling in me the values of discipline, integrity, and independence. My brother, Dico, your consistent efforts to anticipate Didi's needs have helped me get to where I am today.

A special thanks goes to Shyamal Da for your unwavering belief, to Neru for being a comforting presence during moments of vulnerability, and to Julien (Felix) and your family for simply being there, sharing life and introducing me to the world of French songs with your voice.

Thanks to Julien (Boumy) for always being a supportive friend. To Daniele, Sofia, and Matteo, you made my third year bearable, and your genuine friendship has shown me the

depth of human connections. Thanks, Daniele, for your willingness (I hope!!!) to listen to everything.

I am grateful to those individuals whose brief presence in my life left lasting impressions, teaching me valuable lessons about what truly matters. Asha Mam, thank you for creating a space where vulnerability is embraced, and Debasree Di, your courage to be authentic has been a continuous source of motivation. Sangeeta, your role in helping me love myself is immeasurable, and for that, I am sincerely thankful. And Euphemie, your unwavering determination to pursue dreams with a strong mindset has inspired me throughout my second and third years.

I had lost hope in life at some point on my way. Doing the thesis was the only meaning for life, nothing else. I waited for years, hoping to write Dr. as a title. But in the end, my thesis has given me more meaning than a salutation. And everyone on this long journey (four years of desperation and three years of thesis) has been a part of every cell I am today. In closing, I extend my deepest gratitude to everyone mentioned (or not mentioned) and those who have contributed to my academic and personal growth. Each of you has played a unique part in shaping my journey, and for that, I am truly blessed.

Chapter 1
Introduction

Understanding the intricate processes in the universe requires specific observations which corresponds to various detection techniques. This thesis primarily focuses on the development of a detector that has future aspirations in the millimeter-wave astronomical studies. In this chapter, we will provide an introduction to some basic areas in millimeter-wave astronomy that are of particular interest to our research group. Next, we will describe in short detail the working principles of the different detectors used for mm-wavelength observations. We will give a short, general motivation for working on the device described in this thesis.

1.1 mm wave Astronomy

Most astronomical objects, including galaxies, molecular clouds, star–forming regions, protostars, evolved stars, planets, and comets radiate in all part of the electromagnetic spectrum from radio waves to gamma-rays which correspond to a variety of continuous and discrete (emission and absorption) processes. The millimeter-wave frequency range (0.3 to 1.7 mm) serves as a crucial tool useful for studying the vast, cold gas clouds. Stars form at the centre of such giant gravitationally unstable molecular clouds. Either the cloud slowly condenses or collapses, the dense, hot core of the star forms and begins gathering dust and gas. Along with star, planets, asteroids, comets, dust are also produced in the same process. An assembly of hundreds of billions of stars with the ISM, pulled together by gravity creates a galaxy. Small dust particles with sizes ranging from a few nm to a fraction of micrometer are ubiquitous in the interstellar medium. A fraction of the stellar radiation in the UV-optical range from young stars are absorbed by dusty interstellar medium (ISM) and re-emitted in far-infrared and observed in the (sub)millimetre wavelength [Lagache et al., 2005]. The emissions from the cosmos have usually three primary components:

- Thermal emission from dust
- Emission from ionized gas via thermal free-free mechanisms
- Emission resulting from charged particles moving through magnetic fields, known as non thermal synchrotron emission

A short description of these processes is given in the following:

Thermal emission The spectrum emitted by a perfect black body can be described by Planck's law of thermal radiation. The Wein's displacement law,

$$\lambda_{peak} T = 2.898 \times 10^{-3} \qquad [\text{ in m.K}] \tag{1.1}$$

relates the temperature (T, in K) with the peak wavelength (λ_{peak}, in m) of the blackbody spectrum at which the object radiates the most. The thermal dust emission is used to trace the structure and physical conditions of ISM, especially in connection with star formation (SF). The targets range from a galactic diffuse medium and local molecular clouds to full galaxies. Studies of millimeter and submillimeter emissions from the Milky Way and nearby galaxies indicate that around 90% of dust is extremely cold (between 14-16 K) and can be a valuable tool for probing molecular hydrogen [Misiriotis et al., 2006]. Fig. 1.1 shows the map of pure dust emission observed for NGC6946 spiral galaxy in the NIKA2 1.15 mm [CO (2-1) line] and 2 mm bands [Ejlali et al., 2022].

Free-free radiation Charged particles, even if not bound, are accelerated by the ions' Coulomb force in the presence of the ionized gas in the interstellar medium. As the charged particle is free and in local thermal equilibrium before and after the interaction, the continuum radiation is referred as free-free radiation or thermal bremsstrahlung ("braking radiation"). This radiation traces the charged particle's temperature, density and ionized volume.

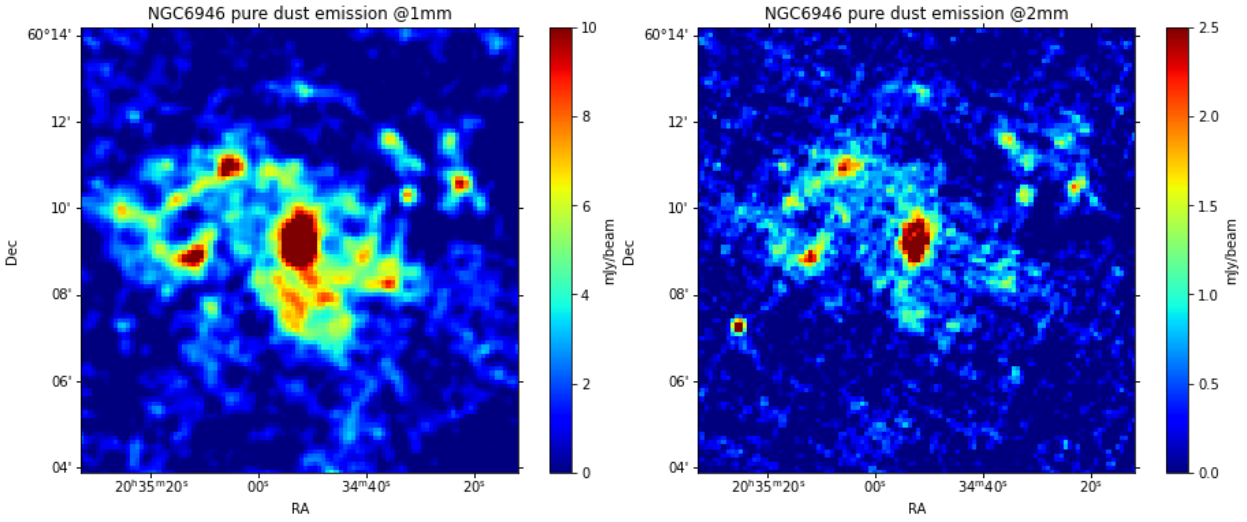

Figure 1.1: Pure dust emission of the galaxy NGC6946 at 1mm (left) and 2mm (right) at angular resolution of 18".[Ejlali et al., 2022]

Nonthermal Emission-Synchrotron Cosmic ray electrons are deflected in the presence of galactic magnetic fields and emit so-called synchrotron radiation. The process, in this case, is non-thermal because the energy distribution of the particles does not follow a Maxwellian

distribution. Rather, each particle has its own characteristic frequency. This kind of radiation is associated with, for example, the active galactic nuclei (AGN).
Fig. 1.2 describes the percentage of thermal radiation due to the dust particles, thermal free-free emission from the ionized gas and synchrotron emission from the NGC 491 edge-on galaxy for characteristic wavelengths in the spectral range between 1 mm and 2 cm. As shown in Fig. 1.2, the presence of thermal radiation is more prevalent in the nearby galaxies at 1-3 mm wavelength than other phenomena. For example, in this galaxy, the synchrotron emission dominates from 5 mm onwards.

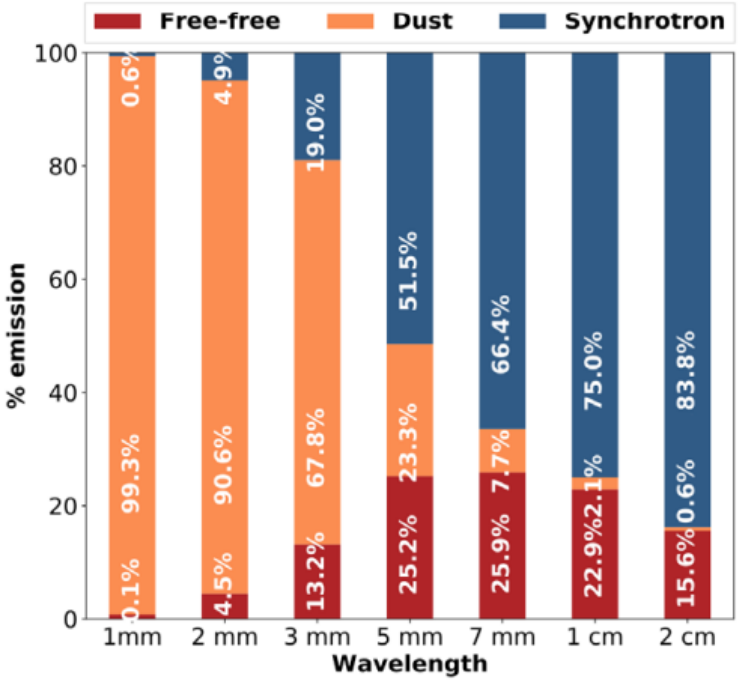

Figure 1.2: Continuum mm-wave radiation distribution in NGC 491 as observed by NIKA2 and other instruments. [Katsioli, S. et al., 2022]

Line emission The emission lines are produced by molecules relaxing from higher to lower rotational energy levels. There are more than 120 known species of ionized and neutral molecular gases in the interstellar medium [Herbst, 2001]. The detection of spectral lines, specific to the molecular rotation or the atomic fine-structure transition is used to diagnose the physical conditions of the sources. Their rest frequencies identify the specific atoms and molecules involved and the detection of lines allows the determination of the redshift and the distance to cosmological sources.
For example, carbon monoxide (CO) exhibits different rotation levels of emission lines in the rest-frame frequencies of 115 GHz (J=1-0), 230 GHz (J = 2-1) and 345 GHz (J= 3-2) corresponding to 2.6, 1.3, 0.9 mm [Gillespie, 1980]. Fig. 1.3 shows the spectrum for the CO-brightest point of NGC 253 galaxy measured by the Deep Spectroscopic High-redshift Mapper (DESHIMA). DESHIMA is the first on-chip mm-wave spectrometer used for astronomical ob-

servations in 2018 and has inspired the work presented in this manuscript.

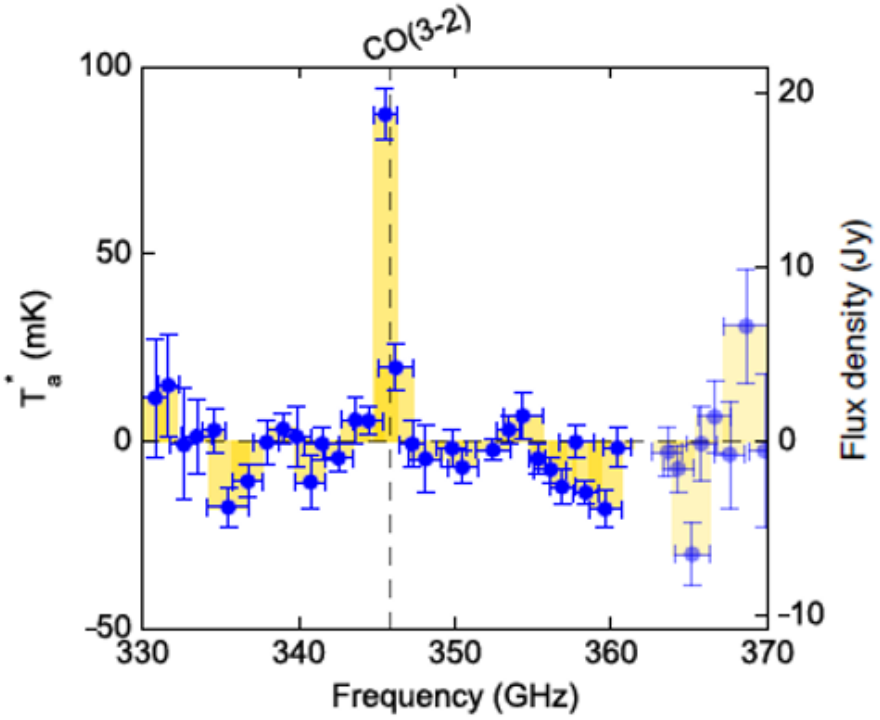

Figure 1.3: The CO (J=3-2) line for NGC 253 based on aperture photometry with DESHIMA [Endo et al., 2019]

Redshifted galaxies The widely accepted ΛCDM (Lambda Cold Dark Matter) model, which is the standard framework for cosmological studies, characterizes the current universe as 13.8 billion years old from the point of the Big Bang. The universe has been undergoing expansion since then and on a cosmological scale, it displays homogeneity. This expansion results in the radiation emitted by celestial objects undergoing a phenomenon where their radiation wavelength is lengthened. For very distant galaxies, the effects of curved space cause the wavelengths of light to be increasingly red-shifted as the distance to Earth increases. Thus a redshift (z) in the spectral response of a monochromatic source gives an equivalence of how stretched the observed wavelength (λ_{obs}) from that source (in rest frame, λ_{res}) is given by,

$$1 + z = \frac{\lambda_{obs}}{\lambda_{res}} \tag{1.2}$$

The Hubble law, $v = H_0 d$ gives the distance d in the expanding universe, once the recessional velocity v and the Hubble parameter H have been independently measured and calibrated. The spectral energy distribution (SED) of the high-z galaxies due to the redshift is an increasing function of the observed frequency, however the emission declines with the inverse of the luminosity distance. Thus the detectable flux-density remains approximately constant with

increasing redshift for z>1, compared to the radio or optical counterparts [Blain and Longair, 1993]. This allows us to detect highly redshifted galaxies comparatively easily at longer wavelengths.

Cosmic Microwave Background and cosmology Cosmic microwave background (CMB) radiation is an isotropic relic radiation with an intensity wavelength and temperature of 1.5 mm and 2.73 K as shown in Fig. 1.4 [Fixsen, 2009]. It is largely uniform across the sky, with significant residuals in the background that provide a kind of imprinting of the universe back 13.7 billion years ago [Smoot, 2007]. Among many interesting features, the Sunyaev Zeldovich (SZ) effect, a change in the apparent brightness of CMB [Sunyaev and Zel'Dovich, 1980], which is caused by the scattering of the CMB photons as they interact with the hot plasma in the clusters of galaxies or the B-mode polarisation pattern [Starobinskii, 1979] are CMB anisotropies. They provide valuable information about the early universe. Improved measurements of the CMB will uncover many secrets the Universe is hiding.

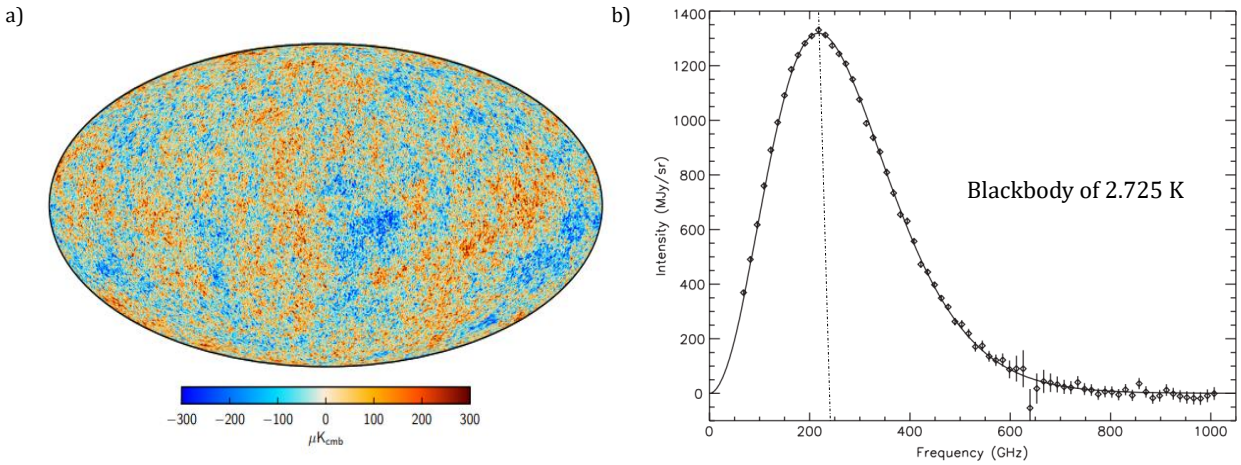

Figure 1.4: (a) Cosmic Microwave Background intensity mapped by *Planck* and WMAP [Aghanim et al., 2016]. (b) FIRAS determined the CMB temperature to be 2.725 ± 0.001 K as a perfect blackbody [Fixsen, 2009].

Line intensity mapping Line-intensity mapping (LIM) is an approach to survey the Universe, using relatively low-aperture instruments to scan large portions of the sky and detect the large scale collective line emission from galaxies using wide-field spectral mapping. It tracks the physics of the intra-cluster gas, the large-scale bulk flows, and star-forming regions in our Milky Way to study the dust properties and its link with star formation. Another interest in cosmology related to LIM is to trace the large structures at high redshift. The [CII] line at 158 μm is one of the main cooling lines of the interstellar medium [Bethermin et al., 2022]. Observational studies at low redshift found a non-evolving and nearly-linear empirical correlation

between [CII] luminosity and SFR. Semi-analytical models ([Lagache et al., 2018]) predict a weakly evolving relation with redshift. The [CII] line is thus a suitable tracer of the high-z star formation at large scales. Several intensity mapping experiments ([Kovetz et al., 2017]) aim to probe the [CII] emission from z>4 galaxies redshifted in the submillimeter domain: the Carbon [CII] line in post-reionization and reionization epoch project (CONCERTO, [Monfardini and Lagache, 2021]), the instrumentation for the tomographic ionized-carbon intensity mapping experiment (TIME, [Crites et al., 2014]), and the Fred Young submillimeter telescope (FYST, formerly CCAT-prime, [Stacey et al., 2018]).

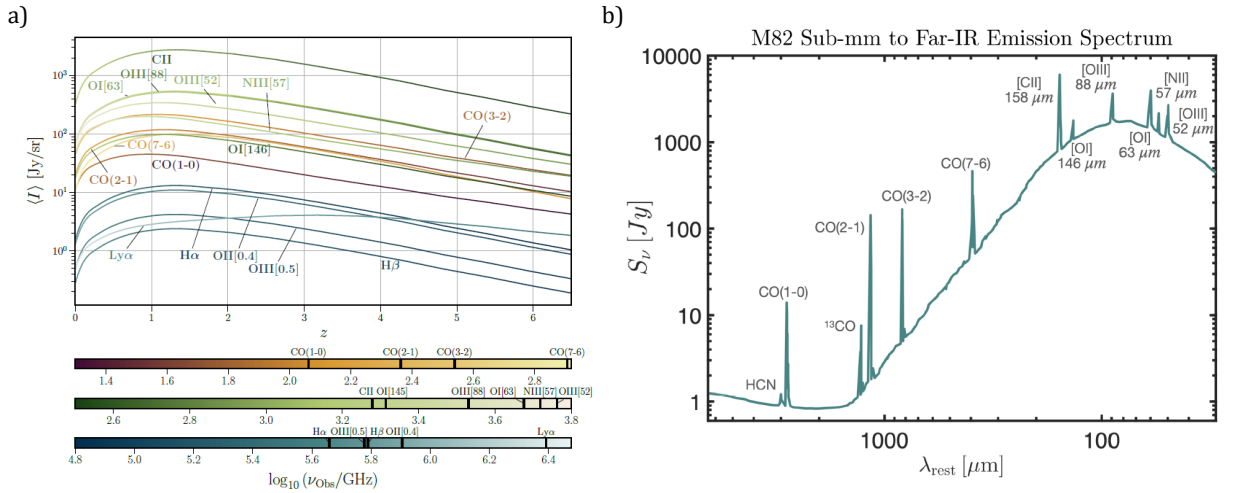

Figure 1.5: (a) Spectral lines mean intensity (as rest-frame frequencies marked with vertical bars in the colorbar) as function of redshift. The line-intensity ratios evolve with redshift. (b) Rest Frame emissions from the M82 galaxy which is starburst galaxy approximately 12 million light-years away.

Limitations of ground based mm wave astronomy Observations at mm and sub-mm wavelengths are limited by the atmospheric absorption and the available technologies. The presence of absorption bands of tropospheric water vapour is one of the major issues as shown in Fig. 1.6. In order to reduce this problem, the telescopes are usually placed at the highest altitudes and in the driest places (Atacama desert, Plateau de Bure in the French Alps, Pico Velveta in Spain, Chajnantor in Chile, Mauna Kea in Hawaii, Tenerife in Spain, Antarctica etc.). Transparent bands are called *"atmospheric windows"* and for example, they occur at 90 GHz ("3 mm", ALMA band 3), 150 GHz ("2 mm", ALMA band 4) and 250 GHz ("1 mm", ALMA band 5,6,7). Around these frequencies/wavelengths, it is possible to observe from the

ground.

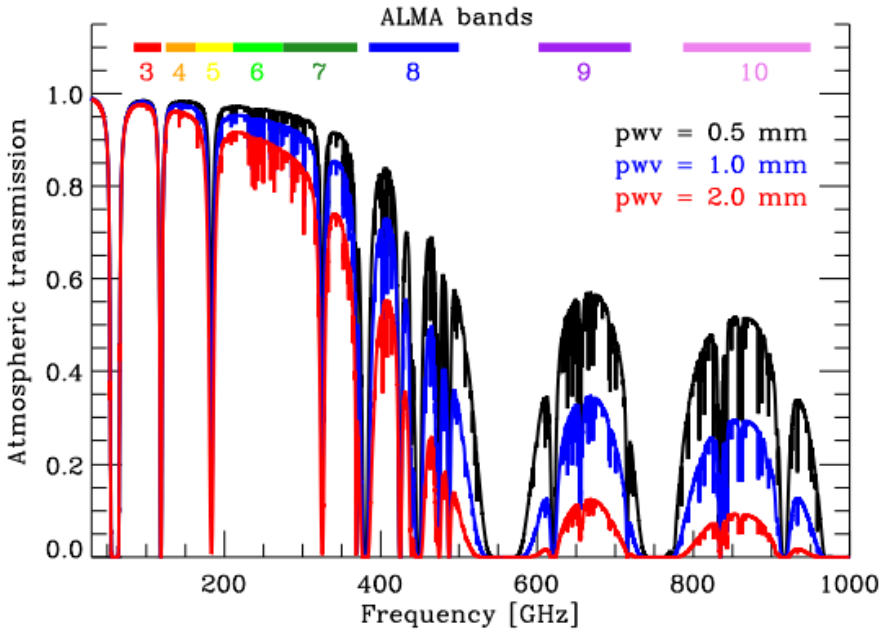

Figure 1.6: Atmospheric transmission at Chajnantor Plateau, the ALMA site, with different amounts of precipitable water vapor (pwv). The horizontal colored bars indicate the frequency ranges of the ALMA bands. Taken from [Maiolino, R. et al., 2008].

In this thesis, we have decided to focus on the 3 mm atmospheric window (75-110 GHz, ALMA band 3) for developing our prototype devices that will then be extended at 2 mm and 1 mm.

1.2 Detectors for mm wave detection

The detection of a signal happens when the incoming electromagnetic radiation is transduced into an electrical signal. There are two types of detectors used in mm and sub-mm wavelengths:

- Coherent detectors, such as heterodyne receivers, are designed to detect both the amplitude and phase of the field's complex amplitude.
- Incoherent detectors, on the other hand, respond to the power or intensity of the field, and they can be classified into two categories:
  - Thermal detectors, including Semiconducting bolometers and bolometers based on Transition Edge Sensors (TES).

- Superconducting Photodetectors, such as Kinetic inductance detectors (KIDs) and Superconducting tunnel junctions (STJs).

Instruments based on different detectors are used depending on the application and are associated with specific advantages and disadvantages. The basic principles of the detectors are discussed below.

Coherent Detector For long wavelengths from the radio into the far-infrared, coherent detection is widely popular. For example in heterodyne receivers, the incoming signal combines with the carrier frequency using local oscillators (LO), resulting in the creation of side-bands (IF). These IF signals are amplified and recorded. Coherent detectors allow very high spectral resolution observations. They are mostly used for line detection.
Coherent detectors are commonly used in receivers of instruments such as the Eight Mixer Receiver (EMIR) [Carter et al., 2012], which serves as a multi-band mm-wave receiver for the IRAM-30m telescope. Additionally, coherent detectors find usage in receivers for prominent telescopes such as the Atacama Large Millimeter/submillimeter Array (ALMA) [Hwang et al., 2016], the Northern Extended Millimeter Array (NOEMA) [Neri et al., 2020], and the Submillimeter Array (SMA) [Ho et al., 2004].

Thermal Detector Bolometers absorb the incoming photons in an absorber and convert the incoming energy into heat (phonons). This heat change is detected by a thermometer. The thermometer and the absorber are linked via a weak thermal link to a heat sink (cryostat). The advantages of these detectors, operated at very low temperatures ($<$1 K), are high sensitivity and a flat spectral response over a wide bandwidth. For this reason, they are used for continuum observations. Examples include Max-Planck-Millimetre-Bolometer (MAMBO) [Omont et al., 2003] for the IRAM-30 m telescope, Bolocam at the Caltech Submillimeter Observatory (CSO), Sub millimetre Common-User Bolometer Array 2 (SCUBA-2) for James Clerk Maxwell Telescope (JCMT) [Holland et al., 2013], MUSTANG-2 for the 100 m Green Bank Telescope (GBT) [Dicker et al., 2014], Large APEX Bolometer Camera (LABOCA) [Siringo et al., 2009], Submillimetre APEX Bolometer Camera (SABOCA) [Siringo et al., 2010] and Architectures de bolometres pour des Telescopes a grand champ de vue dans le domaine sub-Millimetrique au Sol (ArTeMiS) [Revéret et al., 2014] on 12 m APEX etc.

Photodetector Semiconductor materials have a band gap in the range of eV which has made it possible to detect UV-VIS-IR wavelength with devices like charged coupled devices (CCD). A superconductor has intrinsically a much lower band gap ($\sim$1 meV) and the detectors for mm wavelength are designed utilizing this property to detect mm-wave photons.
SJTs are very thin layers of insulators, sandwiched between two superconducting layers (SIS: superconductor-insulator-superconductor). When the detection of an incoming photon happens, a current pulse or an electrical charge proportional to the incoming photon energy sparks with a small magnetic field and bias-voltage well-below the transition temperature (T_c). These devices are popular for single photon detection.

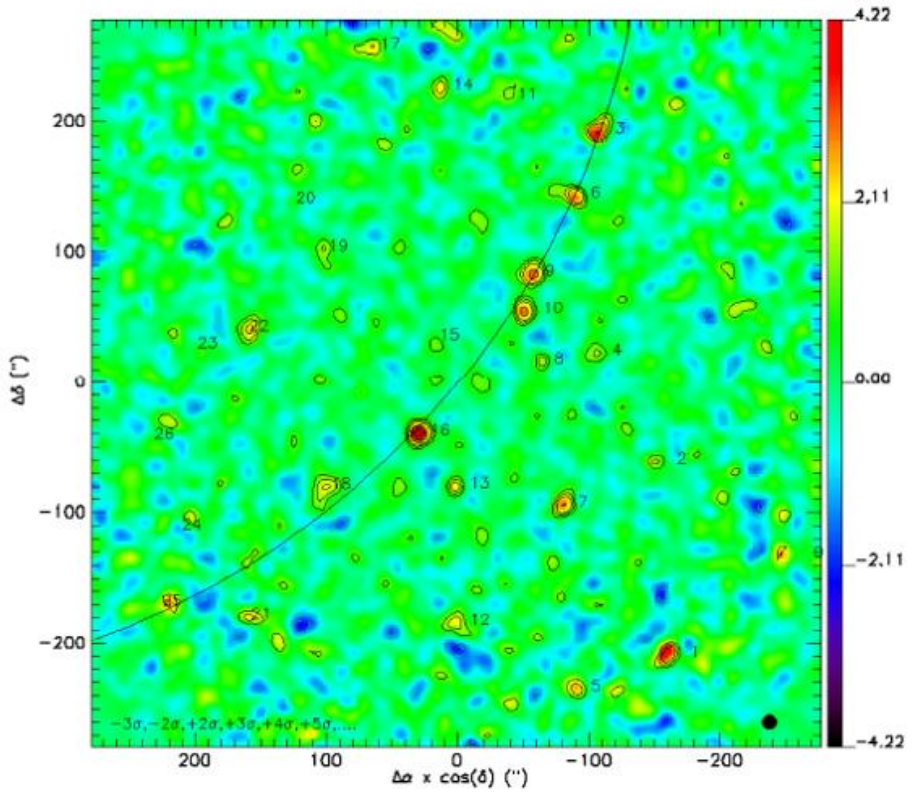

Figure 1.7: A NIKA2 map at 1.15 mm of spatially distributed submillimeter sources along a filament-like structure; taken from [Lestrade et al., 2022]. The color scale is in mJy/beam and contours represents the signal to noise ratio). Such candidate sources discovered by NIKA2 must be followed up individually by heterodyne instrument in order to determine the redshift(ongoing).

In order to improve the detection performance, it is necessary to increase the pixel count. Frequency multiplexing in KIDs is the most decisive advantage. The working principle of these devices will be discussed in Chapter 2.

1.3 Motivation for mm wave spectrometer

Currently, the photometric cameras installed on large single-dish telescopes are typically equipped with either photodetectors or thermal detectors. These cameras are used in various instruments, such as NIKA [Monfardini et al., 2011], NIKA2 [Adam, R. et al., 2018], GISMO [Magnelli et al., 2019], Bolocam [Ginsburg et al., 2013], AzTEC [Wilson et al., 2008], TolTEC [Bryan et al.,

2018], SCUBA2 [Holland et al., 2013], MUSTANG 2 [Dicker et al., 2014]. These instruments serve multiple purposes, including conducting large area blind continuum surveys in search of previously unknown and most likely high-redshift objects.
Although these cameras can have a relatively high angular resolution (e.g. 5-30 arcsec depending on the telescope size and wavelength) and can cover large portions of the sky (e.g. several deg^2) with high sensitivity (e.g. $RMS_{MAP}<$ 1 mJy), the achievable spectral resolution ($R = \frac{\lambda}{\Delta\lambda}$) is as low as $10^0 - 10^1$. This is considered as multicolour-imaging. It has been observed by these surveys in submillimeter and millimeter wavelengths that there are high-Z dust-obscured populations of galaxies forming stars at prodigious rates, sometimes exceeding 1000 $M_\odot$/yr, with correspondingly bright far infrared luminosities larger than 10^{12} $L_\odot$. Fig. 1.7 shows a number of galaxies in filament-like structures detected by NIKA2 camera.
With coherent detectors, it is possible to achieve very high spectral resolution ($R = 10^6 - 10^7$) to probe the redshift of single objects. However, it is impossible to cover a large field of view (FoV) with such instruments because of the small number of pixels. There are many candidate sources that are imaged by the large field of view mm wave cameras but it is impossible to follow them all up with high-resolution spectroscopy. As the emission spectral line width of these cosmological sources is around 0.5 GHz, it brings us to the importance of detectors with moderate spectral resolution ($R = 10^2 - 10^3$) but larger field of view than interferometers like ALMA or NOEMA.
In the framework of millimeter-wave astronomy, on-chip spectrometers aim to achieve intermediate spectral resolution, i.e. $R = \lambda/\Delta\lambda = 100 - 1000$, preserving the high sensitivity typical of continuum detectors and covering a larger instantaneous FoV. The key advantage compared to the existing Fourier transform spectrometers [Monfardini and Lagache, 2021] is the reduction of the optical background per channel, with a gain in the achievable photon-limited noise that can theoretically approach $1/\sqrt{R}$. On top of that, the optical design is enormously simplified. The main drawback, on the other hand, is the need for one readout channel per spectral band. On chip spectrometers based on Kinetic Inductance Detectors (KID) have already been proposed (Micro-Spec [Volpert et al., 2022], SPT-SLIM [Karkare et al., 2022], WSPEC [Bryan et al., 2015]) and fabricated and tested (SuperSpec [Karkare et al., 2020], DESHIMA [Endo et al., 2019]). The Micro-Spec spectrometer was designed for a resolution around 512 in the 420-540 GHz band. The SuperSpec device demonstrated a resolution of $\sim$ 275 in the 255-278 GHz band. The DESHIMA spectrometer on the ASTE 10-meters telescope achieved a bandwidth of 45 GHz centred around 350 GHz with a resolution of 380 with the field of view and angular resolution of 20 arcsec per single pixel. We propose and discuss two designs of on-chip spectrometers, On-chip spectrometer using Microstrip based Kinetic Inductance Detector (OMKID) and Hyperspectral Device with Kinetic Inductance Detector (HYPKID) in this thesis.

1.4 Outline of the thesis

In this introductory section, I have provided an overview of the scientific context and outlined the underlying motivation that drives the development of our device. This discussion sets the stage for the subsequent chapters, laying a foundation for the reader to understand the significance and purpose of this work.

Chapter 2 will present an overview of the fundamental principles and components used in our device, covering various topics such as complex conductivity, the characteristics of KIDs, and the behaviour of different superconducting materials. These elements serve as building blocks for the subsequent design of OMKID and HYPKID.
In Chapter 3, the idea of an on-chip spectrometer is described, the key elements present in our device are outlined, and a detailed conceptual description of our device is provided.
In Chapter 4, a detailed explanation of the step-by-step simulation process employed in my study will be provided, with a specific focus on the utilization of software tools like Sonnet and CST Studio. This chapter will offer insights into the simulation methodologies adopted for each component of the devices, aiding in the understanding of their behaviour and performance.
Chapter 5 will explore the fabrication process employed in our study, discussing the steps and procedures involved in the production and assembly of OMKID and HYPKID. The chapter will provide practical insights into the transformation of the devices from design concepts to physical realizations.
Comprehensive coverage of essential measurements conducted for both OMKID and HYPKID devices, along with an exploration of the employed data analysis procedures, will be the focus of Chapter 7 and 8 . This chapter will offer insights into the steps taken to improve the accuracy and reliability of the device measurements, enhancing the overall understanding of their capabilities.
Chapter 9 will integrate the significant findings and conclusions derived from the study, highlighting key results and their implications.
Lastly, chapter 10 will provide a discussion on future prospects and potential research directions, shedding light on the advancements that can be achieved and the broader impact of the developed device.

Chapter 2

Superconductivity

The focus of the thesis revolves around designing devices using planar superconducting components that operates at temperatures below 100 mK. This chapter will introduce and explain each of these basic terms which eventually help us to develop the subsequent chapters.

2.1 Fundamentals

2.1.1 Transition temperature, T_c and Superconducting Gap, Δ_0

In general, superconductivity arises in a metal with zero DC resistance below a certain temperature called the transition temperature, T_c [Onnes, 2012] with complete expulsion of the static magnetic field. This is a material-dependent property; e.g., bulk aluminum shows T_c around 1.2 K, and for bulk titanium, it is around 370 mK, whereas, in this temperature range, gold still behaves as a normal metal.
According to the free electron model, the electrons in a crystal lattice of metal follow Fermi-Dirac (FD) statistics as each electron occupies a single particle state. The single particle density with energy for electrons is shown in Fig. 2.1 for temperatures below and above T_c. At room temperature, the energy states are occupied according to Fermi-Dirac distribution around an energy state equivalent to the chemical potential of the metal, called Fermi energy, E_F. The properties of the metal in its normal state are related to thermal excitations. At temperatures above T_c, some states above E_F are occupied with thermal electrons, while some states below E_F are empty. Below T_c, the superconductivity arises as the available energy states are shifted above $E_F + \Delta(T)$ and below $E_F - \Delta(T)$ increasing the DOS at the edges of the energy gap, $E_F \pm \Delta_0$. The electrons condense into electron-electron pairs. The energy of each electron in the pair is lowered by the exchange of a virtual phonon, which generates an attractive force between the electrons. The strongest interaction takes place in between the pairs with opposite momenta and antiparallel spins, resulting in the formation of bound states called Cooper Pair [Cooper, 1956]. All the Cooper pairs condense according to Bose-Einstein statistics. At zero temperature, the energy state in between $E_F \pm \Delta_0$ is not occupied by any unpaired electrons.

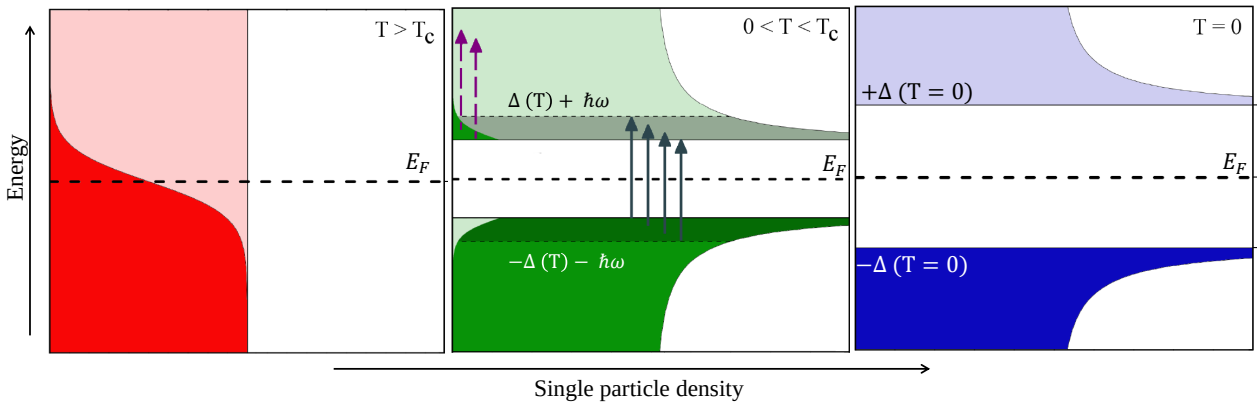

Figure 2.1: Single-particle density of states around the Fermi energy E_F of a superconductor. (left to right) For T > Tc, the energy states follow the Fermi-Dirac distribution, leading to both occupied and empty states relative to E_F. At $0 < T < T_c$, a temperature-dependent energy gap $2\Delta(T)$ emerges around E_F. At finite temperatures within this range, thermally activated unpaired electrons occupy states above the gap, contributing to σ_1 through photon absorption. At T = 0, no electrons are apparent and $2\Delta(T)$ reaches it's maximum. [Pracht et al., 2013]

According to the theory of superconductivity by J. Bardeen, L. N. Cooper, and J. R. Schrieffer [Bardeen et al., 1957], at finite temperatures ($0 < T < T_c$), Cooper pairs break into unpaired electrons. Depending on the occupation, they are identified as quasi-electrons or quasi-holes, whose properties can be described as fermions. The energy of the excitations above the collective ground state is given by,

$$E_k = \sqrt{\epsilon_k^2 + |\Delta_0|^2} \tag{2.1}$$

where ϵ_k measures the energy of the quasi-particle state at wave vector k relative to the Fermi energy E_F and $2\Delta_0$ is the magnitude of the energy gap in the single-particle density of states. This is the maximum energy gap at zero temperature, as given by,

$$2\Delta_0 = 3.528 k_B T_c \qquad k_B = \text{Boltzmann Constant} \tag{2.2}$$

The temperature dependency of the gap can be approximated by [Prozorov and Giannetta, 2006],

$$\Delta(T) \approx \Delta_0 \tanh\left(\frac{\pi T_c}{\Delta_0}\sqrt{a\left(\frac{T_c}{T} - 1\right)}\right) \tag{2.3}$$

where a is a parameter dependent upon the particular pairing state.

2.1.2 Gap Frequency

Below T_c, an incoming photon with $E = \hbar\omega$ (where $\omega = 2\pi\nu$) is absorbed by the Cooper Pair, and the quasi-particles are generated when the equivalent frequency of the energy is equal to

or higher than,

$$\nu_g = \frac{2\Delta}{h} = \frac{3.528 k_B T_c}{h} = 73.5 T_c \qquad [\text{GHz K}^{-1}] \tag{2.4}$$

For frequencies higher than ν_g, Cooper pairs are broken, and electrons are generated by absorbing photons. Such frequencies are in the range of far infrared, terahertz, and microwave frequencies, depending on T_c.

2.1.3 Quasiparticles-Generation and recombination

In the superconducting state, ($T \ll T_c$) when photons with energies higher than twice the gap energy are absorbed, the Cooper pairs break into two so-called "quasiparticles". They are unstable and eventually combine back into a Cooper pair through the emission of phonons. In thermal equilibrium, the constant generation and recombination result in a constant number of quasiparticles. The density of thermally excited quasi-particles (n_{qp}) at any temperature, T is proportional to the density of states times the Fermi distribution function $f(E)$:

$$n_{qp}(T) = 4N_0 \int_{\Delta}^{\infty} \frac{E}{\sqrt{E^2 - \Delta^2}} f(E)\, dE \tag{2.5}$$

where N_0 is the single-spin density of states at the Fermi surface ($1.72\times\ 10^{10}\ \mu\text{m}^{-3}\text{eV}^{-1}$ for Al) and

$$f(E) = \frac{1}{1 + e^{\frac{E}{k_B T}}} \tag{2.6}$$

The residual number of quasiparticles, N_{qp}, whose density in a superconductor of volume V is exponentially dependent on the temperature due to the presence of the energy gap. For $k_B T \ll \Delta$, the density is given by,

$$n_{qp} = \frac{N_{qp}}{V} \approx \left[2N_0 \sqrt{2\pi k_B T \Delta} \exp(-\Delta/(k_B T))\right] \tag{2.7}$$

The quasiparticle lifetime τ_{qp} is a measure of the average time a thermal quasiparticle remains above the gap energy before forming a Cooper pair. The theoretical quasiparticle lifetime for a thermal distribution and $T \ll T_c$ for a quasiparticle at the gap edge are given by Kaplan [Kaplan et al., 1976],

$$\frac{1}{\tau_{qp}} = \frac{\pi^{1/2}}{\tau_0} \left(\frac{2\Delta}{k_B T_c}\right)^{5/2} \left(\frac{T}{T_c}\right)^{1/2} e^{(-\Delta/k_B T)} \tag{2.8}$$

where τ_0 is a material dependent characteristic electron-phonon interaction time ($\tau_0 = 438$ ns for Al). For example, $\tau_{qp} \sim 4$ ms for 40 nm thick Al below 160 mK [De Visser et al., 2012]. During photon absorption, the number of quasi-particles rises until an equilibrium is reached between the number of quasi-particles being created to those recombining. It is possible to estimate the loaded equilibrium number of quasi-particles generated under a continuous flux of photons of energy $E > 2\Delta$,

$$n_{excess} = \frac{\eta P \tau_{qp}}{\Delta} \tag{2.9}$$

where n_{excess} is equal to the excess number of quasi-particles in the system, P is the optical power and η is the quasi-particle creation efficiency factor. Therefore, quasiparticle fluctuations are thus the fundamental source of potential signal in a pair-breaking detector, the incident power is detected through a change in the number of quasiparticles.

2.1.4 Proximity effect

The superconducting gap and its associated transition temperature serve as critical factors in material selection for our specific application. **Our device operates within a frequency range of 75 to 110 GHz. Below the superconducting transition temperature (T_c), a superconductor exhibits no losses below the gap frequency, while above the gap frequency, it behaves like a material with normal sheet resistance.** We use these characteristics to engineer thin films that manipulate the surface impedance of these films. Consequently, we require a superconducting material with a gap frequency exceeding 110 GHz and another material with a gap frequency falling below 75 GHz to achieve our desired functionality. Bulk aluminum is a superconductor characterized by a superconducting energy gap, $\Delta \approx 180$ μeV ($T_c \sim$1.2 K). The actual critical temperature T_c and the energy gap Δ depend on the thickness and quality of the films. The T_c of aluminum is also known to increase from 1.2 K for bulk up to typically about 1.4 K for 10-50 nm thin layers [Chubov et al., 1969][Steinberg et al., 2007]. For our specific application, we chose 20 nm thick aluminum a the gap frequency $\nu_g \approx 110$ GHz. To achieve a lower superconducting gap frequency, we choose a bilayer of aluminum and titanium using the proximity effect to tune the superconducting gap frequency. When two layers of superconductors, referred to as S_1 and S_2 ($T_{c_{S_1}} < T_{c_{S_2}}$), come into contact, their physical properties undergo changes. This proximity-coupling effect leads to changes in the density of states in both superconductors, resulting in a gap Δ_g that falls between the gap energies of the two superconductors (Δ_{S_1} and Δ_{S_2}) [Kuprianov and Lukichev, 1988]. When Δ_2 is in contact with Δ_1, the quasiparticles near thermal equilibrium from the high gap superconductor may diffuse into the lower gap superconductor. The change depends on the properties of the two superconducting layers in contact, as well as the geometries of each film and the behavior of the interface, specifically the interface transparency. We can adjust the transition temperature of the bilayer using the proximity effect of two superconductors and the gap frequency. The solutions of the proximity effect for multi superconducting layers are well-described in [Brammertz et al., 2001] when both of the superconductors are in the dirty limit condition, $l_{S_i} \leq \xi_{S_i}$ where l_{S_i} is the electronic mean free path and ξ_{S_i} is the coherence length.
Bulk titanium has a transition temperature (T_{cTi}) around 370 mK [Steele and Hein, 1953][Thiemann et al., 2018]. The superconducting transition temperature T_c is found to increase with decreasing thickness, e.g., T_c for a 100 nm Ti layer is around 580 mK [Xu et al., 2020][Zhao et al., 2018][Zhao et al., 2020]. The measurements of 100 nm thick Ti layer with different thickness of Al are obtained in [Zhao et al., 2018]. The model of bilayer has been also predicted. We use 10 nm thickness of titanium on 25 nm of aluminum which was previously used for LEKIDs and described in [Catalano et al., 2015]. Other groups have also reported the use of TiAl bilayers [Paiella et al., 2016] [Aja et al., 2020]. The transition temperature lies in the range of 900 mK to 1000 K for the bilayer. This provides a threshold frequency for photon absorption between 62 GHz and 70 GHz. The other reason for choosing Ti instead of noble metals comes from its weak solubility in Al, which improves predictability and reproducibility.

2.2 Penetration Depth

A superconductor in the Meissner state [Essén and Fiolhais, 2012] screens its interior from the magnetic field through a highly non-homogeneous supercurrent density, **J**. The penetration depth, or London's penetration depth at zero temperature, is given by

$$\lambda_L(0) = \sqrt{\frac{m}{n_s e^2 \mu_0}} \tag{2.10}$$

The coherence length ξ_0 was introduced by [Pippard and Bragg, 1953]. It is the minimum distance over which the superfluid density can vary. If impurities are present in the superconductor, the actual coherence length (ξ_0) varies depending on the mean free path (l) and the effective coherence length, ξ_{eff} becomes,

$$\frac{1}{\xi_{eff}} = \frac{1}{\xi_0} + \frac{1}{l} \tag{2.11}$$

The superconductor is dirty if $l/\xi_0 \ll 1$ and $\xi_{eff} \approx l$ and is clean when $l/\xi_0 \gg 1$ and $\xi_{eff} \approx \xi_0$. We use thin films, of thickness, $d \approx$ nm for which the mean free path is perturbed at the surface. Thus, superconducting films for our detectors are working in the dirty limit.

For extreme dirty superconductors($l \ll \xi_0$), the London penetration depth becomes, $\lambda_{eff}(l,T) = \lambda_L(T) \times (\xi_0/l)^{1/2} J(0,T)^{-1/2}$ where $J(0,T)$ varies from 1 at T=0 to 1.33 for $T = T_c$.
According to the microscopic theory by BCS, at temperatures very near T_c, the excitations of quasi-particles by the electromagnetic field have a significant effect on the penetration depth. The presence of excitations modifies the penetration depth by the formula,

$$\frac{1}{\lambda^2(T)} = \frac{1}{\lambda^2(0)} \left(1 - 2\int_{\Delta}^{\infty} \frac{\partial f(\epsilon)}{\partial \epsilon} \frac{\epsilon}{\sqrt{\epsilon^2 - \Delta^2}}\, d\epsilon\right) \tag{2.12}$$

where $\frac{\epsilon}{\sqrt{\epsilon^2-\Delta^2}}$ is the BCS density of states and $f(\epsilon)$ is the the occupation probability of a state of energy ϵ.

2.3 Complex conductivity

The Drude model gives the frequency-dependent electrical conductivity of the free electrons in a time-dependent electric field, $\mathbf{E(t)} = \mathbf{E}e^{-i\omega t}$ is given by [Ashcroft and Mermin, 1976],

$$\sigma(\omega) = \frac{\sigma_n}{1 + i\omega\tau} = \frac{n_0 e^2 \tau}{m^*} \frac{1}{1 + \omega^2\tau^2} - i\omega \frac{n_0 e^2 \tau^2}{m^*} \frac{1}{1 + \omega^2\tau^2} \tag{2.13}$$

where $\sigma_n = \frac{n_0 e^2 \tau}{m^*}$ is the dc conductivity at zero frequency and τ is the scattering time, which is assumed to result solely from collisions between electrons, phonons or impurities. The average distance travelled by electrons between collisions is the mean free path, and given by, $l = v_F.\tau$, where v_F is the velocity evaluated at the Fermi level, n_0 is the number of electrons in the cubic centimetre and m^* is the effective mass of an electron.
The two-fluid model by Bardeen [Bardeen, 1958] is used to simply describe the electrodynamics

of the superconductors in the context of the motion of elementary excitations, "normal" electron density (n_n) and "superconducting" electron density (n_s) in the alternating electromagnetic field. While carrying time dependent alternating current, the total current, **J** conducts through the quasi-particles or via Cooper pairs (J_s) is

$$\mathbf{J}(\omega, T) = \sigma_\omega \mathbf{E}(\omega, T) \tag{2.14}$$

Below T_c, the scattering time for Cooper pairs is infinite, $\tau_s \to \infty$. Therefore, the complex conductivity for the superconductors can be approximated for frequencies below the gap frequency ($\omega\tau \ll 0$) from Equation 2.3 as [Tinkham, 2004],

$$\sigma(\omega) = \sigma_1(\omega) - i\sigma_2(\omega) = \frac{n_{qp}e^2\tau_n}{m^*} - i\frac{n_s e^2}{\omega m^*} \tag{2.15}$$

The real part of the conductivity, σ_1, accounts for the response of the quasiparticles; whereas the imaginary part, $-\sigma_2$, accounts for the non-dissipative response from the Cooper pairs. Even though normal electron density reduces exponentially to zero as $n_{qp} \sim \mathrm{e}^{-\Delta/k_B T}$ at low temperatures, there is a finite number of quasiparticles from the n_n at non-zero frequency, which causes dissipation.
A microscopic treatment of the complex conductivity was derived by Mattis and Bardeen, which consistently takes into account both the Cooper pair condensate and the quasiparticle excitations [Mattis and Bardeen, 1958]. Expressions for σ_1 and σ_2 with respect to the normal state conductivity ($\sigma_n = \sigma_{qp}$) are given by,

$$\frac{\sigma_1}{\sigma_n} = \frac{2}{\hbar\omega}\int_{\Delta_0}^{\infty} \left[f(E) - f(E+\hbar\omega)\right] g(E) dE + \frac{1}{\hbar\omega}\int_{\Delta_0-\hbar\omega}^{-\Delta_0} \left[1 - 2f(E+\hbar\omega)\right] g(E) dE \tag{2.16}$$

$$\frac{\sigma_2}{\sigma_n} = \frac{1}{\hbar\omega}\int_{\Delta_0-\hbar\omega,-\Delta_0}^{\Delta_0} \frac{\left[1 - 2f(E+\hbar\omega)\right](E^2 + \Delta_0^2 + \hbar\omega E)}{(\Delta_0^2 - E^2)^{1/2}\left[(E+\hbar\omega)^2 - \Delta_0^2\right]^{1/2}} \tag{2.17}$$

where

$$g(E) = \frac{(E^2 + \Delta_0^2 + \hbar\omega E)}{E_1 E_2} \tag{2.18}$$

where $E_1 = (E^2 - \Delta_0^2)^{1/2}$ and $E_2 = \left[(E + \hbar\omega E)^2 - \Delta^2\right]^{1/2}$ are energies corresponding to E and $E + \hbar\omega$. The second term of Equation 2.16 is important when $\hbar\omega > 2\Delta_0$ and in this regime, usually $\sigma_2 \gg \sigma_1$. As at $T = 0$, no quasi particles are excited, $\sigma_1(T = 0) = 0$ and σ_2 equals to [Flanigan, 2018],

$$\frac{\sigma_2(\omega, 0)}{\sigma_n} = \frac{\pi\Delta_0}{\hbar\omega} \tag{2.19}$$

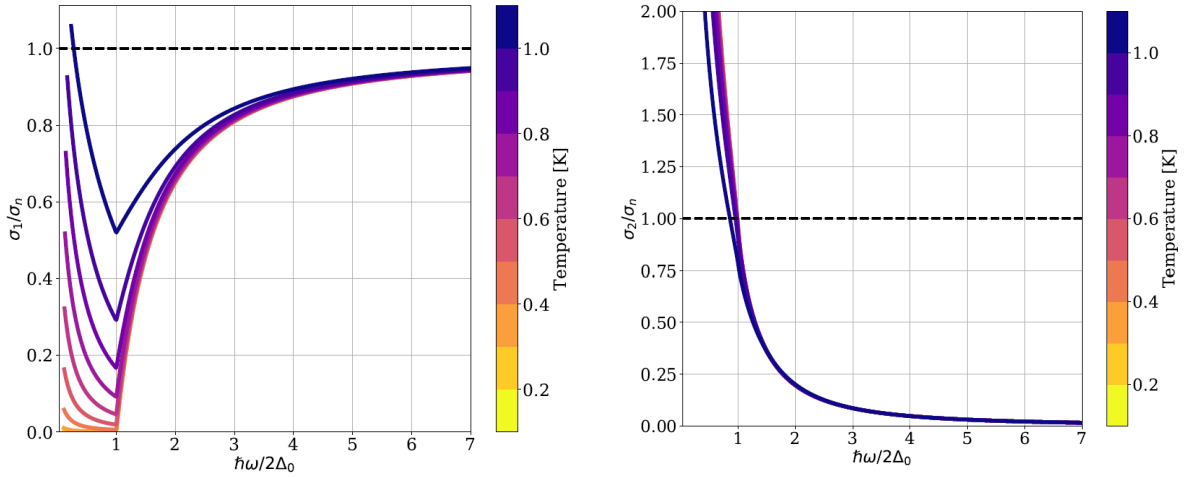

Figure 2.2: The variation of complex conductivity as a function of frequency (ω) and temperature (T) in terms of (a) real component, σ_1 and (b) complex component, σ_2 using Equation 2.16 and Equation 2.17. Taken from the thesis of Amber Hornsby [Hornsby, 2020].

Transmission with frequencies From the expressions of σ_1 and σ_2, the fractional transmissivity of a thin superconducting film (thickness, $d < \lambda_{eff}$) can be shown as [Tinkham, 1956] [Glover III and Tinkham, 1956],

$$T_m = \left[\left(1 + \frac{\sigma_{1m} dZ_0}{n_r + 1}\right)^2 + \left(\frac{\sigma_{2m} dZ_0}{n_r + 1}\right)^2\right] \tag{2.20}$$

where n_r is the refractive index of the substrate, Z_0 is the impedance of the free space and d is the film thickness. T_s as the transmission in the superconducting state and T_n as the transmission in the normal state, where $m = n$ or s.
When $\omega \to 0$, $\sigma_2 = 1/\omega \to \infty$, the transmissivity, $T_s \to 0$ which gives rise to **the total reflection of the incoming signal**. Whereas, when $\hbar\omega \gg 2\Delta_0$, $\sigma_{2_s} \to 0$ and $\sigma_{1s} \to \sigma_n$, which makes $T_s \approx T_n$. And $\hbar\omega \approx 2\Delta_0$, both σ_{1s} and σ_{2s} are smaller than σ_n, which gives $T_s > T_n$.

Surface Impedance For a circuit analogy for a thin film, σ_1 is the conductance or $1/R_s$ of a resistive channel in parallel with σ_2, the inductive channel impedance, $1/j\omega L_s$. Most of the current flows in the lossless inductive channel below the characteristic frequency $\omega_0 = R_s/L_s$ and above through the resistive channel. The frequency dependence of σ_2 is often interpreted

in terms of frequency dependent kinetic inductance. Therefore the surface impedance is

$$Z_s = R_s + j\omega L_s \tag{2.21}$$

where $R_s = \frac{\sigma_1}{\sigma_2^2 d}$ is the surface resistance and $L_s = \frac{1}{\sigma_2 \omega d}$ is the surface inductance. For very thin films, the surface impedance has a direct relationship with the surface resistance as from Equation 2.3,

$$L_s = \frac{\hbar R_s}{\pi \Delta_0} \tag{2.22}$$

In terms of effective penetration depth, we can also express,

$$Z_s = j\mu_0 \omega \lambda_{eff} \tag{2.23}$$

where $\lambda_{eff} = \sqrt{\hbar/\pi\Delta\mu_0\sigma_n}$ and an effective penetration depth for thin films, $\lambda_{thin} = \lambda_{eff}^2/d$. Consider a plane superconductor with thickness, d. The magnetic field can penetrate through the film and both magnetic field and current density can be non-zero inside the film. If the film thickness d is smaller than the electron mean free path in the bulk case l_∞, l will be limited by surface scattering and $l \approx d$. Z_s can be derived as,

$$Z_s = \frac{1}{(\sigma_1 - i\sigma_2)d} \tag{2.24}$$

Z_s has a $\frac{1}{d}$ dependence on the film thickness d. For temperatures T much lower than T_c, $R_s \ll \omega L_s$. The surface impedance of conductive films with arbitrary thickness d in the dirty limit is given by [Kautz, 1978],

$$Z_s = \sqrt{\frac{i\omega\mu_0}{\sigma}} \coth(\sqrt{i\omega\mu\sigma}d) = \sqrt{\frac{i\omega\mu}{\sigma}} \coth\left(\sqrt{1 + i\frac{\sigma_1}{\sigma_2}}\frac{d}{\lambda}\right) = R_s + iX_s \tag{2.25}$$

where $\lambda = (\omega\mu\sigma_2)^{-1/2}$ is the magnetic penetration depth.
The surface impedance of a superconducting film changes when photons break Cooper pairs and generate quasiparticles generates. For thin film,

$$\frac{\delta Z_s(\omega, T)}{Z_s(\omega, 0)} \approx -\frac{\delta\sigma(\omega, T)}{\sigma(\omega, 0)} \tag{2.26}$$

2.4 Kinetic Inductance

When an electric current (I) is carried by charged particles of mass m and number density n, there is inductance (L) associated with the magnetic field perpendicular to the flow of the current which opposes the current. The magnetic energy stored in the field is given by $W_m = \frac{1}{2}LI^2$. The inductance L predominantly hinges upon the geometrical attributes of the system. Consequently, it is termed the geometric inductance and designated as L_m.
There is another term in the energy W_k due to the inertial mass of the particles that carry the electrical charge. In normal metals, this term can be neglected because it is proportional to the

average scattering time of electrons, which even for good conductors is very short. Due to frequent scattering, electrons have no time to accumulate a great amount of kinetic energy besides their thermal energy. Yet, in superconductors, it can have an important contribution because instead of electrons, the current is carried by Cooper pairs. This inertial mass is equivalent to an inductance, known as the kinetic inductance (L_k). According to the measurements of the kinetic inductance in a thin cylindrical film described in [Meservey and Tedrow, 1969], the kinetic inductance dominates the internal magnetic inductance when the one lateral dimension is less than λ_L. The energy associated with the kinetic inductance is given by,

$$W_k = \frac{1}{2}\frac{m}{ne^2}\frac{l}{a}I^2 \tag{2.27}$$

where $\frac{m}{ne^2}$ is the material dependent term and $\frac{l}{a}$ is geometric effect given by the length (l) divided by the cross-sectional area(a). Thus, the kinetic inductance is expressed,

$$L_k = \frac{m}{ne^2}\frac{l}{a} \tag{2.28}$$

For a long superconducting line of very thin cross section and small carrier concentration, the kinetic inductance is comparable to the geometrical inductance as discussed in Little [1967]. In terms of superconducting penetration depth (λ_L),

$$L_k = \mu_0 \lambda_L^2 l/a \tag{2.29}$$

The total inductance can now be written as

$$L_s = L_m + L_k \tag{2.30}$$

The surface inductance of a superconducting thin film with $d \ll \lambda_{eff}$ is given by, $L_s = \frac{1}{\omega\sigma_2 d}$. The equivalent kinetic inductance L_k and the effective kinetic inductance fraction α for the thin film case are still given by,

$$\alpha = \frac{L_k}{L_m + L_k} \tag{2.31}$$

$$\lambda(T) = \lambda_L(T)\sqrt{\frac{\xi_0}{t}} \tag{2.32}$$

For $d \ll \lambda_L(0)$, the penetration depth is dependent on thickness as $\lambda(T) = \lambda_L(T)/d$. At temperature, $T \ll T_c$, all the free electrons form the dissipationless Cooper pairs that exhibit $Z(\omega) = i\omega L_k$.

2.5 Resonators

We use superconducting resonating circuits, which are basically planar transmission lines with various lengths, shapes, and terminations. The equivalent circuits of the resonators are usually described using RLC resonating circuits containing resistance (R), inductance (L) and capacitance (C). In this section, we start with a short description of the basic circuit theory for a parallel RLC resonator circuit. The approach to describing a series circuit is similar and the

basics of complete circuit theory are well-described in the chapter called 'Microwave Resonators' in [Pozar, 2005]. We proceed by giving an example of a $\lambda/2$ resonator, which is eventually used for our work.

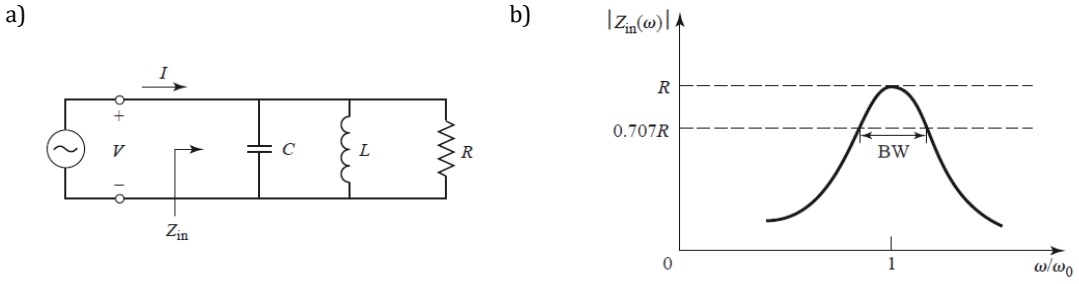

Figure 2.3: Parallel RLC resonator (a) The resonating circuit. (b) Input impedance magnitude vs relative frequency (ω/ω_0) with the half power fractional bandwidth (BW). Taken from [Pozar, 2005].

Resonating circuit At frequencies near resonance, a microwave resonator can usually be modelled by either a series or parallel RLC lumped-element equivalent circuit. The input impedance of a series unloaded resonant circuit shown in Fig. 2.3 is:

$$Z_{in} = \left(\frac{1}{R} + \frac{1}{j\omega L} + j\omega C\right) \tag{2.33}$$

At resonance, the average magnetic energy is equal to the average electric energy.

$$W_m = W_e \implies \frac{1}{4}|V|^2\frac{1}{\omega_0^2 L} = \frac{1}{4}|V|^2 C \implies \omega_0 = \frac{1}{\sqrt{LC}} \tag{2.34}$$

The quality factor of any circuit shows the characteristics of the resonance. It is defined as,

$$Q = \frac{\text{Energy stored in the circuit near resonance}}{\text{Average energy dissipated per cycle}} \tag{2.35}$$

If the circuit is lossy, it can be found in the Q values. Resonator losses may be due to conductor loss, dielectric loss, or radiation loss, and are represented by the resistance, R, of the equivalent circuit.An external connecting network may introduce additional loss. For the series resonant circuit, unloaded quality factor, $Q_0 = 1/\omega_0 RC$. For the resonator near its resonant frequency, $\omega = \omega_0 + \Delta\omega$, the input impedance can be simplified as,

$$Z_{in} \simeq \frac{R}{1 + 2j\Delta\omega RC} \approx \frac{R}{1 + 2jQ_0\Delta\omega/\omega_0} \tag{2.36}$$

In the Fig.2.3(b), the variation of the magnitude of the input impedance versus frequency is shown. At resonance, maximum power is delivered to the circuit. When the impedance

is $|Z_{in}|^2 = \frac{R^2}{2}$, the average (real) power delivered to the circuit is one-half that delivered at resonance. The half-power fractional bandwidth (BW) = $\frac{2\Delta\omega}{\omega_0}$ is is given by,

$$BW = \frac{1}{Q_0} \tag{2.37}$$

The quality factor due to loaded circuit because of coupling is given by,

$$\frac{1}{Q_l} = \frac{1}{Q_c} + \frac{1}{Q_d} + \frac{1}{Q_{rad}} \tag{2.38}$$

where the energy that dissipates from the resonator at the coupling capacitor, dielectric or radiation are given by Q_c, Q_d, and Q_{rad}. For a superconducting resonator on a monocrystalline dielectric (lossless), the measured Q of the resonator will be close to Q_c as the contribution of Q_d or Q_{rad} is comparably negligible.

Half-wavelength ($\lambda/2$) resonator The half-wavelength resonator is a planar thin line of length l whose working principle can be expressed by transmission line theory. The equivalent circuit can be described as a parallel resonant circuit. The fundamental resonance in this line usually occurs when the wavelength of the signal is $l = n\lambda_0/2$ where $\lambda_0 = \frac{c}{\omega_0}$. The resonance frequencies for all the modes are given by,

$$\omega_{0n} = \frac{nc}{2l\sqrt{\epsilon_{eff}}} \tag{2.39}$$

where n is the resonance mode, c is the velocity of light in vacuum and ϵ_{eff} is the effective dielectric constant, which is discussed in the Appendix. A.1.

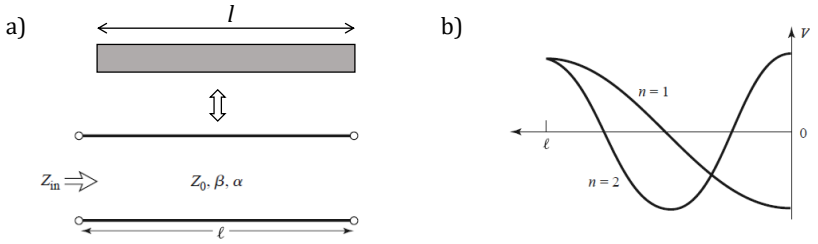

Figure 2.4: $\lambda/2$ resonator (a) A line of length l and its equivalent transmission line with the input impedance Z_{in} which is dependent on the characteristic impedance, Z_0, the propagation constant of the medium, β, and the attenuation constant, α. (b) The voltage variation over the length of the line. Taken from [Pozar, 2005].

A transmission line has a characteristic impedance, Z_0, defined by the ratio of voltage to current for a travelling wave, the propagation constant, β and the attenuation constant, α. The input

impedance of an open-circuited lossy transmission line of length l is given by the transmission $(ABCD)$ parameters of a two-port circuit as,

$$Z_{in} = Z_0 \coth(\alpha + j\beta)l = Z_0 \frac{1 + j\tan\beta l \tanh\alpha l}{\tanh\alpha l + j\tan\beta l} \tag{2.40}$$

For a lossless line(α =0) as we are using superconducting line,

$$Z_{in} = \frac{Z_0}{\tan\beta l} \tag{2.41}$$

Assuming that $l = \lambda/2$ at resoance frequecny, $\omega = \omega_0$ then,

$$\beta l = \pi + \frac{\pi\Delta\omega}{\omega_0} \tag{2.42}$$

which gives,

$$\tan\beta l = \tan\frac{\Delta\omega\pi}{\omega} \approx \frac{\Delta\omega\pi}{\omega_0} \qquad \tanh\alpha l \simeq \alpha l \tag{2.43}$$

Comparing to the input impedance of a parallel resonant circuit, the resistance, capacitance, and inductance of equivalent RLC circuit are,

$$R = \frac{Z_0}{\alpha l} \qquad C = \frac{\pi}{2\omega_0 Z_0} \qquad L = \frac{1}{\omega_0^2 C} \tag{2.44}$$

This gives the unloaded Q as,

$$Q_0 = \omega_0 RC = \frac{\pi}{2\alpha l} = \frac{\beta}{2\alpha} \qquad l = \frac{\pi}{\beta} \text{ at resonance} \tag{2.45}$$

which shows the quality factor decreases as the attenuation of the line increases.

2.6 Lumped Element Kinetic Inductance detectors

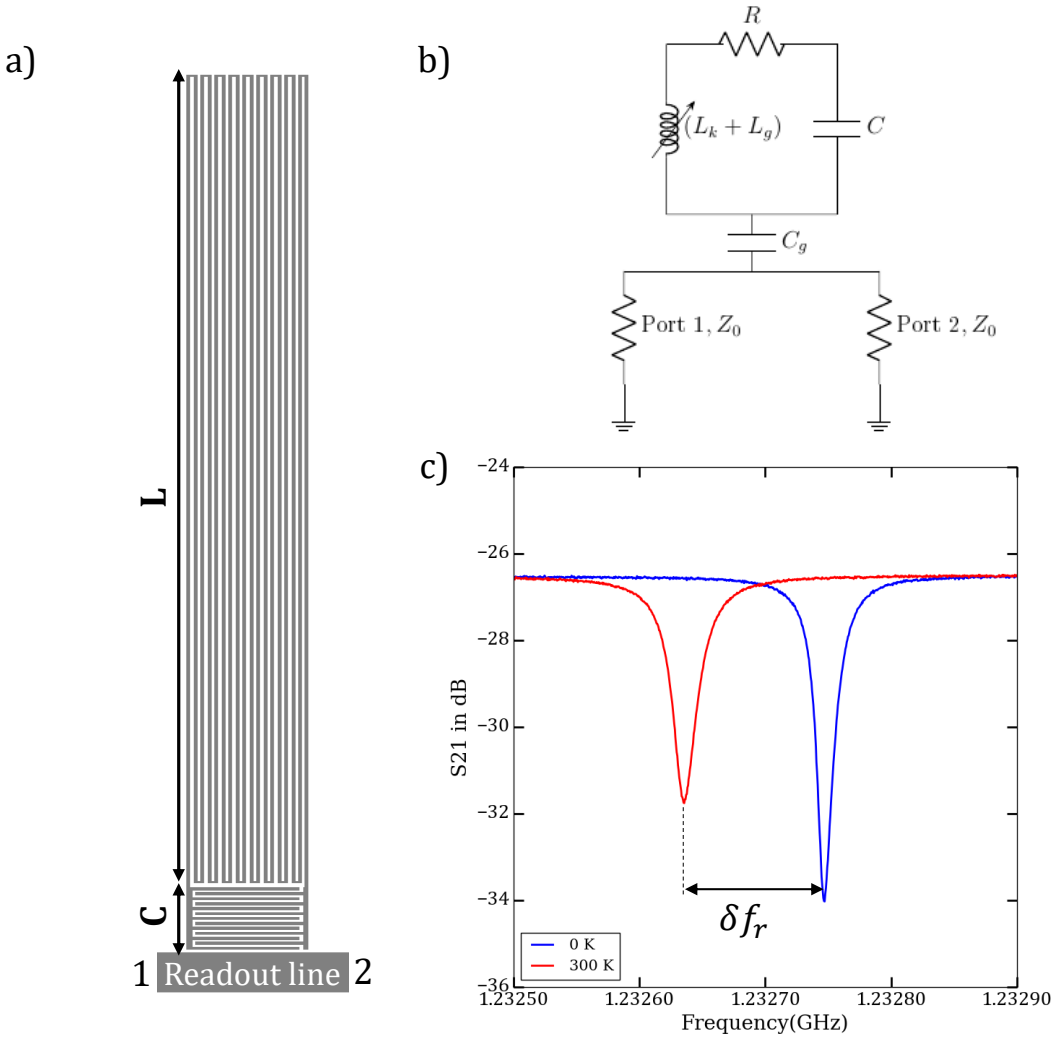

Figure 2.5: LEKIDs: (a) The design of a LEKIDs with the meander lines (L) and the interdigitated capacitance (C) coupled with the readout line in between two ports 1 and 2. (b) The equivalent circuit. (c) An electrical response of the resonance frequency with illumination (300 K) and without illumination (0 K).

The kinetic inductance detectors (KIDs) are resonating circuit designed with thin superconducting films. The resonating frequency of KIDs usually lies below the superconducting gap frequency, while the detection frequency is above the gap frequency. When illuminated radiation above the gap frequency, the photon interaction breaks the Cooper Pairs and increases the number density of the quasiparticles which affects the resonating frequency of the resonator.

The technology was introduced in [Mazin, 2005][Day et al., 2003]. The review of the KIDs are described in [Zmuidzinas, 2012][Mauskopf, 2018]. Depending on the layouts, there are two kind of KIDs, distributed elements KIDs or MKIDs (such as transmission line resonators), and lumped element KIDs or LEKIDs. Throughout the thesis, we will discuss LEKIDs. The concept of LEKIDs was discussed in [Doyle et al., 2008].
Let us consider a lumped element resonator of an ideal lossless superconducting circuit consisting of an inductance L and a capacitance C. The resonance occurs when the energy stored in the capacitor (C) (electrical energy) is equal to the energy stored in the inductor (L) (magnetic energy). As a result, the input impedance of the circuit can be described by as follows:

$$Z_{in} = i\omega L + \frac{1}{i\omega C} \tag{2.46}$$

The resonance occurs when the input impedance is zero. Thus, the resonating frequency of the circuit is given by:

$$f_{res} = \frac{1}{2\pi\sqrt{LC}} \tag{2.47}$$

In practice, the circuit contains several dissipative components, even in the lossless superconducting phase. These components introduce an effective resistive component, denoted as R, in series between L and C. The presence of R modifies the input impedance in the following manner:

$$Z_{in} = i\omega L + \frac{1}{R} + \frac{1}{i\omega C} \tag{2.48}$$

In a RLC circuit as shown in previous section, the Q is given as,

$$Q = \frac{1}{R}\sqrt{\frac{L}{C}} \tag{2.49}$$

Thus, the dissipation through R can be identified. The Q value is usually high as 10^5 with infinitesimal resistive losses as in a superconducting circuit.
The LEKID for our device is shown in Fig.2.5(a). The inductor part is usually a series of meandered lines and the capacitive part is interdigitated capacitors (IDC). The equivalent circuit of the resonator is shown in Fig. 2.5(b). As a basic resonator circuit, the LEKID can be expressed as the inductive component, $(L_k + L_g)$ and the capacitive component, C. The impedance of the resonator is given by,

$$Z_{res} = R + j\omega(L_k + L_g) + \frac{1}{\omega(C + C_g)}(\frac{1}{j} + \tan\delta_{eff}) \tag{2.50}$$

where $\tan\delta_{eff}$ is effective loss tangent of the dielectric material. The resonator is coupled to the microstrip readout line through the coupling distance, given by the capacitance C_g. A microwave probe tone tuned to the KIDs resonance frequency is sent down the readout line. The resonance frequency becomes,

$$\omega_0 = 2\pi f_0 = \frac{1}{2\pi\sqrt{(L_k + L_g)C}} \tag{2.51}$$

and the internal quality factor

$$Q_i = \frac{\omega_0(L_k + L_g)}{R} \tag{2.52}$$

In the presence of photons with energy, $h\omega > 2\Delta$, here, a variation in the optical loading ("0 K" to "300 K"), the density of Cooper pairs (n_s) and the quasiparticles (n_{qp}) changes. It results in a change in the resistive and inductive parts of the surface impedance of the films. As the density of the quasiparticles increases, the circuit becomes lossy which can be shown in the broader bandwidth of the resonance frequency. Whereas there is an increase in kinetic inductance (L_k) (geometrical inductance (L_g) is fixed by the circuit geometry) to ensure the circuit carries the same current with the reduced number of Cooper pairs. As the inductance increases, the resonance frequency lowers inversely. We observe the variation of a shift in the resonance frequency, δf_r as shown in Fig. 2.5(c).
A variation in the kinetic inductance and complex conductivity leads to changes in the resonance frequency,

$$\frac{\delta f_r}{f_r} = -\frac{\alpha}{2}\frac{\delta L_k}{L_k} \tag{2.53}$$

where α is the kinetic inductance fraction. The temperature dependence of Z_s results in the variation of the resonance frequency f_r and of the quality factor Q_r. The relationships between f_r, Q_r and X_s, R_s are

$$\frac{\delta f_r}{f_r} = \frac{f_r(T) - f_r(0)}{f_r(0)} = -\frac{\alpha}{2}\frac{X_s(T) - X_s(0)}{X_s(0)} = -\frac{\alpha}{2}\frac{\delta\lambda_{eff}}{\lambda_{eff}} \tag{2.54}$$

The LEKID resonator is coupled to the readout line through the coupling distance. The total quality factor Q_r can be divided into two components, the internal quality factor, Q_i and the coupling quality factor, Q_c.

$$\frac{1}{Q_r} = \frac{1}{Q_c} + \frac{1}{Q_i} \tag{2.55}$$

Q_c accounts for the energy exchange between the resonator and the readout line and it is mainly designed by specifying the relative distance between the resonator and transmission feedline. The internal quality factor is determined by the residual losses within the resonator itself. In our case, these losses are mainly due to the residual resistivity or radiation losses. A good thumb rule to achieve an appropriate correspondence between the responsivity of the device and its dynamic range is to have similar values of Q_i and Q_c. The ratio Q_i/Q_c defines three coupling regimes,

$$\frac{Q_i}{Q_c} = \begin{cases} > 1 & \text{overcoupled regime} \\ = 1 & \text{ideal for our case} \\ < 1 & \text{undercoupled regime .} \end{cases}$$

The typical transmission signal for a resonator is given by, [Flanigan, 2018] as,

$$S_{21} = 1 - \frac{Q_r(1 + iA)/Q_c}{1 + 2iQ_r x} \tag{2.56}$$

where the fractional frequency shift, $x = \delta f_r / f_r - 1$ where f_r is the resonant frequency and the asymmetry parameter A is necessary to characterize a commonly-occurring resonance asymmetry that can be caused either by parasitic coupling between the resonator and the feedline or by an impedance mismatch between the feedline and the transmission lines to which it connects. $A = 0$ for a symmetric response.

Noise The fundamental noise in KIDs is limited by the fluctuations in the quasiparticle density and noise that is inherent to the readout system. The generation-recombination noise (g-r noise) is proportional to the quasiparticle density itself, which decreases as $e^{(-\Delta/kT)}$ when T goes to zero. Therefore, by operating at $T \ll T_c$, in theory KIDs can achieve a very high detector sensitivity as 10^{-20} W/Hz$^{-1/2}$.

Frequency Domain Multiplexing The most attractive aspect of KIDs is its capability for large scale frequency domain multiplexing. **Each resonator is designed to have a slightly different resonant frequency, and is excited and read out independently. All the resonators are coupled to a single transmission line. The detectors are read out by sending a probe microwave signal containing a comb of frequencies tuned to the unique resonance frequency of each resonator. The frequency separation of resonators must be greater than the width of the typical resonance. The separation must be several times greater than f_r/Q.**

Chapter 3

Concept of OMKID and HYPKID

In this chapter, we will briefly discuss the fundamental concepts and working principles of available on-chip spectrometers, examining their available options and capabilities. Within this context, we will investigate and analyze the operational principles that underlie our device.

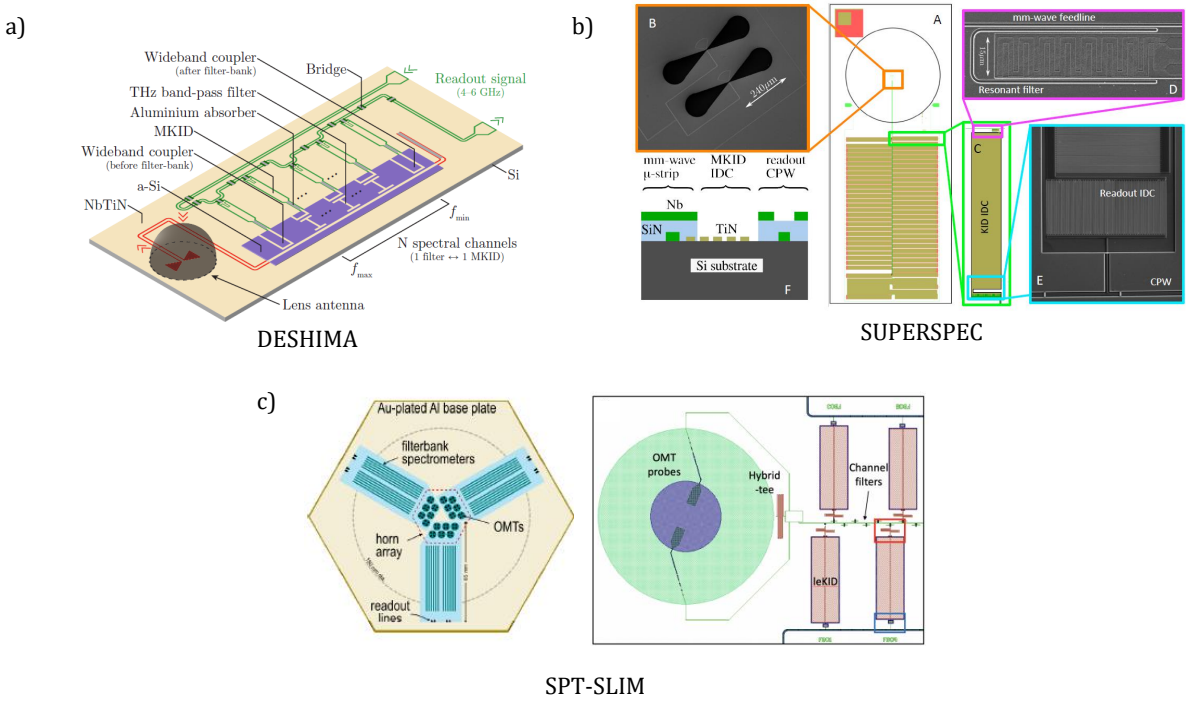

Figure 3.1: Available On-chip Spectrometers.

3.1 On chip spectrometers based on KIDs

Over the past decade, various groups, including Superspec [Karkare et al., 2020], Deshima [Endo et al., 2019], SPT-Slim [Karkare et al., 2022], μ-Spec [Volpert et al., 2022] specializing in millimeter wave technology, have been working on the development of on-chip spectrometers utilizing the kinetic inductance detectors. The fundamental idea of an on-chip spectrometer involves gradually filtering the incoming signal on the chip until a narrow band is attained. The selected band signal is then detected by the kinetic inductance detectors, which are detection units known for their sensitivity and frequency multiplexing capability. The on-chip design relies

on the superconducting properties of thin films. A short description of the on-chip spectrometers is given below.

DESHIMA DESHIMA is a superconducting spectrometer designed for millimeter-wave signals in a wide bandwidth of 335-377 GHz with spectral resolution (R $\approx$ 380) [Laguna, 2022]. It employs a dual-slot antenna to capture linearly polarized radiation, guides the received signals through a terahertz coplanar waveguide, and then splits them into 49 sub-bands for analysis using NbTiN-Al hybrid MKID detectors. In this case, the dielectric is amorphous silicon (a-Si).

SuperSpec SuperSpec is a 50-channel spectrometer integrated on a chip, functioning within the narrower frequency range of 255-278 GHz with a resolving power of approximately $R \approx 275$. Its operation begins with precise radiation focusing using a silicon lenslet with an anti-reflection coating, followed by coupling into a microstrip via a dual bow-tie slot antenna. The mm-wave radiation is further processed using NbTiN $\lambda/2$ filters, and the resulting currents are linked to a NbTiN-Al KID. Subsequently, these currents undergo detailed analysis within a microwave resonator circuit spanning 80-160 MHz before being connected to a coplanar waveguide readout line via an interdigitated capacitor for high-precision spectral analysis.

SPT-Slim SPT-SLIM is another filterbank-style spectrometer of $R \approx 300$ for 120-180 GHz designed on Si-rich SiN_x dielectric [Cecil et al., 2023]. Optical signals are coupled to the spectrometer via a feedhorn to an ortho-mode transducer (OMT) coupling. The signals from opposing OMT probes are combined in a hybrid tee, and the resulting signal continues down a microstrip transmission line. For each filter bank channel, one end of a Al-$\lambda/2$ channelizing resonator is capacitively coupled to the microstrip feedline. The other end of the channelizing resonator is capacitively coupled to the inductor of a Nb-NbN/dielectric/Nb LEKID that is used to detect the power in each channel and provides readout multiplexing.

3.2 Working principle

Conditions for our device Our device consists of superconducting circuits operating at temperatures significantly below the transition temperature of the superconducting materials employed, typically by a factor of 10, $T_{working} < T_c/10$. The detection frequency range of the device is spanning in between 75 to 110 GHz. The design can be upgraded to higher frequencies by changing the materials utilized and upgrading the design. We will focus on the description of the superconducting films employed.

3.2.1 On-chip spectrometer using Microstrip based Kinetic Inductance Detector (*OMKID*)

The schematic of the device is presented in Fig. 3.2. The incoming signal is coupled to a slot-shaped structure located in the ground plane, made of a bilayer of aluminum-gold ($\sim$ 400 nm) deposited at the back of a monocrystalline dielectric material. The slot shape serves as the antenna responsible for receiving signals within a specific frequency range (75-110 GHz). A 20 nm

thick aluminum microstrip transmission line located on the opposite side of the substrate is utilized to guide the electromagnetic signals out from the antenna. This design ensures efficient signal propagation while minimizing losses. The microstrip transmission line, referred to as the mm-wave line afterwards, matches the impedance of the slot-shaped antenna.
C-shaped filters, made out of a 20 nm thick aluminum layer, are positioned on both sides of the mm-wave line. These filters are capacitively coupled with the mm-wave line. Each filter is a $\lambda/2$ resonator tuned to a narrow frequency band of the incoming signal. Up to about 110 GHz, these filters are superconducting, i.e., they have zero losses. Thus, a high Q can be achieved.
Each filter is coupled to a lumped-element kinetic inductance detector, LEKIDs, designed to resonate in the readout frequency range of 1-3 GHz. Both the LEKIDs and readout lines are made of a TiAl bilayer, which has a lower transition temperature ($T_{c_{TiAl}} \approx 1\ K$) compared to 20 nm aluminum ($T_{c_{Al}} \approx 1.4\ K$). This lower transition temperature results in a lower superconducting gap frequency, approximately 70 GHz. Above this frequency, the superconductor behaves as a normal metal with a finite sheet resistance ($\sim 2\ \Omega/\square$). When the filter is on resonance, the maximum current is coupled with the meander lines of the LEKIDs. The current induced in the LEKIDs increases the density of quasi-particles by breaking Cooper pairs, causing a shift in the resonance frequency. The readout line, composed of the same bilayer material (TiAl), remains in a fully superconducting state since the electronics operate at frequencies from 1 to 3 GHz which are significantly lower than the superconducting gap.
This approach of utilizing coupled filters with antenna and LEKIDs serves as a spectrometric method for detecting the incoming signal.
The OMKID device, featuring a slot-shaped antenna with an mm-wave line feed, is polarization-dependent. This characteristic enables the device to select the incoming signals aligned parallel to the direction of the mm wave line itself.

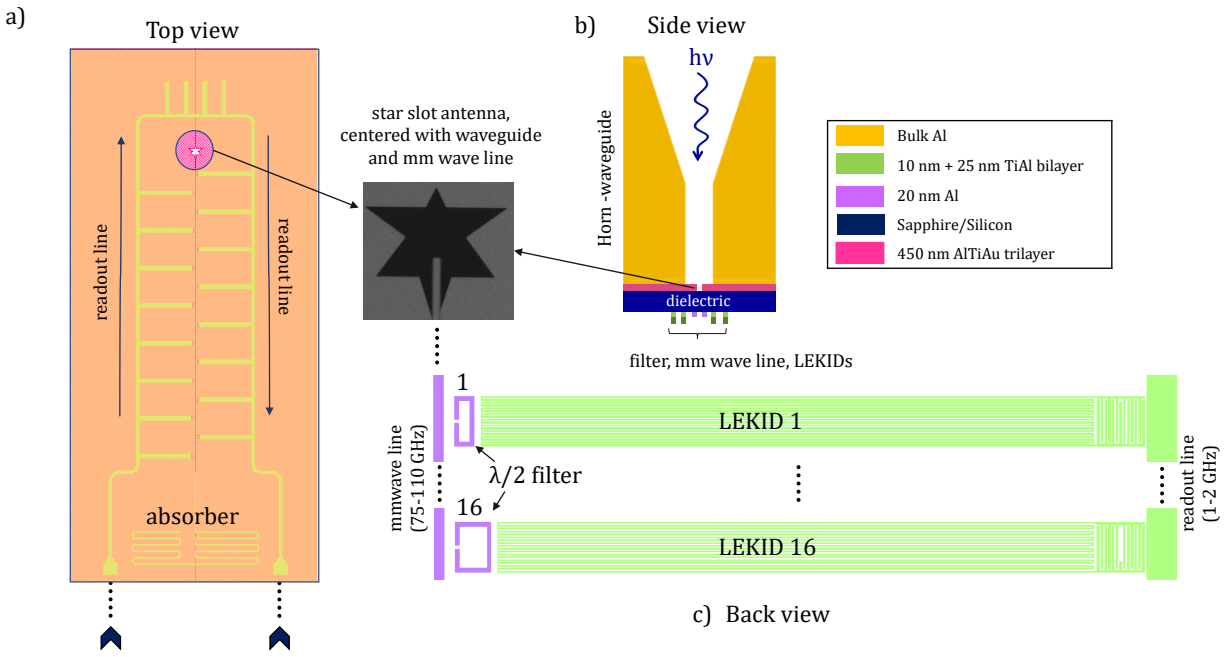

Figure 3.2: OMKID device schematic: (a) Top view and (b) Side view: The radiation is collected through a horn waveguide, a slot termination in the shape of a star on a sapphire substrate. The only visible part from the top is shown in the circle. The slot shape is fed through a mm-wave microstrip line that is placed at the center (shown in the inset). b) Back view: This Al-mm wave line is basically on the other side of the substrate, and it guides the signal further. The Al-made c-shaped filters pick up the signal from the mm-wave line. The filtered signal is absorbed by the LEKIDs, which are made of TiAl (with a superconducting gap of 70 GHz). The resonance frequencies of the LEKIDs are monitored with the readout line.

3.2.2 HYPerspectral device with Kinetic Inductance Detector (*HYPKID*)

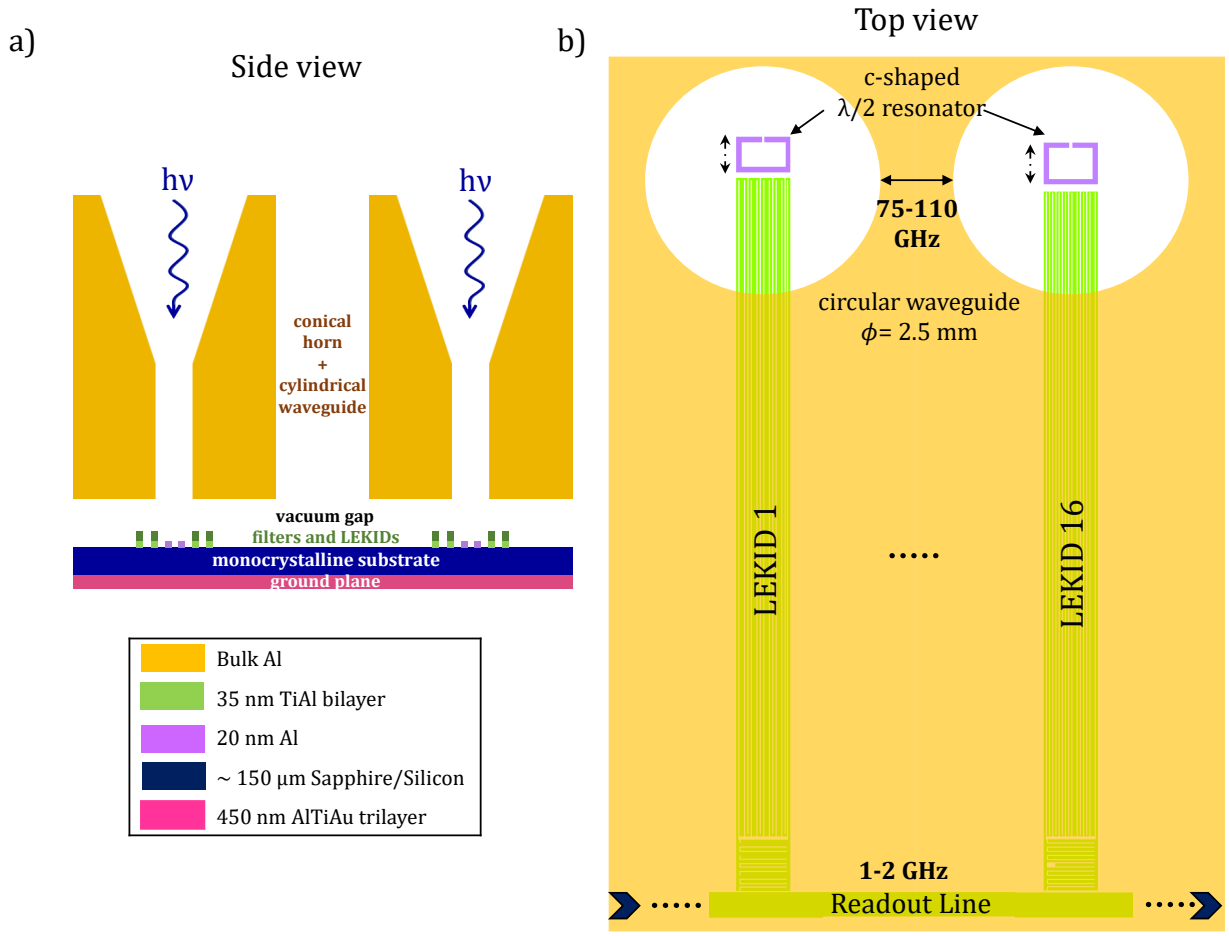

Figure 3.3: Schematic of HYPKID device: (a) Side view: The radiation is collected through a conical horn-circular waveguide radiating at the end towards the patterned superconducting layers level, realized on top of the sapphire silicon substrate. The ground plane is on the other side of the substrate. (b) Top view: The incoming radiation excites a resonance in the superconducting c-shaped $\lambda/2$ filter (tuned in between 80-110 GHz). The filtered signal is dissipated by the LEKID made of TiAl (spectroscopic gap around 70 GHz). The resonance frequencies of the LEKID are monitored with a GHz readout line (1-2 GHz).

The schematic design is shown in Fig. 3.3. The new HYPKID is derived from the OMKID as the idea originated during the measurement of the OMKID device. The working principle of signal flow from the filter to LEKIDs is the same. We eliminate the use of the slot and the microstrip line; instead, we directly illuminate the c-shaped filters to couple the incoming signal.

The incoming signal is focused on each filter with a conical horn-circular waveguide system. The waveguide has a cut-off frequency proportional to its radius. The cut-off frequency of the waveguide refers to the point at which the waveguide can no longer propagate certain frequencies due to its inability to fit within its dimensions.
The c-shaped filters, made of 20 nm aluminum, are positioned at the center of the waveguide at a given distance from its end. Their size determines the specific resonant frequency that is absorbed. They resonate with the incoming signal at their characteristic $\lambda/2$ frequencies as long as it is below the superconducting gap frequency of 20 nm aluminum of about 110 GHz. The filters are electromagnetically coupled with the LEKIDs (similar to OMKID). When the resonant frequency of the filter shape aligns with the incoming signal, it causes a noticeable change in the resonance frequency of the coupled LEKIDs.

3.3 Key elements of OMKID and HYPKID

We highlight the important points of our devices compared to these available devices that contribute to their effectiveness.

Monocrystalline Dielectric The presence of dielectric loss is a critical issue for integrated circuits that utilize deposited amorphous dielectrics, as it introduces two-level system noise at the readout frequency and losses in the mm-wave line. OĆonnell reported that the losses arise from the dispersion of absorbed energy at low power in the dielectrics [OConnell et al., 2008]. When considering the maximum power coupling between the filter and LEKID, the energy lost in the dielectric in this process is inversely proportional to the loss tangent of the dielectric. Addressing the issue of losses in the dielectric is essential to achieving a device with high efficiency. Several research groups are actively involved in the development of different deposited low-loss amorphous dielectric materials, such as a-Si:H [Buijtendorp et al., 2022a], a-SiC:H [Buijtendorp et al., 2022b], SiO_2, SiN_x. However, the loss tangent value for monocrystalline dielectrics is in general better when compared to any amorphous dielectric. In our research, we address this challenge by utilizing monocrystalline dielectric materials, specifically silicon and sapphire. These single crystals are free from grain boundaries and exhibit a predominantly uniform and defect-free structure throughout the solid. The use of high-resistive silicon, in particular, reduces the presence of impurities and dopants.

Fabrication steps By initiating our fabrication approach with a monocrystalline dielectric, we are able to reduce the processing steps involved, leading to a significant reduction in the overall number of steps required by other groups in general. This approach enhances efficiency and simplifies the fabrication process.

Simple and unique design We have opted for the microstrip-based device to avoid the slot mode present in the coplanar structures and the need for complicated micro bridges. A star-shape is engraved on the ground plane which works as a slot-antenna with a microstrip feed. The readout line is as well based on microstrip design.

Direct illumination on the filter For the HYPKID design, the direct absorption of the radiation signal by the filters reduces the losses in the intermediate elements.

Chapter 4

Device simulation and design selection

The OMKID and HYPKID devices consist of various subcomponents that contribute to the functioning of the spectrometer. Before incorporating them into the design, each component underwent simulation, in order to optimize the design parameters used in the device's fabrication and get a first estimation of the device's performance. In the following discussion, we will explore the working principles of each element.

Overall Simulation Approach We organize the simulations using a Top-Down approach. First, we simulate the components used to collect the incoming light (slot antenna, lens, and horn). Then the waveguide that is used, in the case of OMKID, to guide the signal towards the filters. We conclude by simulating the filters, which allow us to separate or "split" the different frequency sub-bands, and the LEKID detectors with the readout feedline which finally convert the incoming light into a traceable signal. Each component is device specific and will be discussed further.

Software Used To simulate the designs of the LEKID, filter, mm-wave line, and readout line responses, we used Sonnet [em], a 2.5D planar high-frequency electromagnetic simulation software. Sonnet is capable of simulating devices composed of multiple planar structures separated by dielectric layers and accurately accounts for the superconducting properties of materials. Sonnet uses a surface meshing technique, i.e., it meshes only the surface of the circuit metallization. The mesh elements for analysis are triangular or rectangular 2D structures.
For optimizing the slot antenna, horns, and waveguides, and for studying the coupling of filters to incoming radiation, we employed CST Microwave Studio [CST, 2002], another high-frequency software. CST is a 3D simulation software that allows the simulation of 3D structures of arbitrary shapes to extract circuit properties and visualize electromagnetic fields and surface currents using the 3D vector plot. Here, the mesh element is volumetric, i.e., tetrahedral or hexahedral 3D meshes over all the structure. The article [O'Rourke, 2015] is suitable for a detailed discussion about these two simulation softwares.

Considerations on the materials To achieve accurate results in both CST and Sonnet simulations, it is essential to assign appropriate values for material properties. When using Sonnet, one needs to provide values for metal losses (R_{dc}), kinetic inductance (L_s) and dielectric losses ($\tan\delta$) and the dielectric constant (ε) for the substrate. On the other hand, in CST, a metal can be described as a lossy material by representing it as an ohmic sheet with resistance and reactance values, while the parameters for dielectrics are the same as in Sonnet.
Initially, we used silicon as the substrate material for our simulation of OMKID. It has a dielectric constant of 11.9 and negligible dielectric loss. However, we encountered a fabrication issue, as explained in Chap.5 and decided to switch to sapphire. Sapphire is a suitable alternative to

silicon, with a dielectric constant of around 9.9 and a negligible loss tangent at low T. We aimed for thin silicon and sapphire substrates that can be used in the frequency range of 1-110 GHz depending on the working frequency of the planar circuits designed on these substrates, such as LEKIDs are operational in the frequency range of 1-2 GHz and the planar antennas or the filters are working in 75-110 GHz. The available sapphire is c-cut with an anisotropic dielectric constant. At low temperatures and high frequencies, the dielectric constant is $\sim$11.58 for axes parallel to the C-plane (XY wafer plane) and $\sim$9.48 for axes perpendicular to the C-plane.
As far as metal layers are concerned, we used thin superconducting films composed of Aluminum (Al) and Titanium Aluminum (TiAl) bilayer. As explained in Chap. 2 on superconducting properties, the properties of these materials are influenced by temperature, thickness and frequency. Our working temperature always remained significantly below the transition temperature. Therefore, below the superconducting gap frequency, the superconducting material exhibited zero resistive losses, but a finite impedance. Typical values are in the range of pH/$\square$ range at a consequence of the kinetic inductance of the material. However, when the frequency equals or exceeds the superconducting gap frequency, the same superconducting film behaves as a normal metal, with finite resistive loss. The metal components in the sample holder and ground plane are assumed to be perfect conductors.

4.1 Optical coupling

In this section, we present a detailed overview of the components employed in our device to efficiently gather incoming radiation and direct it towards the filter. The process of collecting incoming radiation involves carefully selecting a specific frequency range and then transmitting it to the subsequent part of the device. The primary focus here is on the star-shaped slot antenna used in our OMKID device. To enhance the performance of the antenna, we incorporate additional transition components, including Si lenses or horn-waveguides. These elements work in conjunction with the antenna to optimize its behaviour and improve overall functionality. Furthermore, for our HYPKID device, a similar transition approach is employed, but with distinctive perspectives tailored to its specific requirements. We will discuss the implementations for both OMKID and HYPKID separately, emphasizing their unique characteristics and contributions.

4.1.1 OMKID optical coupling

OMKID follows the design of the on chip spectrometer in which an antenna is used to transfer the incoming signal to the filter. We describe the star shaped antenna followed by different transitions in order to improve the collection of the incoming signal.

Star shaped slot antenna

The OMKID device incorporates a star-shaped slot antenna based on a microstrip design to enable its antenna functionality. A star shaped slot is positioned at the centre of a metal plane on a substrate. This metal plane with slot serves as the ground for the microstrip line located

on the other side of the substrate, with one open end aligned to the slot's centre. This arrangement shields most of the detector and minimizes direct signal absorption. The star shape was chosen as a first-order fractal structure in the OMKID prototype to achieve better efficiency and larger bandwidth.
The antenna operates in receiving mode within the frequency range of 75-110 GHz, with the microstrip line forwarding the coupled signal collected by the slot. For the ease in the simulation, we assess the antenna's performance in transmitting mode by exciting the microstrip to understand its behaviour. Thanks to the reciprocity theorem, we can infer that the antenna's performance in transmitting mode is equivalent to its receiving mode when measured in an isotropic, lossless, and linear medium. Therefore, we model and simulate the antenna performance in transmitting mode which can be equivalent in receiving mode. We conduct our simulations using *CST* software.

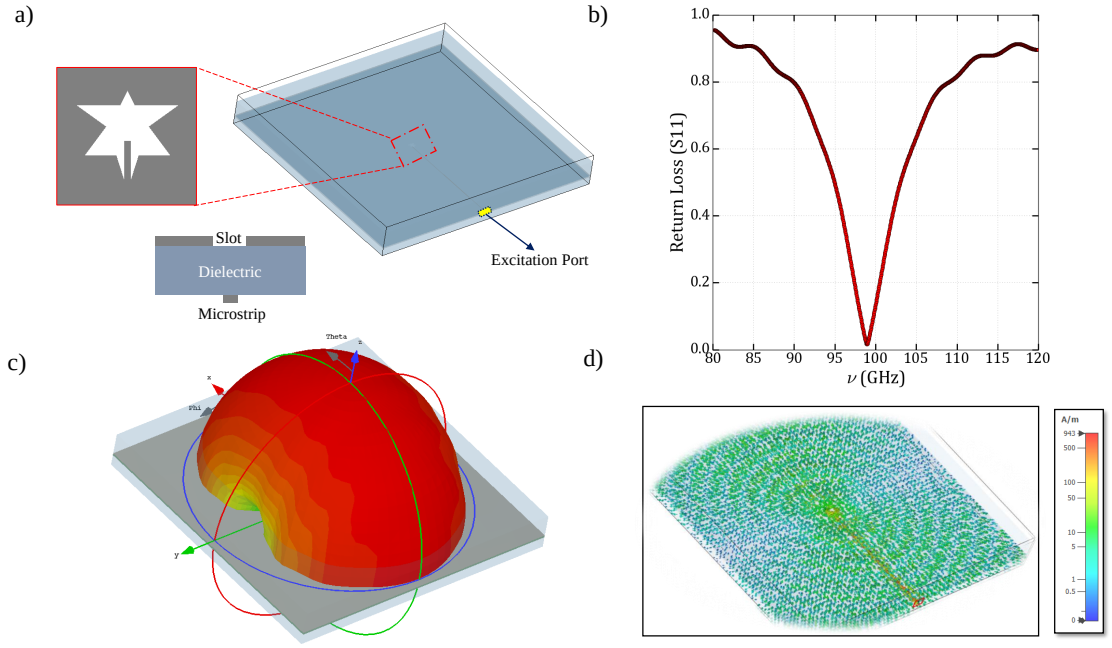

Figure 4.1: Antenna simulation: (a)The modelling of the star shaped slot with microstrip line (mm-wave line) in the CST Studio Suite. The excitation port is situated at the end of the microstrip line. Inset shows the star shape with the position of the microstrip. The side view shows the star slot at one side of the dielectric and strip line on the other side. (c) S11 parameter with center frequency around 99 GHz. (b) The far-field at 99 GHz from the top is shown. (d) The surface current when the microstrip mode is excited.

In the CST model, Fig. 4.1(a), the ground plane is taken as a perfect conductive layer (PEC) on the top of a sapphire dielectric. The slot, located at the centre of the ground plane, is fed by the microstrip line positioned on the lower side of the dielectric. In the superconducting

state, the microstrip works as perfect lossless superconductor with finite impedance. But for the excitation, we need perfect conducting part that connect the port. Therefore, the microstrip line is designed as an aluminum section representing 3/4 of its length with a surface impedance of 2 Ω/□ (which corresponds to the impedance of Al below the gap frequency at low temperature), and a PEC section representing 1/4 of its length, which terminates at the excitation port. The port at the end of the microstrip line functions as the feed for the slot shape in the ground plane, enabling transmission mode operation.
This model can be explained using the microstrip cavity model [Balanis, 2005], where the dielectric's bounding box acts as a cavity between two perfect conductors, the ground plane and the microstrip line. When the microstrip line is excited, the attractive and repulsive mechanisms between the charge distributions on the microstrip surfaces and the ground plane surface introduce surface currents along the periphery of the star. The slot's length along the microstrip line controls the central frequency, while its width variation determines the bandwidth. The position of the microstrip line's open end is then crucial to compose the desired frequency range. The radiation losses via the microstrip line due to the fringing field in the dielectric and the microstrip is reduced with substrates having high dielectric constant.
The scattering parameters (S-parameters) of the excitation port, the surface current at the open end of the microstrip line and the far-field behaviour provide an overview of the slot shape's performance. In Fig 4.1 (b), the magnitude of the return loss is depicted with respect to frequency when excited with microstrip mode. It can be observed that the star-shaped slot antenna with microstrip feed resonates at ∼ 98 GHz, with a bandwidth of 15 GHz.

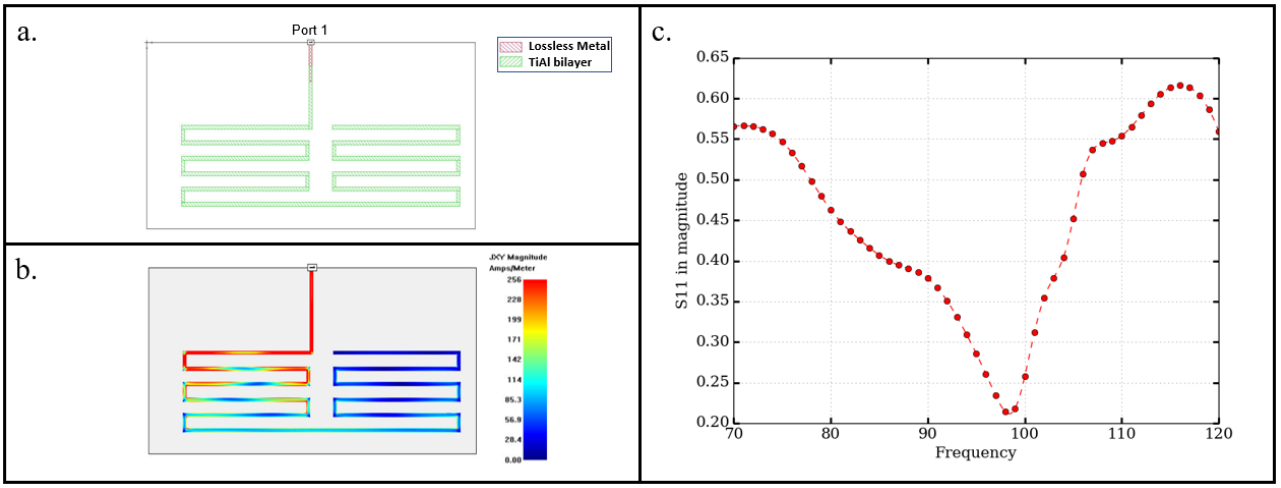

Figure 4.2: The absorber modelled (a) in *Sonnet* is shown with the current distribution at 90 GHz (b). Fig (c) shows return loss in the working frequency range.

Absorbers

In receiving mode, to reduce the reflections at the far end of the mm wave line and the consequent onset of standing waves, we terminate the line with an absorber. This consists of a

series of meandering lines of a lossy material. Fig. 4.2(a) shows a simulated prototype. Port 1 excites a strip of lossless metal, which overlaps with a conductor with a DC-resistance of 1 Ω/□ (corresponding to the normal sheet resistance of the Titanium Aluminum bilayer used). This property describes the behaviour of the films in the 75-110 GHz, where the Aluminum used for the mm wave line is superconducting whereas TiAl bilayer acts as normal lossy metal.
Fig. 4.2 (b) shows the current distribution along the line over the frequency. Between the mm wave line and the meander line, there is a small variation of impedance, so that a certain amount of reflection is observed. On the other hand, because of the lossy meander line, the part of the signal that propagates dissipates over the line. Thus, the current intensity is decreased along the path, with almost zero current at the end of the meander line.

Transition with Si lens

To further improve the collection of the signal on the slot shape, a hemispherical silicon lens of 4 mm radius on its surface has been used. The design of the lens ensures that parallel incoming rays converge at the centre of the flat surface. By maintaining the slot at this position, the antenna's performance is significantly enhanced. Fig 4.3 illustrates the simulation model depicting the slot shape with the integrated Si-lens.

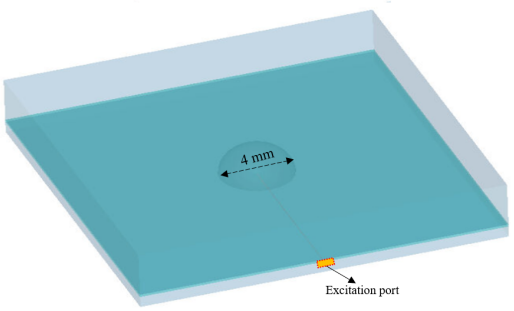

Figure 4.3: Simulation model for the slot with lens

Transition with horn and waveguide

An alternative approach to enhance the coupling between the signal and the slot antenna can be explored by simulating the behaviour of a slot coupled to a waveguide and a horn antenna. The waveguide is configured as a cylindrical metal box. In this setup, the transverse electric (TE_{11}) mode is the lowest frequency mode in the circular waveguide. The cut-off frequency ($f_{c_{11}}$) for this mode can be expressed as follows:

$$f_{c_{11}} = \frac{p'_{11} c}{2\pi a \sqrt{\varepsilon_r}} \tag{4.1}$$

where a is the waveguide radius, p'_{11} is a constant depending on the modes, c is the velocity of light and ε_r is the dielectric constant of the material used for the waveguide.

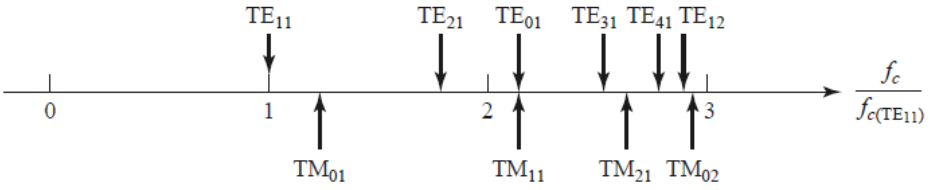

Figure 4.4: The frequency modes (f_c) in the circular waveguide vary according to the frequency of the dominant mode.($f_{c(TE_{11})}$) Taken from [Pozar, 2005].

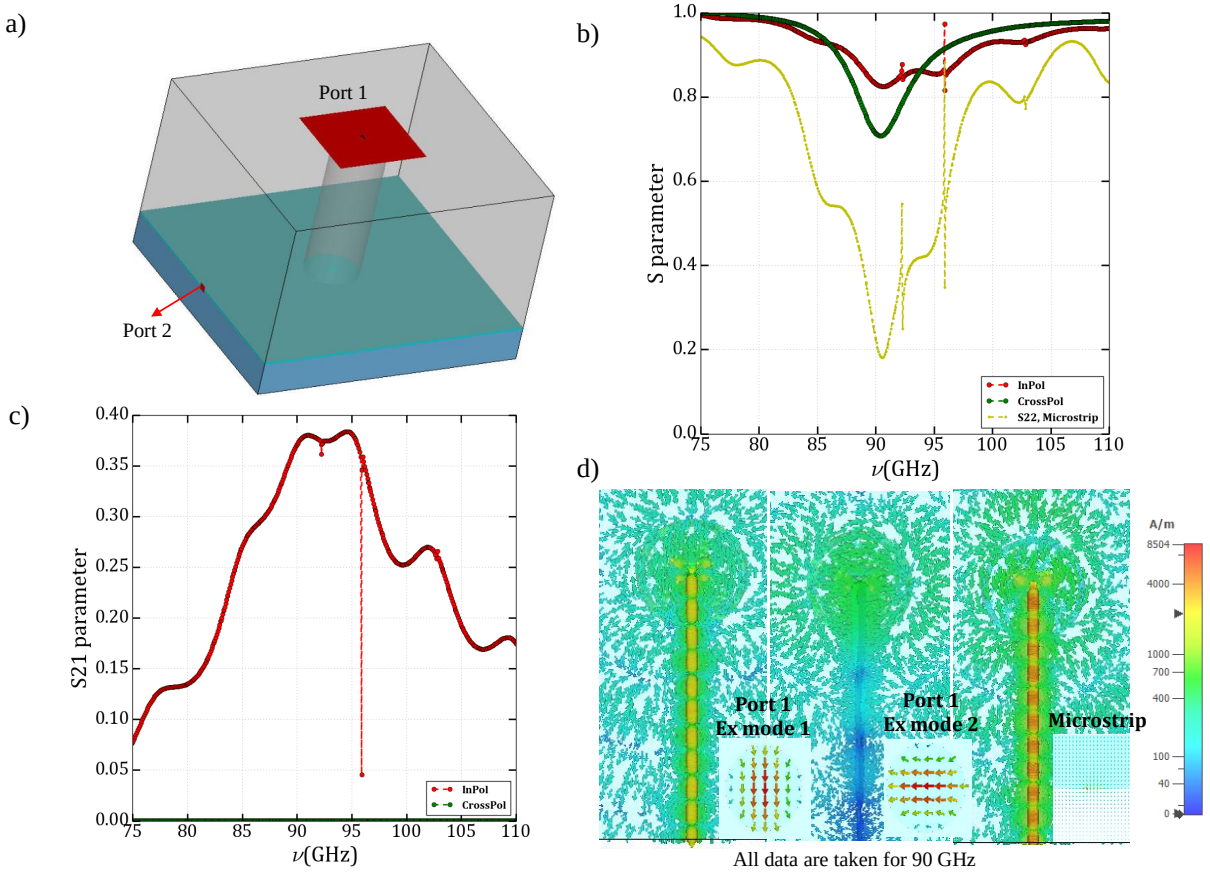

Figure 4.5: Simulation for the circular waveguide with the slot shape antenna.(a)The model used two excitation ports, Port 1 at the top of the circular waveguide and Port 2 at the end of the microstrip; (b) S parameters showing the reflections for two modes of Port 1 and microstrip mode. (c) The coupling efficiency between two ports is shown as S21 parameter of how transmission occurs when the excitation of Port 1 is transmitted to the microstrip mode. (d) The surface currents show the currents flowing in the microstrip in these three conditions i.e.; Port 1 with two excitations and microstrip mode (Port 2). In the inset, the corresponding port modes are shown.

In the case of a hollow circular waveguide of diameter 2.5 mm, the onset of the TE_{11} mode, occurs at approximately 70 GHz. Fig. 4.4 illustrates the relationship between the frequency at dominant mode(TE_{11}) and the frequencies at higher modes within the circular waveguide. It gives an idea about the position of the next modes within the working frequency range. As such, the next frequency mode (TM_{01}) arises before 70 GHz $\times$ 1.3 = 91 GHz and as seen from the simulation and calculation, it is around 90 GHz. The attenuation in the higher modes increases with higher frequencies.

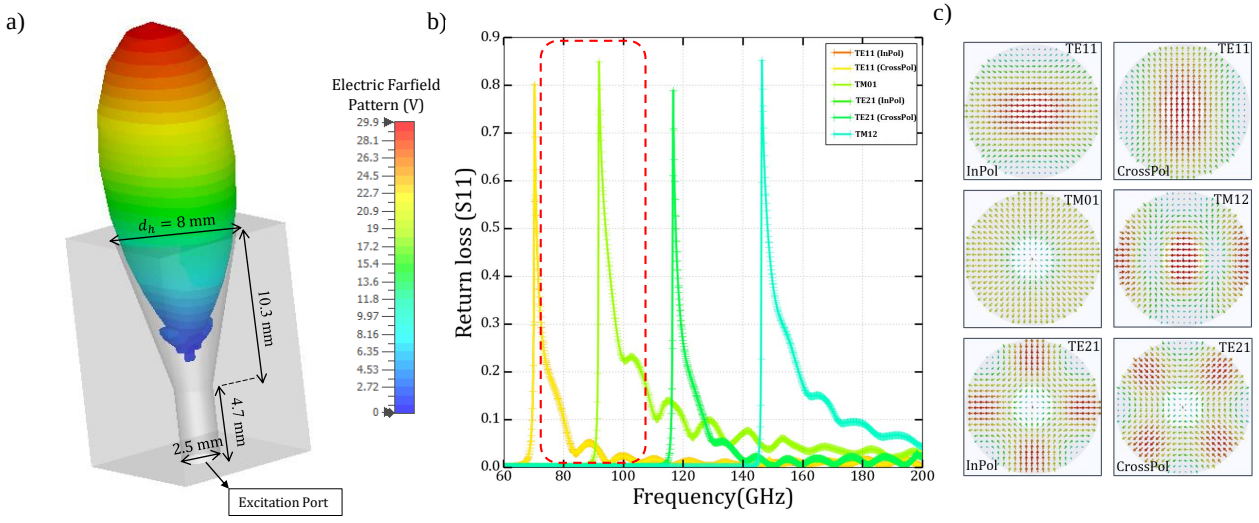

Figure 4.6: Conical horn with circular waveguide feed: (a) The schematic of the simulated design of the horn-waveguide set-up with the electric field pattern of the far-field at 73.7 GHz (active mode: TE11).(b) The return loss on the port for multiple excitation modes. The red dotted rectangle outlines the working range (75-110 GHz) needed for our device. (c) Six excitation modes used for the simulation.

In this simulation, we introduced an excitation port (Port 1) on the waveguide and another port (Port 2) at the end of the microstrip as shown in Fig. 4.5(a).
Panels (b) and (c) in Fig. 4.5 illustrate the return losses for the two distinct excitation modes of the two ports, as well as the corresponding distribution of surface current. In both excitation modes, the waveguide port (Port 1) is active and exhibits a clear cut-off at approximately 70 GHz. Additionally, it demonstrates coupling with the microstrip within the frequency range of 85-105 GHz. Conversely, the microstrip mode is active only for the excitation, parallel to its length.
The efficiency of the coupling is measured by the S21 parameter, which determines the extent

of signal coupling between port 1 and port 2, and vice versa. As depicted in Fig. 4.5(c), the coupled signal amounts to approximately 40%. The majority of the signal is lost due to reflections occurring on the metal part surrounding the slot shape.
When simulated in transmitting mode with one excitation port at the end of the waveguide, the input signal transfers from the port through the waveguide to the horn. This results in a far-field radiation at the end of the horn as shown in Fig. 4.6 (a). The conical horn has optimum directivity when its diameter (d_h) is equal to $\sqrt{3l\lambda}$ where l is the axial length and λ is the wavelength [Balanis, 2005]. The radius of the waveguide selects the modes that are propagating. Whereas the length of the waveguide effects the efficiency of the wave propagating as per the effective electrical length. We opted for a 4.7 mm long circular waveguide with 2.5 mm diameter. This introduces the cut-off frequency of 70 GHz, with a single mode(TE_{11}) until 91 GHz (TM_{01}). The horn diameter is 8 mm with the axial length of 10.3 mm. The aperture efficiency of this horn antenna is around 60 %. In the simulation, the excitation is applied at by the port at the end of the waveguide using six different modes as shown in Fig. 4.6(c).

4.1.2 Optical coupling for HYPKID

The goal of HYPKID was to maximize the end to end efficiency (reducing the losses in OMKID). This can be achieved by a feed system of the conical horn followed by the circular waveguide, mirroring the configuration employed in the OMKID device. In the case of OMKID, the waveguide directly terminates at the ground plane with the slot placed at the centre. In contrast, for HYPKID, the filter is positioned at the centre of the guide shape with a gap between the end of the waveguide and the filter structure.

4.2 Filters

In our devices, c-shaped half wave resonators serve as filters that allow specific frequencies from the incoming signal to be transmitted to the LEKIDs, thereby determining the spectral resolution.
The half wave resonator is commonly used as band selective filters in microstrip transmission lines, exhibiting its fundamental resonance mode when its electrical length (L) is precisely half of the guided wavelength (λ_g), given by $L = \lambda_g/2$. Similarly, the c-shaped filter, serving as a half wave resonator, features a straight line bended for geometrical reasons into a rectangular loop with two open ends. On resonance, the incoming signal is coupled into the resonator via the mm-wave line near the open end, leading to the formation of standing waves inside the structure. From the current distribution, it can be shown that the open ends experience a zero current point and maximum voltage. The filter is connected to the LEKIDs on the opposite side, as illustrated in Fig. 4.7(c), near maximum current distribution. The gap between the open ends introduces a fringing capacitance, which controls the effective length of the design. Therefore, the resonator is not a pure $\lambda/2$ resonator. For tuning the resonance frequencies of the filters in between 80-110 GHz, the side length (l) has been varied. The filter simulations for OMKID have been carried out using Sonnet software.

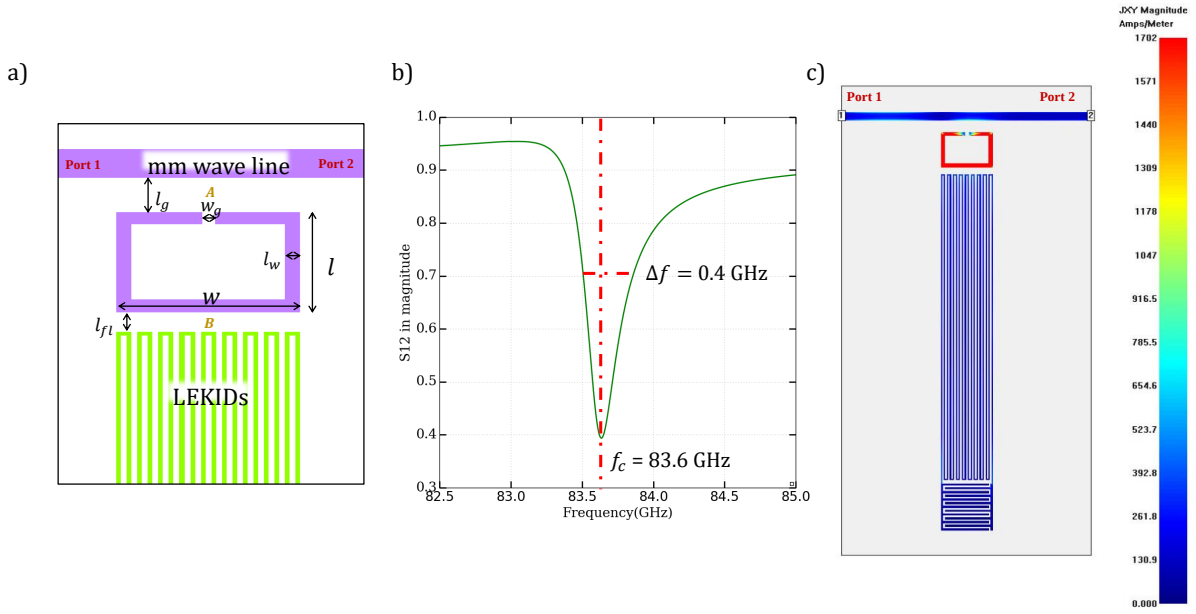

Figure 4.7: C-shaped filter: (a) The schematic diagram used in the Sonnet simulation. l is the side length that has been varied for tuning the resonance frequency, l_g and l_{fl} can be varied to adjust the strength of the coupling. A stronger coupling corresponds to a wider resonance width. This parameter is used to fix the resolution of the spectrometer. (b) The S21 transmission parameter of the filter for side length, l =151 μm. The resolution is given by, $\frac{f_c}{\Delta f}$ = $\frac{83.6\ \text{GHz}}{0.4\ \text{GHz}}$ = 209. (c) Current distribution in the filter at the base resonance frequency.

The coupling gap between the mm-wave line and the filter (l_g) isolates the incoming signal from the feedline and selects specific frequency (resonance frequency) depending on the total effective length of the c-shape. The gap between the filter and LEKID (l_{fl}) couples the resonant signal with the LEKIDs. The selection of the length of this gap is tricky and optimized through multiple simulations. Opting for a minimum gap diminishes losses or increases Q factor, yet influences the fields within the resonant structure, i.e. changes the resonant frequency. On the other hand, a wider gap minimizes field perturbation while increasing losses. We optimize for a distance to have a resolution around 200. The larger the percentage of the surface area of the filter the coupling region occupies, the greater the effect on the filter's performance. We designed in such a way that the filters are in increasing order in the mm wave line with the maximum area coverage for the meandered LEKIDs.
For the HYPKID design, the filters maintain the same geometry. The only radical difference is that the incoming signal is directly fed from the feed system of horn and waveguide to the filters. The distance between the waveguide end and the ground plane depends on the sample holder design and the wafer thickness. This vacuum gap is around 700 μm for HYPKID on the sapphire device. We decrease the vacuum gap by placing a 'spacer', double sided metal

deposited silicon wafer of thickness 275 μm. This hardly affects the absorption efficiency as shown in Fig. 4.9. Fig. 4.8 shows the absorption efficiency of the filters for the side lengths varied from 135 μm to 170 μm. The spectral resolution varies from 100-300 and the absorption efficiency is around 80 % over the range.
In both cases, when the resonant frequency is reached, the energy is coupled to the filter and dissipated by the meander lines of the LEKIDs. This leads to an increase in the quasi-particle density within the LEKIDs and a shift in their resonance. This can be measured using the readout circuit.

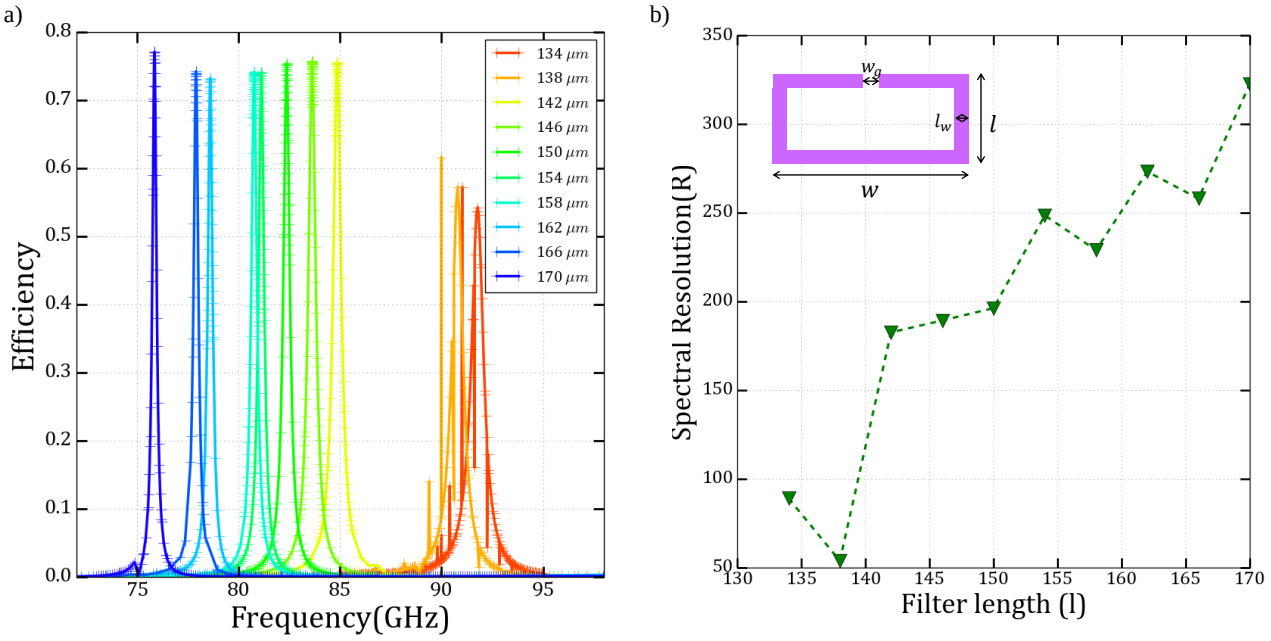

Figure 4.8: Simulation of the side length(l) of the c-shaped filter for the HYPKID design where the signal is directly illuminated on the filter shape.

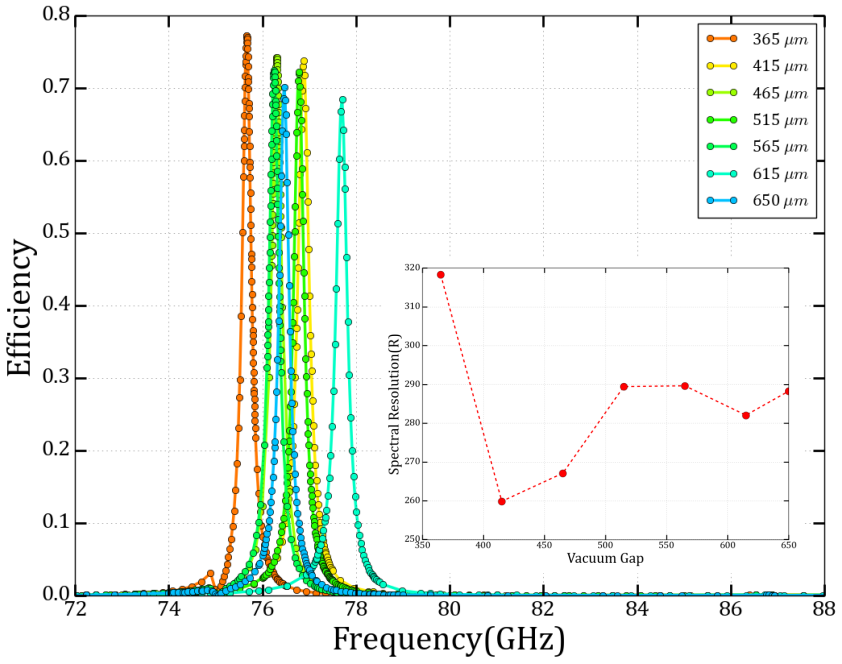

Figure 4.9: The gap between the waveguide end and the filter is varied from 365 μm to 650μm and the corresponding efficiencies of the filter is shown. In the inset, the consecutive spectral resolutions are shown.

4.3 Detectors: the LEKIDs

The LEKIDs structure is the same for both the OMKID and HYPKID devices, but their simulation setups differ due to the presence of different elements nearby, such as the ground plane or waveguide. The substrates also vary depending on the device. The simulation setups are depicted in Fig.4.10.
For the OMKID device, the setup involves placing LEKIDs on one side of the substrate. A lossless metal layer acts as the ground plane for the microstrip structure. Additionally, a vacuum layer is positioned in front of the device.
In the case of the HYPKID device, a metal plate is introduced above the vacuum layer. This metal plate covers half of the LEKIDs, mimicking the waveguide section on top of the LEKID. The remaining portion without the metal plate represents the hollow part of the waveguide. The LEKIDs and readout lines are designed as metal layers with a DC resistance (Rdc) of 5×10^{-7} $\Omega/\square$ and a kinetic inductance (Ls) of 2 pH$/\square$. These values represent the properties of a TiAl bilayer operating as a superconductor within the frequency range of 1-3 GHz. The metal plates representing the waveguide and the ground plane are perfect conductors. The width of the readout line (discussed in the next section) ranges from 100-120 μm to achieve a 50 Ω microstrip line. Two ports (P1 and P2) are added at the ends of the line. The distance

between the capacitor and the readout line was varied to study the coupling quality factor of the LEKIDs. In the final mask design, a distance of 10 μm was chosen to achieve $Q_c = 10^5$ that matches the typical Q_i of TiAl LEKIDs.

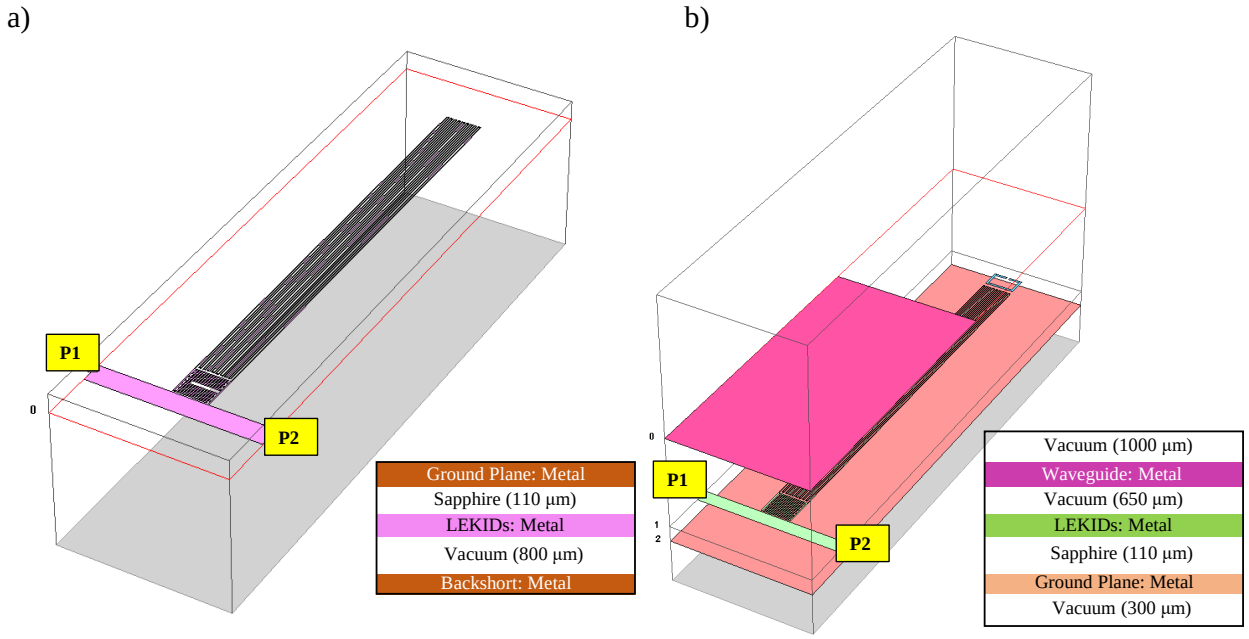

Figure 4.10: Schematic simulation model of a LEKID: Schematic diagram of the *Sonnet* simulation of LEKID for OMKID (a) and HYPKID (b): The LEKID is on the sapphire substrate of thickness 110 μm, with different vacuum gaps and settings. The two ports (P1 and P2) are situated at the end of the readout lines.

The filters are electromagnetically coupled with the LEKIDs at resonance with a gap distance of 30 μm. The total spatial width of the LEKIDs are controlled by the total width of the filter as discussed in the previous section. To maximize the inductance of the LEKIDs, and increase the effect of L_k, the kinetic inductance, the meander line should be long and thin. The lowest possible unit is precisely determined by the fabrication process. To mitigate the defects on the long meander, we opted for a width of 4 μm. The separation between the two adjacent

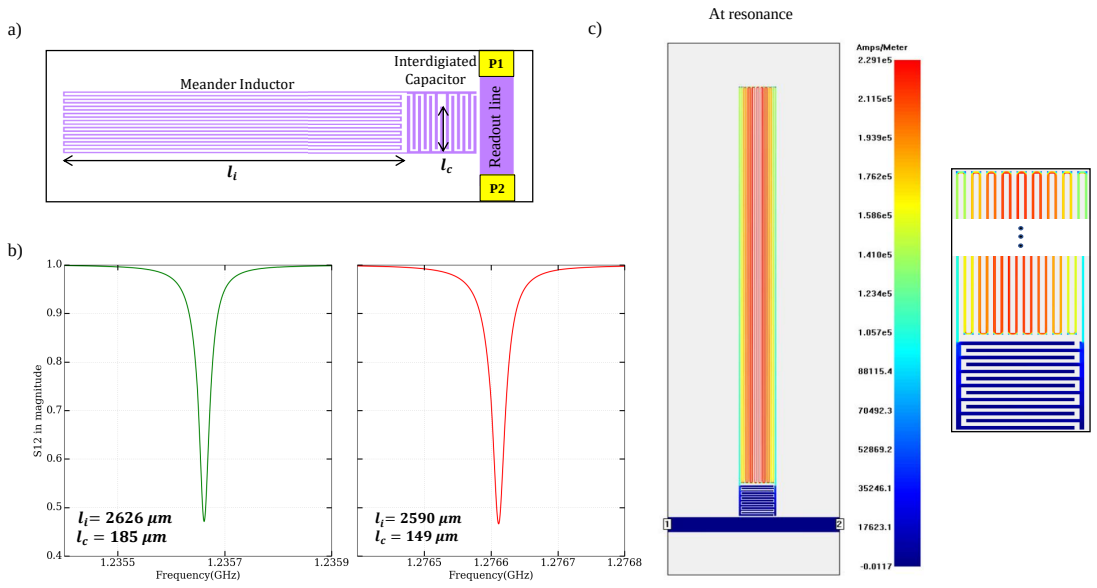

Figure 4.11: Simulation of a LEKID: (a) A simplified LEKID with tuned lengths (b) The simulated resonance frequencies of the LEKIDs are shown for two different configurations of the meander line length (l_i) and one of the middle finger of the capacitor length(l_c). The LEKIDs designed for HYPKID are in between these two extremes. (c) This figure shows the current density in the meanders of LEKIDs at resonance frequency. The zoomed view displays the density of the current in the lines.

meanders is 8 μm. We stress here that the meanders do not act as direct light absorbers, where their length would match to the free space impedance. Our main goal was choosing a suitable coupling between filter and meander lines. The gap between each meander lines was 8 μm. With this choice, the surface area of the LEKIDs coupled with the filter maximizes the coupling. The total number of meander lines are fixed by the gap distance, i.e., the separation between the two adjacent meanders. The meander shape ensures uniform current density at resonance.

The choice of the resonating frequencies of the LEKIDs are driven by the readout frequency of the available electronics and readout chain (0.5 GHz - 3 GHz). We fix the inductance by changing the meanders length and width. Thus the capacitance of the LEKIDs must be such that the LEKIDs resonance frequency must comply within the electronics range. We use interdigitated digital capacitor (IDC) to close the LC circuit. The fingers of the interdigitated capacitor (IDC) are 184 μm long, 8 μm wide with comb-like shape with a gap width of 8 μm. The number of fingers is 13.
The LEKIDs are designed to occupy a frequency range of 80 MHz for the case of OMKID (16 channels). For HYPKID, we choose to have 20 MHz frequency band for 19 channels, for future

design. The length of the meander in the OMKID varies in between 2551 μm to 2626 μm in steps of 5 μm for 16 spectral channels. The length of finger in the middle was varied as well in between 35 μm to 185 μm. For HYPKID design, the length of the LEKID lines (l_i) varies from 2590 μm to 2626 μm in steps of 2 μm. The length of the middle finger of the IDC (l_c) was varied between 149 μm to 185 μm in steps of 2 μm. Fig. 4.11(c) shows the uniform current density distribution at the resonance frequency. On resonance, the energy transferred to the LEKID from the readout line reaches its maximum.
The distance between two LEKIDs is also critical parameter to reduce the crosstalk. Over the mm wave line, the distance between two LEKIDs was around 800 μm for OMKID. In simulation, there were no crosstalk found between two lines. In the case of the HYPKID, the distance is fixed by the horn size and is several mm.

4.4 Feedline

The LEKIDs are capacitively coupled with the readout line. The distance of the last capacitive finger closest to the readout provides the coupling quality factor of the LEKID. The Q_c value increases with this distance, and at the same time, the coupling with the readout line becomes weaker. The width of the readout microstrip line is determined by the substrate's thickness, which fixes the characteristic impedance. Meanwhile, the physical length is influenced by the width, substrate permittivity, and operating frequency. In this particular case, the feedline is a 50 Ω microstrip line with a width of 128 μm. To mitigate unwanted radiation, the feedline is intentionally curved in its bending sections. We chose the radius of the bending curve to be around 800 μm which is almost 3-4 times the width of the microstrip.

4.5 OMKID and HYPKID design

The design prototypes for both OMKID and HYPKID were created based on simulations. For OMKID, we use three different masks as shown in Fig. 4.12. Whereas for HYPKID, we use two masks to implement different parts as in Fig. 4.13. Each device consists of 16 spectral channels, with the dark channels directly coupled to the readout line. In the case of OMKID, there are four dark channels, while HYPKID features three dark channels that is without any filters. The patterning masks were created using layout editing software such as *L-Edit* and *CleWin*.

(in μm)	Line width	Gap width	Pitch	Total width	Coupling distance
Filters	16	16	-	208	50
LEKIDs	4	8	8	208	30
Capacitors	8	8	8	184	10

Table 4.1: The design parameter for filters, LEKIDs and capacitors.

We select the parameters of the detectors by simulation. The basic parameters shown in 4.1 are fixed for both OMKID and HYPKID. The pitch refers to the separation gap between two consequent lines. For OMKID, the filter is coupled with the mm-wave line, the meander of the

LEKID is with the filter, and the interdigitated capacitor (IDC) is with the readout line. We referred to the corresponding coupling distances above.

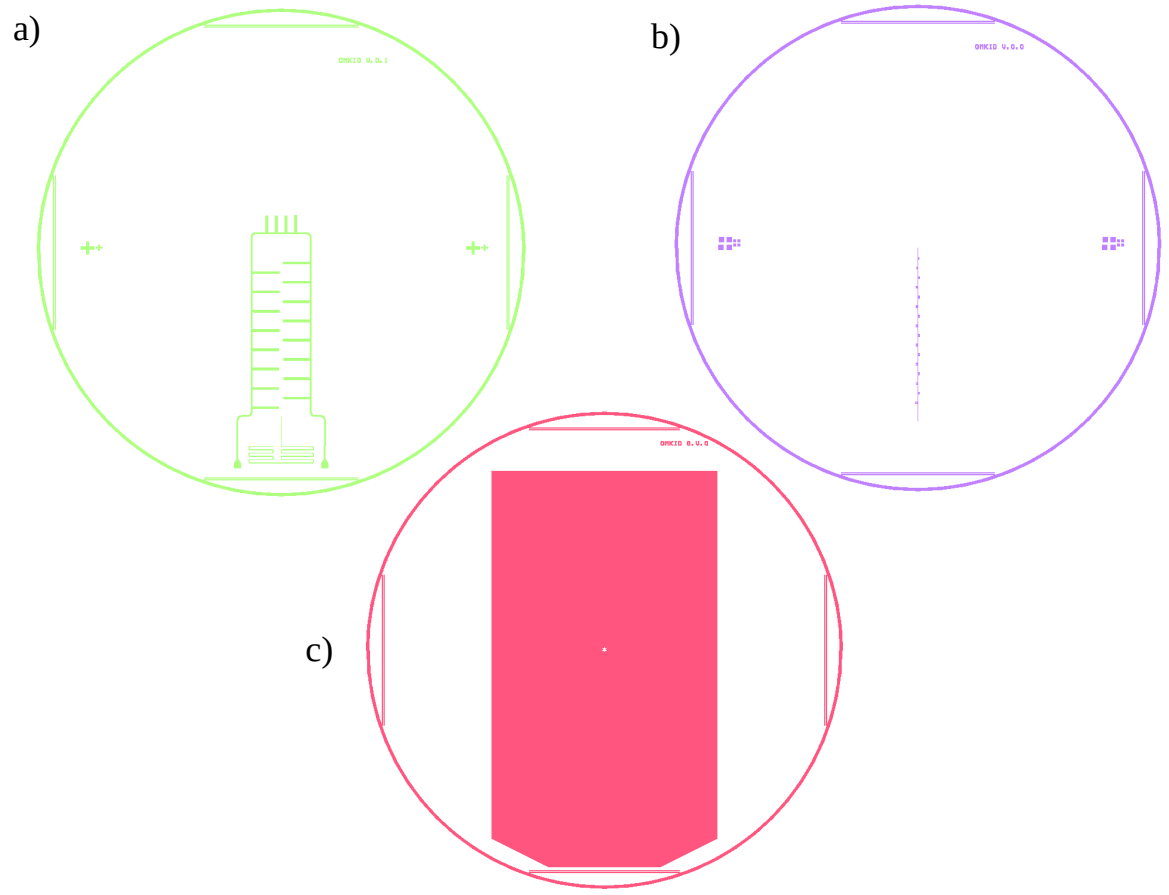

Figure 4.12: The mask design for OMKID: (a) The first mask with readout line, LEKIDs and absorber. (b) The second mask with filter and mm wave line, (c) The third mask with the slot shape.

	No. of total LEKIDs	Dark LEKIDs (No filter)	Minimum to Maximum Length in μm for		
			Side length of filter	External line of meander	Middle finger of IDC
OMKID	20	4	76-151	2551-2626	35-185
HYPKID	19	3	134-170	2590-2626	149-185

Table 4.2: The parameters used for designing the channels for OMKID and HYPKID devices.

We have used dark LEKIDs for test measurements. These are without any resonators. To keep the distance of the distance between the mm-wave line and readout line fixed, the filter length

was increased while the inductor length was decreased. It has given us the opportunity to simultaneously tune the filters and the LEKIDs. The parameters used are shown in Table. 4.2. The middle finger of the capacitor was also changed simultaneously with the meander length to acquire an optimized distance between two consequent resonances in the readout frequency.

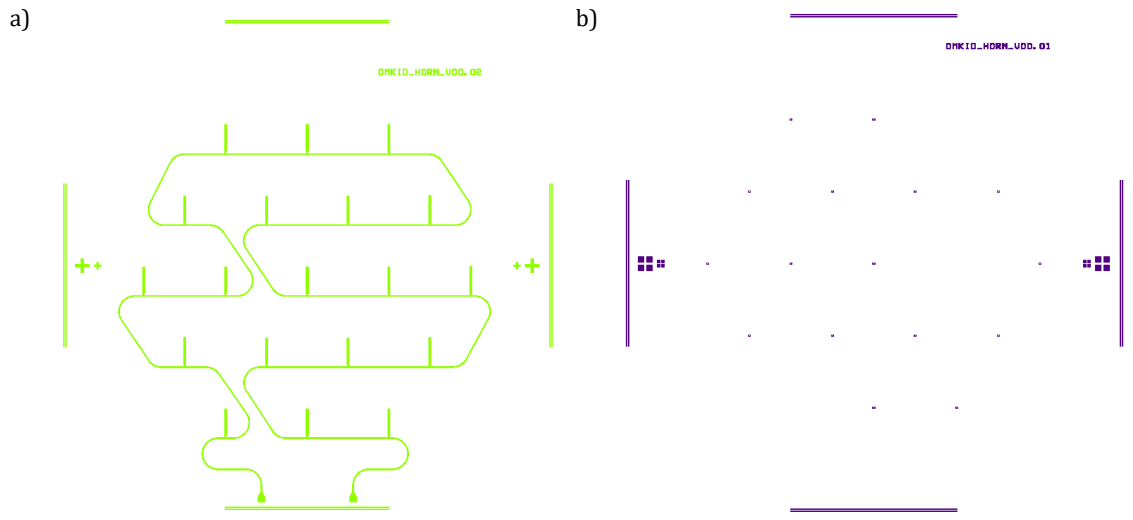

Figure 4.13: Masks for HYPKID: (a) The first mask is used for LEKIDs and readout line, (b) The second mask is used for filters.

Chapter 5
Fabrication

The designed device is divided into multiple masks for the fabrication process. Each represents the pattern for a specific layer. In our particular case, we had three distinct layers to deposit, as discussed in 4.5. This chapter will focus on the fabrication process specifically related to these three layers. The production process took place in a clean room environment and played a significant role in the overall outline of this thesis.

5.1 Dielectric Substrate

We employed two types of low-loss monocrystalline dielectrics, namely silicon and sapphire.
High resistivity silicon refers to intrinsic monocrystalline silicon with a bulk resistivity exceeding 1-5 kΩ.cm at 300 K. It exhibits low loss tangent and a high effective dielectric constant ($\varepsilon = 11.9$). The utilization of high ε material helps minimize the radiation losses by concentrating the electromagnetic field within the dielectric.
Sapphire, on the other hand, is a transparent, monocrystalline material with low-loss characteristics and an equally high dielectric constant ($\varepsilon = 9.9$). Its unit cell displays high anisotropy. For our purposes, we selected sapphire with a C-cut, where the dielectric permittivity only varies along the c-axis or Z axis i.e, the dielectric constant is isotropic in the wafer plane. This cut is the most popular for microelectronics and photonics applications.
For OMKID, the reason behind choosing sapphire instead of silicon is the transparent property of sapphire. We need to align between the slot shape and the microstrip at a certain point in our processing (discussed in Sec. 5.4). It would have been a complicated process if we had chosen the two sided alignment system for the lithography process. However, by choosing sapphire, which has similar dielectrics properties as silicon, we were able to solve the misalignment issue.

5.2 First Lithography Step: LEKIDs, absorbers and Readout line

The fabrication process commences with a 2-inch commercial substrate. Prior to initiating any further steps, we verified the thickness of the substrate using a micrometer. The LEKIDs served as a crucial component of the device. The quality factors of the device heavily rely on having a clean interface between the dielectric and the metal layers. Consequently, it was decided to prioritize the deposition of this initial layer on the pristine wafer before carrying out subsequent processes. The substrate was cleaned using an ion-beam etching process, which was conveniently performed in situ within the evaporation system. Fig. 5.1 shows the schematic views of the first lithography steps. The steps are detailed in the next paragraphs.

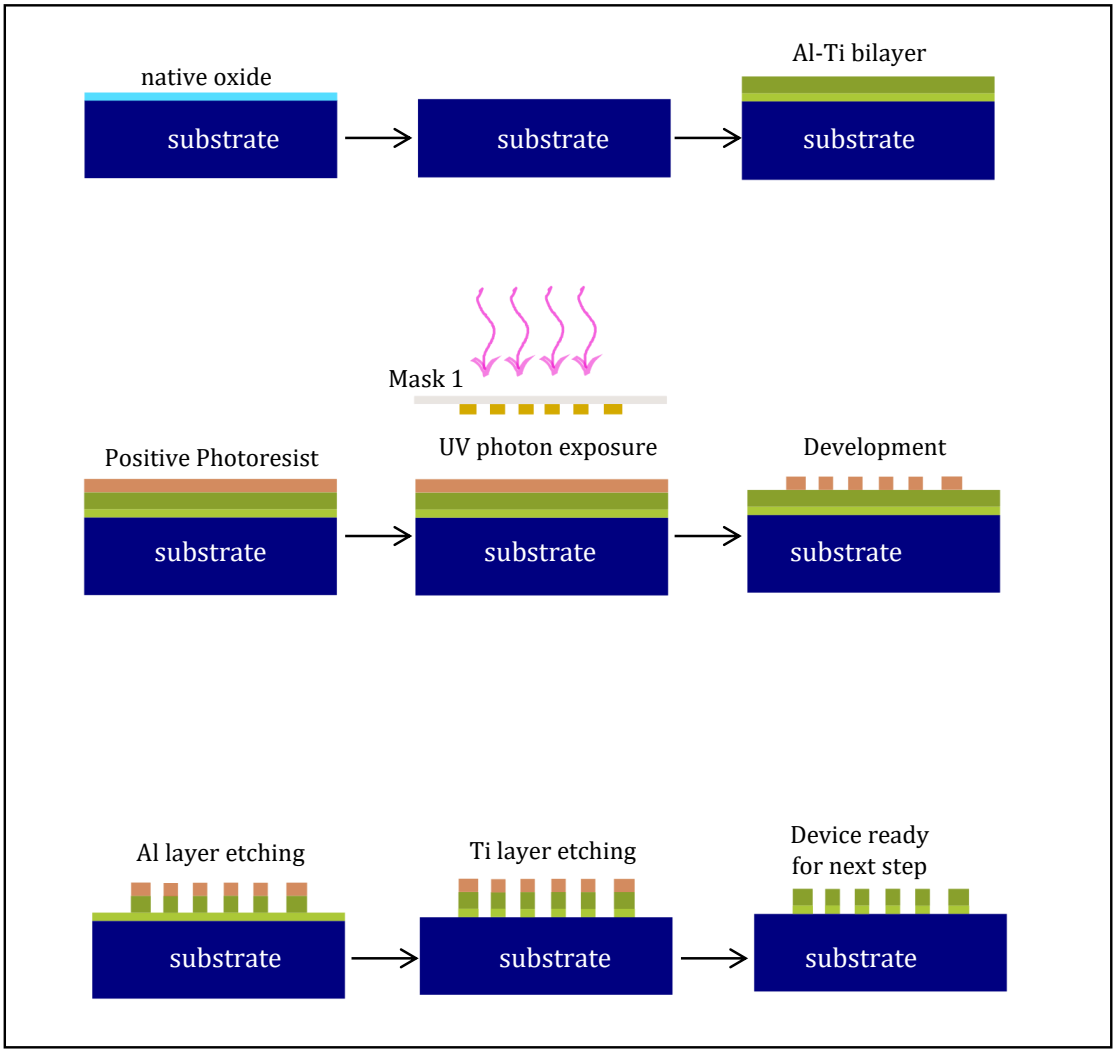

Figure 5.1: Fabrication procedures employed for the LEKIDs, mm wave line and absorbers outlined by the first mask.

Step 1: Deposition The Plasyss MEB550 metal evaporator system, a physical vapour deposition unit, utilizes thermal evaporation with an electron beam and offers various other capabilities such as ion-beam etching and oxidation facilities. At first, the substrate underwent a 2:30 minute etching process utilizing argon ions (Ar+) to remove the native oxide layer (SiO_2) in the case of silicon. In the case of the sapphire substrate, it aimed to eliminate any hydrocarbon and fluorine contamination. The rate at which the oxide layer is etched depends on both the ion beam voltage and the sample's angular position. In our case, when using a beam

voltage of 300 V, beam current of 14 mA, and an accelerating voltage of -60 V at a pressure of 10^{-4} mbar, the typical etching rate for SiO2 is approximately 1.5 nm per minute.
To maintain the vacuum integrity, a 10-nm thick layer of titanium (Ti) was deposited onto the substrate at a rate of 0.25 nm per second. Subsequently, without breaking the vacuum, a 25 nm thick layer of aluminum (Al) was deposited on top of the Ti layer. This process protects the Ti layer from oxidation. During the deposition process, the sample holder was rotated at a rate of 5 rpm to ensure a uniform deposition. The working pressure was less than 10^{-7} mbar during the whole process.

Step 2: Patterning The deposited bilayer undergoes a spin-coating process using AZ1512HS positive photoresist. It was then subjected to a soft-baking step at 100 °C for 2 minutes to cure the resist and prepare for exposure. The photoresist undergoes a chemical reaction upon exposure to UV radiation, rendering that area soluble in the developer solution while acting as a protective layer in the unexposed regions. The first mask was employed for the optical lithography process.
In the MJB4 mask aligner, the photoresist layer was exposed to UV light for 22 seconds while in soft contact with the mask. Following this, the pattern was developed using AZ developer diluted with deionized (DI) water in a 1:1 ratio for 40 seconds, causing the exposed layer to dissolve into the solution. The sample was then thoroughly rinsed with DI water and dried using nitrogen gas (N_2). A post-baking step was carried out at 120 °C for 2 minutes to harden the resist for the next step.

Step 3: Etching The unmasked region underwent an etching process using a suitable etching solution (discussed in Sec. 5.5) for about 40 seconds to remove the aluminum (Al) layer. Following that, a diluted hydrofluoric acid (HF) solution with a concentration of 0.1% was applied for about 30 seconds to remove the titanium (Ti) layer. The sample was meticulously cleaned using deionized water in a resistivity bath tub up to 12 MΩ to ensure the removal of any remaining etching solution, and then it was dried using nitrogen gas (N_2).

5.3 Second Lithography Step: filters and mm wave line

The alignment of the second layer with the first is crucial.To accomplish this, a positive mask (mostly transparent) and image reversal photoresist are utilized. The image reversal photoresist consists of a two-step process in which the areas protected by patterns in the mask undergo photo excitation and dissolve in the developer solution, thereby exposing those specific areas. This enables the metal to be deposited and patterned. As the minimum feature size of our second mask is around 16 μm, it can be lifted off without issues. In general, the lift off process would allow realising feature dimensions down to 5 μm wide. The steps elaborated in the next paragraphs are illustrated in Fig. 5.2.

Step 4: Patterning The sample, which has been patterned with the LEKIDs, undergoes a spin-coating process with AZ5214E photoresist. Subsequently, it is subjected to a pre-baking stage at 100°C for 2 minutes. Using the second mask, UV light is exposed to the photoresist

for a duration of 5.5 seconds.
The photoresist is then baked for 2 minutes at 120°C. During this step, the exposed resist loses its ability to develop. The sample is flood-exposed to UV light for 33 seconds without a mask, causing the previously unexposed areas from the first exposure to become reactive and susceptible to development. The sample is then developed using a solution consisting of AZ developer and distilled water in a 1:1 ratio for a duration of 40 seconds. As a result, the photoresist remains on the areas of the sample that are exposed to UV light.

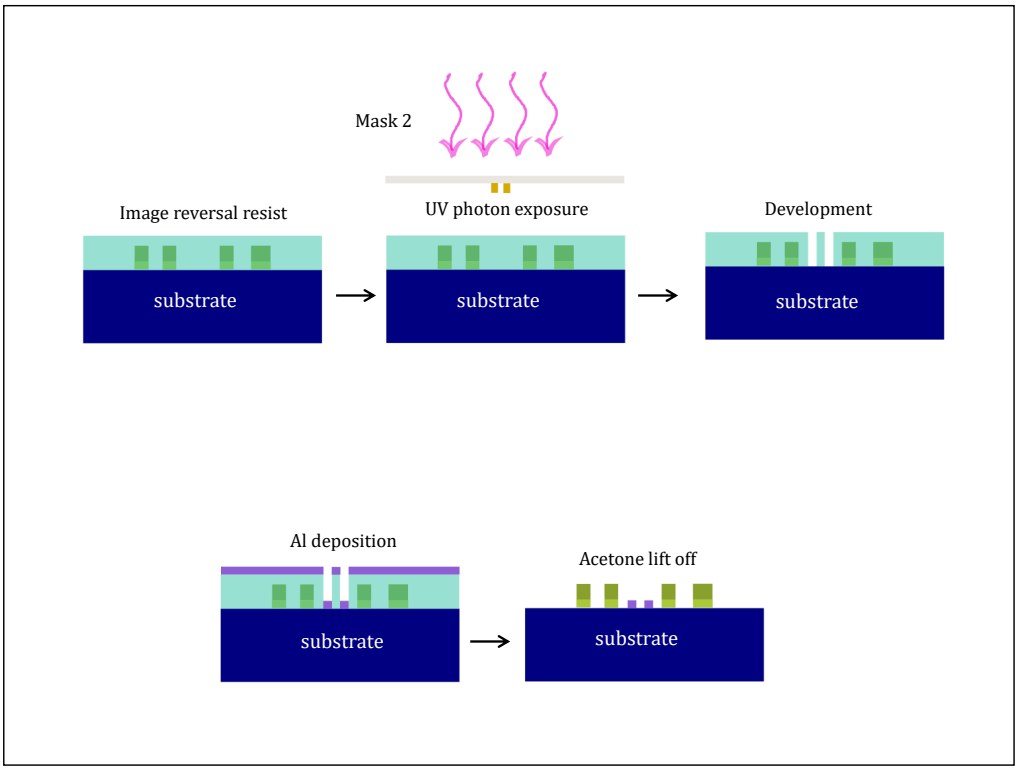

Figure 5.2: Fabrication steps followed for the filters and the readout line with the second mask.

Step 5: Deposition An aluminum layer of 20 nm with a deposition rate of 0.25 nm/sec and usual substrate spinning is deposited on the resist pattern using the same MEB550 metal evaporator system.

Step 6: Lift-off The layered sample is immersed in an acetone bath for a duration of 20 minutes. Acetone dissolves in the resist and allows the removal of the metal that was deposited on top of it The sample is inspected for any residual debris and undergoes a cleaning process using acetone and isopropanol to ensure its thorough cleanliness. The sample is blow dried with N_2 and coated with a photoresist layer to protect the patterned layers for the next step.

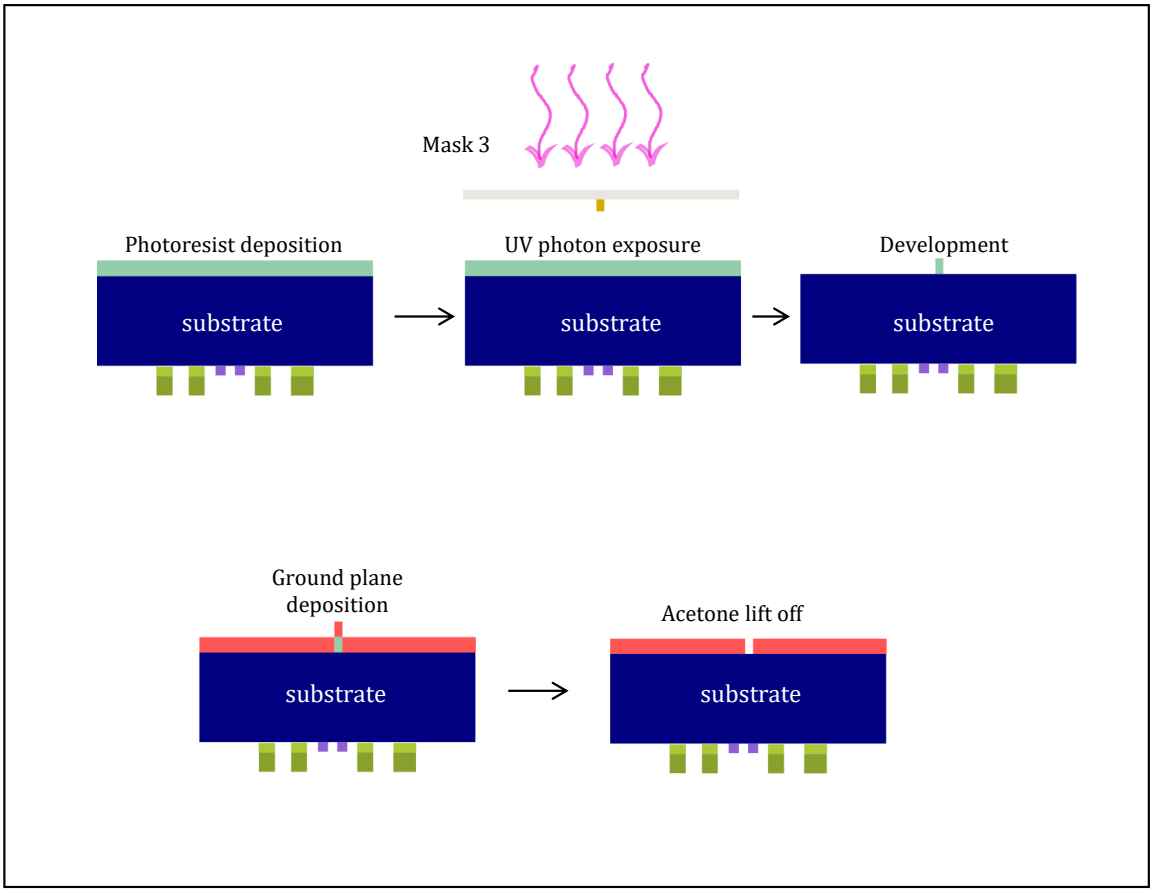

Figure 5.3: Fabrication steps followed for the ground plane with slot shape with the third mask. The lithography is in this case realised on the back of the substrate.

5.4 Third Lithography Step: slot antenna in the ground plane (OMKID only)

After completing the patterning process on one side of the substrate, we proceed by flipping the substrate to utilize the back side for the subsequent step. In this process, the image reversal resist is once again employed facilitating the alignment between the slot shape in the back and the mm wave line in front of the substrate. We show in Fig.5.3 the steps followed in the next sections.

Step 7: Patterning When fabricating the OMKID device, we create a slot-shaped pattern (antenna) on the ground plane. To accomplish this, a layer of AZ5214E photoresist is coated onto the substrate, and Step 4 of the fabrication process is performed using the third mask.

Step 8: Deposition A 200 nm aluminum (Al) with a rate of 2 nm/s, followed by a 200 nm thick gold (Au) layer with a rate of 0.5 nm/s was deposited on the patterned resist for the ground plane. The gold layer is used for better thermalization of the sample.

Step 9: Lift off To ensure the protection of the first and second layers on the front side of the substrate, a resist that is soluble in acetone is used. Therefore, before initiating the lift-off process for this particular step, it is necessary to safeguard the back side of the sample. This can be achieved by placing the sample on a concave-shaped glass beaker cover and positioning it on top of the beaker used for the acetone bath. The dimensions of the cover are critical to ensuring proper floating of the back side of the sample. The sample is left immersed in the acetone bath for 20 minutes. As a result of this process, a star-shaped slot is formed in the center of the ground plane, facing the mm wave line feed on the front.

HYPKID device As there are no structures on the ground plane for HYPKID, the last step was depositing the ground plane which was followed by Step 8.

5.5 Etching Processes

In this section, we will describe various etching methods that we have developed in this thesis. Etching solutions, which are carefully formulated dilutions, are utilized for the purpose of selectively removing metal layers. We often used the Al etch solution and HF for our device.

Al Etch The etching process for Aluminum involves the use of a specific etchant, known as Aluminum etch. It is composed of 1-5% HNO_3 (for Al oxidation), 65-75% H_3PO_4 (to dissolve the Al_2O_3), 5-10% CH_3COOH (for wetting and buffering) and H_2O dilution to define and limit the etch rate. The etching process is an exothermic process and constant agitation is needed to reduce the under etching of the mask and ensure uniformity.

Ti Etch: HF solution In standard process, we use 0.05-0.1% hydrofluoric acid in DI water for the Ti layer removal. This process leaves the residues of titanium fluoride. The sample must be cleaned in DI water multiple times after exposure to the etching solution.

Standard Clean 1 solution Due to a temporary unavailability of hydrofluoric acid (HF), we employed this solution to etch the titanium layer in a limited number of samples. The composition of the solution employed was as follows: 4 parts water (H_2O), 1 part of 27% ammonium hydroxide (NH_4OH), 1 part of 30% hydrogen peroxide (H_2O_2). We observed that the 10 nm layer of Ti had been completely removed within 45 seconds.

5.6 Packaging: sample holder

The aluminum sample holder is specifically designed to host a 2 inch wafer and was developed in an improvised manner. It has an octagonal shape in order to hold the sample without the need

for dicing. The holder is either equipped with a back short or an eccosorb layer to allow different options for optical measurement. The sample is equally pressed on the sample holder by the custom gold plated copper beryllium (CuBe) tweezers. Thus, the back side of the substrate is grounded and thermalized with the sample holder. There are two SMA connectors to connect the 50 Ω microstrip launchers with the readout circuits. The SMA connectors are soldered to the copper microstrip launcher. Al wire bond (17 μm wire) are made in between the launcher on the chip and the copper feed line using a micro bonding machine. The aluminum sample holder ensures magnetic shielding. The aluminum wire bondings and soldering are linked between the SMA connector and the readout lines of the sample. In front of the LEKIDs and filters, the backshort/eccosorb is mounted at a calibrated distance. When the reflecting backshort is used, it is placed at a distance of around 800 μm to the sample. This corresponds to roughly $\lambda/4$ for 90 GHz radiation.
Fig.5.5 and 5.6 show the OMKID and HYPKID devices installed in the specific sample holders.

Lens and Horn The conical horn with a diameter 8 mm and flare angle 29.86° is machined on the aluminum sample holder. The shape is continued for 7.8 mm and followed by a cylindrical waveguide of diameter 2.5 mm and length 4.7 mm. The waveguide is terminated on the ground plane of the sample by the slot antenna. The sample holder was designed to place the antenna at the termination of the circular waveguide.

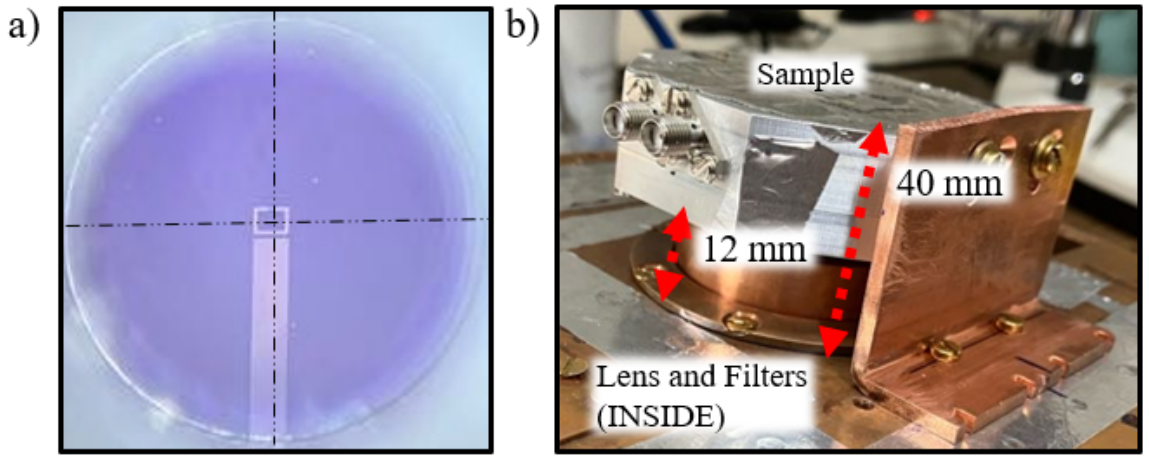

Figure 5.4: Placement of the HYPKID sample, (a) optical image during the centring of the absorber with respect to the waveguide for the HYPKID device, (b) the device kept on the focal plane of the lens with a post.

5.7 Installation in the cryostat

Fig. 5.4 shows how the HYPKID sample was centred manually and kept on the cryostat focal plane using a metal post. For the image lens, the 5.9 cm^{-1} and 3.7 cm^{-1} low pass filters were fastened with metal washers to keep them in place, in front of the device. The set-up with lens, filter and device was placed on the NIKA cryostat at the 100 mK stage, ready to cool-down.

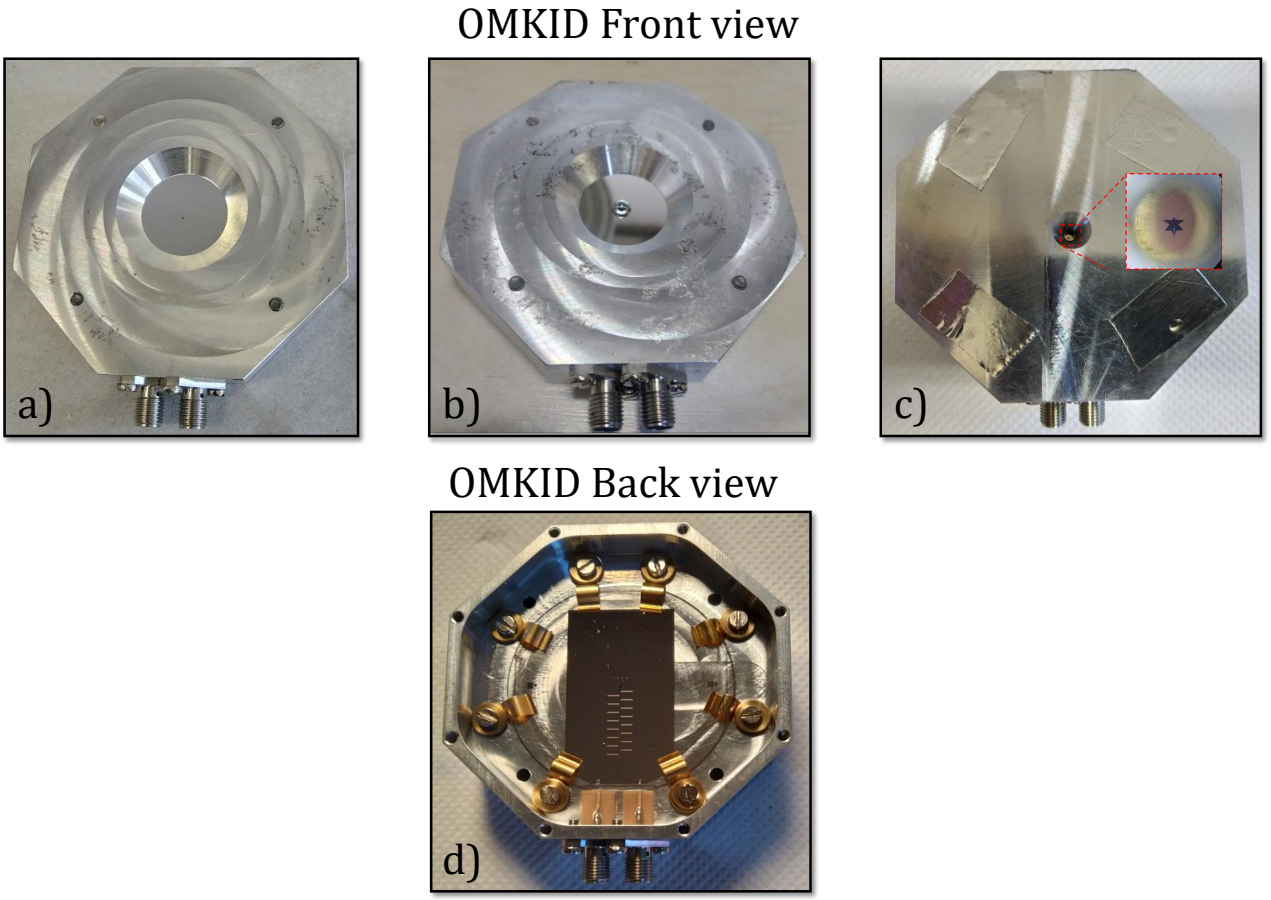

Figure 5.5: Final OMKID device on sapphire installed in the sample holder and ready for testing. Front view of the slot antenna (a). Illumination through Si hemispherical lens (b) and through horn and waveguide (c). In the inset, the slot shape at the centre of the waveguide is shown. Thanks to the sapphire's transparency, we can observe the part of microstrip which is on the other side of the substrate. View of the device from the detectors side of the substrate (d).

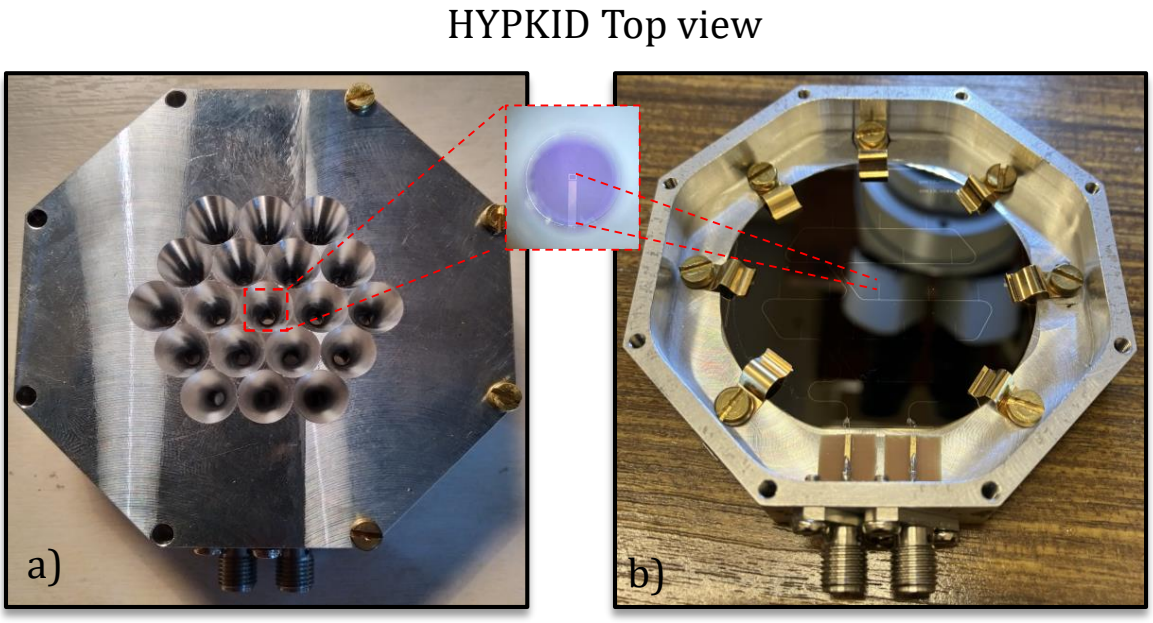

Figure 5.6: Final HYPKID device (on silicon) ready for testing. Both the images are top view of the HYPKID device. The detectors are shown with horn (a) and without horn (b). *Inset.* The visible section of a channel within the waveguide.

Chapter 6

Measurement Set-up

6.1 NIKA0 camera

We have used a customized cryogenic camera called NIKA0 to conduct tests on our device at cryogenic temperatures. NIKA0 is a dilution refrigerator with a base temperature of approximately 60 mK. The system is composed of multiple temperature stages, thermally isolated from each other. Each stage is equipped with a screen positioned along the optical axis. The screens are covered by alumina foil to minimize radiative heat transfer and have an optical aperture on which we mount filters that effectively block unwanted radiation. The temperature screens and the corresponding filters of NIKA0 are (Fig. 6.1):

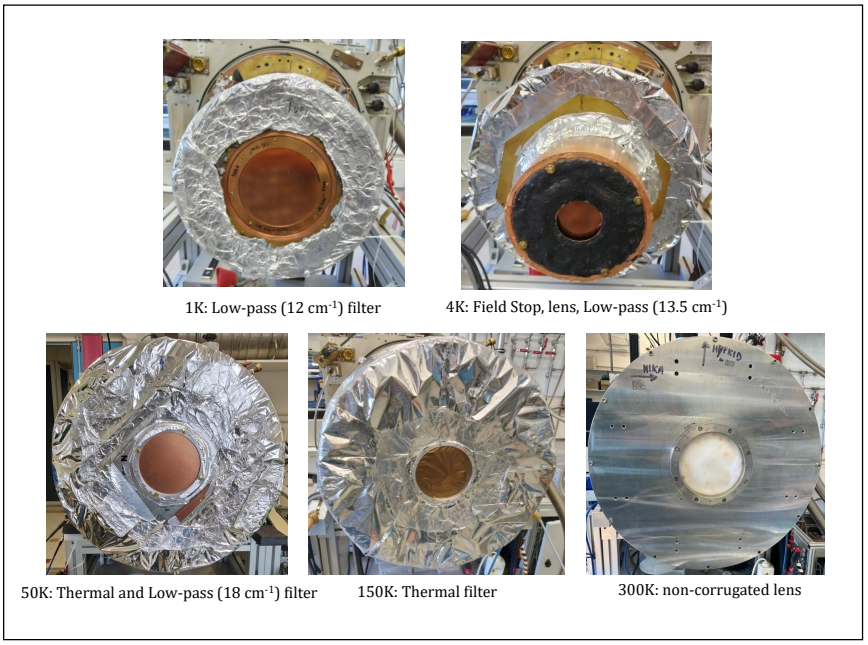

Figure 6.1: Optical elements on the different screens in the NIKA0 camera.

- At 300 K, we have the main cryostat body.
- At 150 K, there is an infrared (IR) block filter.

- At 50 K, we have an IR block and an 18 cm^{-1} low pass edge (LPE) filter. This filter allows frequencies below 540 GHz while blocking higher frequencies.
- At 4 K, we have a 13.5 cm^{-1} transition filter, allowing frequencies below 400 GHz.
- At 1 K, there is a 12 cm^{-1} low pass edge (LPE) filter, which corresponds to 360 GHz.
- At 100 mK, the coldest stage, we mount the final band-defining filters as shown in Fig. 6.2. Additionally, in this stage, we have the flexibility to adjust the pupils of different radii and select the input power of the optical signal.

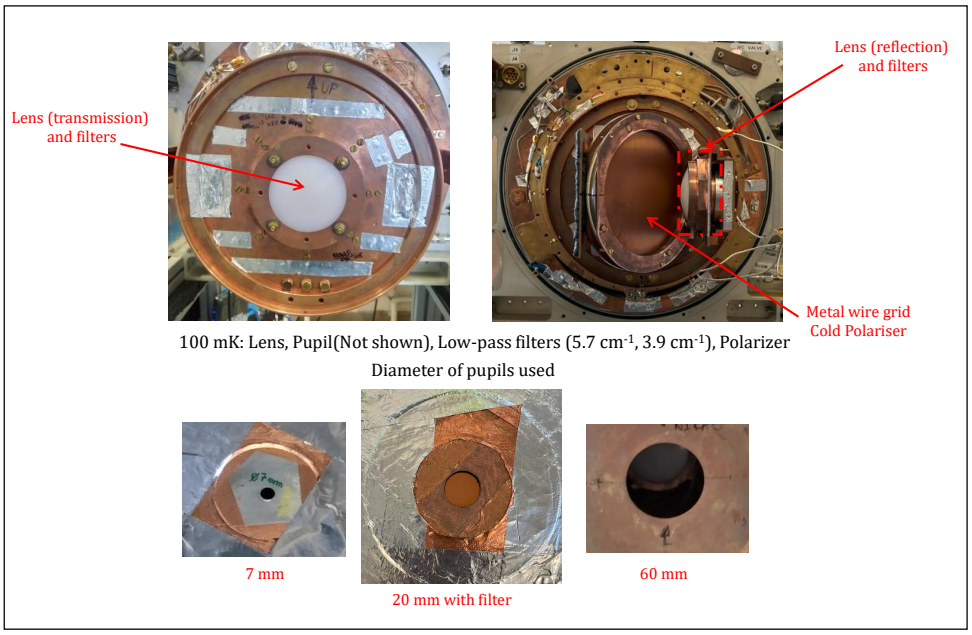

Figure 6.2: Optical elements in the NIKA0 cryostat at 100 mK.

The remaining optics consist of three non-corrugated high density polyethylene (HDPE) lenses, mounted on the 300 K, 4 K, and 100 mK stages. An additional lens can be added to the 300 K window to adjust the focal plane position for lab measurements, as the original set of lenses is designed to couple NIKA0 to the IRAM 30 m telescope of Pico Veleta. This corrective lens is used for capturing images of the planet in front of the sky simulator. However, when using the mm-wave source for data acquisition, we do not utilize the corrective lenses. In this case, the optical system has a pupil located 10 cm outside the cryostat, where we mount our mm wave source. This setup allows the point-like source to illuminate the entire focal plane Finally, to suppress the Earth's magnetic field, a μ-metal shielding is added to the 4 K stage, and a superconducting lead (Pb) shield is added to the 1 K stage.

At 100 mK, two low-pass filters with cut-off frequencies of 5.7 cm^{-1} and 3.9 cm^{-1} are positioned along with the lens. These filters block the radiation above 180 GHz and 120 GHz, respectively. The cold lens directs the incoming signal onto the detector and the image. As shown in the upper right of Fig. 6.2, we can use a polariser to project a linearly polarised signal on the device. Fig. 6.3 (a) shows the optical path of NIKA0 cryostat for a mm wave source kept at 10 cm from the 300 K window, at the room temperature pupil.

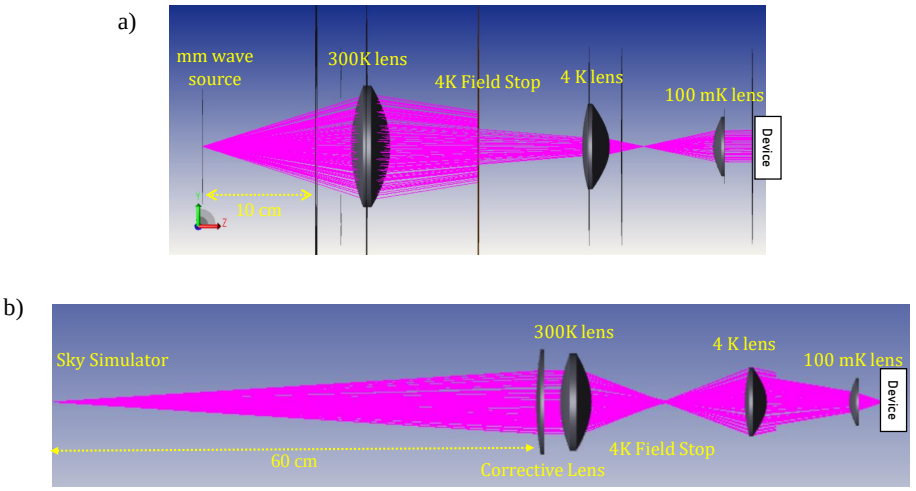

Figure 6.3: (a) The optical path of the NIKA camera with the mm-wave source placed on the 300 K pupil. (b) The optical path of the camera with the sky simulator on the image focal plane.

6.2 RF lines

The NIKA0 cryostat is equipped with two complete RF readout units to which we can connect the links to SMA feedthroughs inside the cryostat, allowing testing for two device measurements simultaneously. A DC block is connected to the stainless steel cabling, which is used for connections at 300 K. The output of the DC block is then connected to a -10 dB attenuator at 4 K and another -10 dB attenuator at 100 mK to suppress the effects of the 300 K Johnson noise. The stainless steel cabling itself contributes roughly an additional -5 dB of attenuation. Below 4 K, NbTi superconducting cables are adopted. The attenuated signal is then sent to the device, which is at a temperature of 100 mK. The signal is passed through another DC block. The output signal from the device is amplified using a low noise amplifier (LNA), which adds

+30 dB of gain. The additional attenuation due to the stainless steel cable is approximately -5 dB. Therefore, the total attenuation from the VNA to the device is about -65 dB. Inside the cryostat, the net power is roughly zero.

6.3 Vector Network Analyser (VNA)

The frequency sweep of the resonances is carried out using a Vector Network Analyser (VNA). The VNA consists of a source for generating a RF signal that is fed to the device in test (DUT) and a receiver to measure the signal transmitted past the DUT (or reflected from it). By comparing the generated and received signals, a VNA can easily measure all the circuit parameters such as the transmitted signal between the generator and the receiver, S_{21} both in phase and amplitude. Our primary use of the VNA is to carry out frequency sweep to measure S_{21} and thus be able to deduce the resonance positions and quality factors.

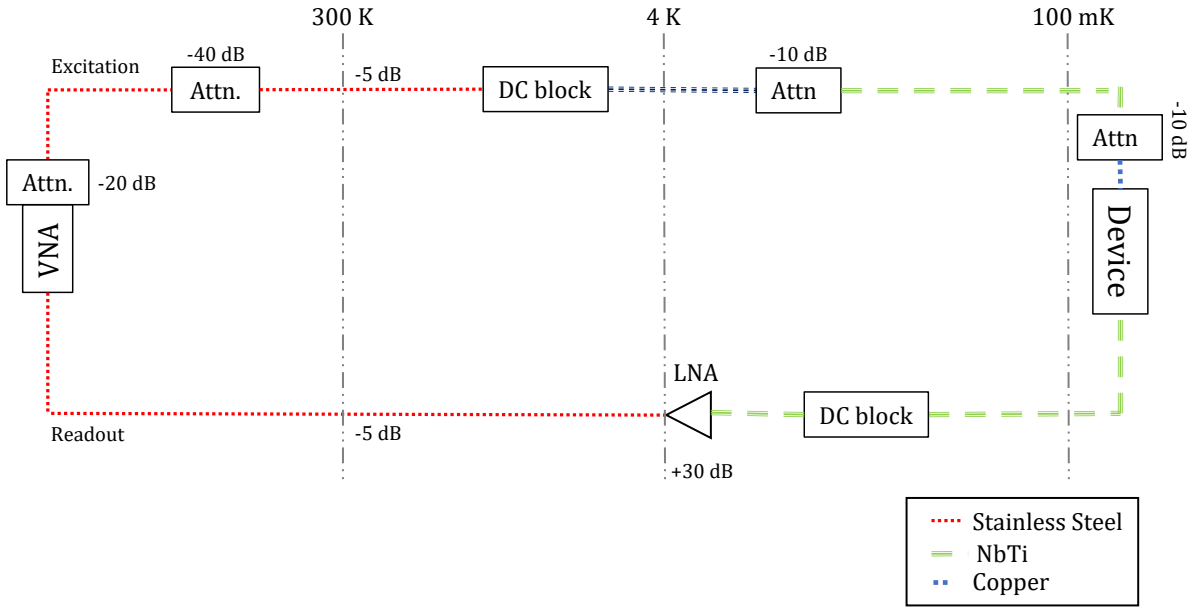

Figure 6.4: The RF lines connected with VNA

In our specific setup shown in Fig. 6.4, we require a low excitation power for our DUT, typically in the order of -100 dBm. To achieve this, the VNA signal (whose amplitude can be varied between -70 dBm to 20 dBm) is first attenuated by a fixed attenuator of -40 dB. This attenuated signal serves as the excitation for the device.
The two ports of the device are micro-bonded with Al wire to the LEKID readout line (TiAl). The designed impedance of the line is 50Ω to match the cables and the LNA. The detectors used in this thesis have resonance frequencies ranging from 1 to 2 GHz. The resonance peaks

of the LEKIDs are measured at a readout power of approximately -100 dBm.
To evaluate the optical response, we place either a metal plate or $Eccosorb^{TM}$ plate, in front of the optical lens of the cryostat. In one configuration, the metallic side of the plate faces the inside of the cryostat. In this setup, the plate acts as a mirror and the detectors see the reflection of the cryostat coldest stages. Therefore, the mirror acts as a cold blackbody for the detectors and we refer this configuration as "0 K". The real blackbody equivalent temperature is obviously well above 0 K, especially because of the nonzero emissivity of the plate and all the components present in the optical path. In the other configuration, the eccosorb plate acts as a blackbody emitter at approximately 300 K (referred to as "300 K"). The eccosorb not being ideally emissive, the effective temperature is lower than 300 K.
The frequency shift, δf for each resonance between these two background temperature conditions reflects the optical response of the detectors. Fig. 8.1 shows the readout frequency sweep for one configuration of the HYPKID on a silicon device. At T_{300K}, the device experiences more pair-breaking radiation, leading to an increase in surface impedance due to the higher density of quasiparticles. As a result, the resonance frequencies at T_{300K} are shifted to lower frequencies. On the top of that, they are broader compared to that observed under a lower optical load, due to the losses associated with the excess quasiparticles.

6.4 Electronics

For our real-time observations and analysis of resonators, we adopt the NIKEL, an electronics and data acquisition system customized for this purpose. A comprehensive description of the system can be found in the article by Bourrion et al (2012) [Bourrion et al., 2012]. By using a frequency multiplexing technique, this electronics enables the simultaneous monitoring of 400 pixels over a 500 MHz bandwidth on a single transmission line.
The NIKEL electronic board consists of a central FPGA (Field Programmable Gate Array) that receives the data flow from a 12-bit analog to digital converter at a rate of 1 Gigabits per second. The electronic board generates the excitation frequency comb in the form of in-phase (I) and quadrature (Q) components with a phase difference of 90°. To reach frequencies in the range between 1 and 5 GHz, the frequency comb is up-converted using a mixer and a synthesizer acting as a local oscillator (LO). A variable attenuator limits the power of the signal after IQ-mixing to prevent saturation of the LEKIDs. At the output of the LEKID array, the signal is amplified by a cold low-noise amplifier at the 4 K stage and further amplified at room temperature. The modified frequency comb, obtained by down-converting with an IQ mixer and the synthesizer signal (LO), is brought back to the original FPGA bandwidth (0-500 MHz). Finally, the power of this signal is adjusted to match the dynamic range of the subsequent ADC using another controllable attenuator.

a)

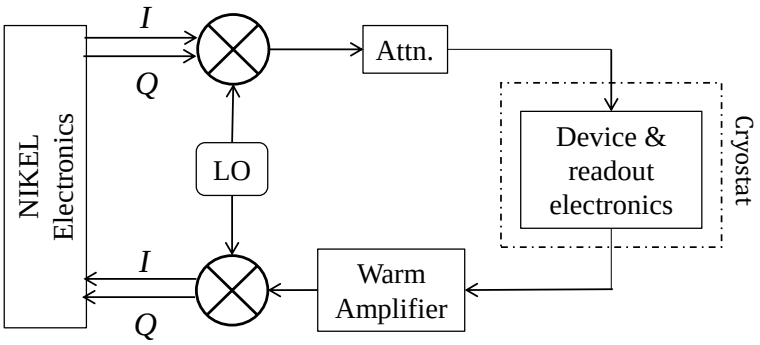

b)

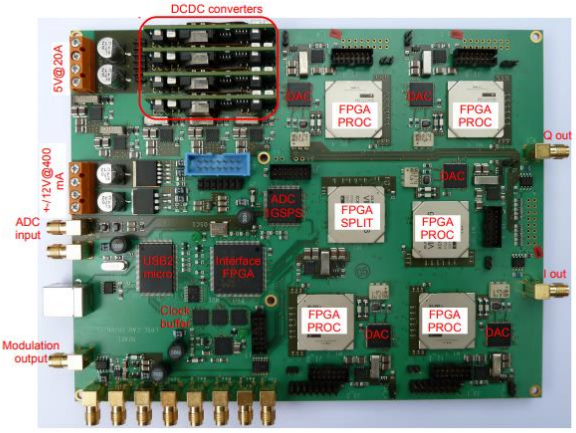

Figure 6.5: Electronics set-up: (a) The schematic of the whole readout/excitation chain. (b) A picture of the NIKEL board, taken from Bourrion et al. (2012)

The digital signal, acquired by the ADC is down converted in the complex domain into I and Q components for each tone. The amplitude (A) and the phase (ϕ) of the transmitted tone signal are given by,

$$A = \sqrt{I^2 + Q^2} \qquad \phi = tan^{-1}\frac{Q}{I} \tag{6.1}$$

The response of every pixel of the array is in this way measured simultaneously and broadcasted to the control computer where it is acquired by a custom software as shown in Fig. 6.6.

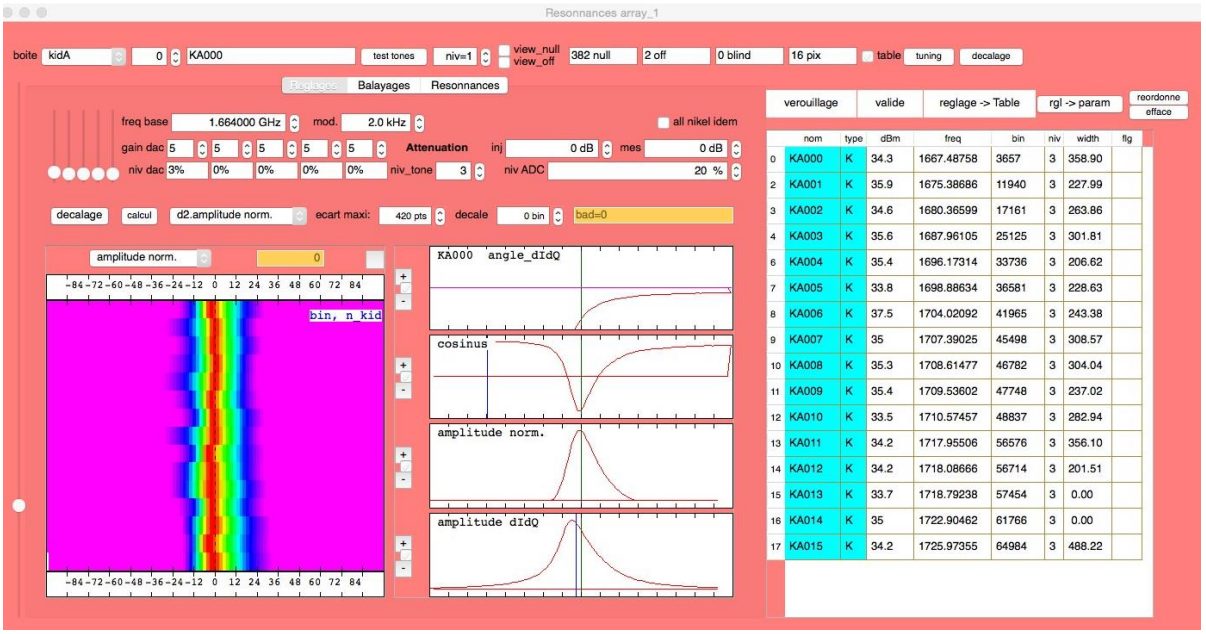

Figure 6.6: A typical capture of acquisition software for OM-D4 device

6.5 Martin Puplett Interferometer (MPI)

The broadband (0-500 GHz) low resolution spectral characterization was performed using a custom Martin-Puplett Interferometer.
When two monochromatic waves combine, depending on their relative phase they can either reinforce each other (constructive interference) or cancel each other out (destructive interference). In the interferometer, the waves are generated from a single source and travel along different paths before recombining. A moving mirror introduces variations in the optical path, leading to interference based on frequency and arm length differences. This interference pattern, captured in the interferogram, can be Fourier transformed to deduce the power as a function of frequency. The Martin-Puplett Interferometer [Martin and Puplett, 1970], a special type of Fourier Transform interferometer, uses wire grids instead of total power splitters. The output signal produced by the Martin-Puplett Interferometer system is linearly polarized, i.e., the electric field vector has a well-defined direction. The optics of our custom-made MPI system [Durand, 2007] is shown in a top view diagram in Fig. 6.7 (a). The image is taken from the article [Maleeva et al., 2018]. The radiation source consists of two combined beams emitted by blackbodies at temperatures of 77 K (liquid Nitrogen) and 300 K. The rotating polariser P1 combines and polarizes the beam, which is then divided by two partial beams by the beam splitter, BS. The wire grids of the beam splitter BS are oriented at 45° to the normal of the drawing so that the polarization component perpendicular to the grid is transmitted and the component parallel to

the grid is reflected. The two metal roof mirrors, one of which is movable, reflect the two components back to the beam splitter with a 90° rotation of polarization. When the roof mirrors are equally spaced from the beam splitter, the input and output beams of the beam splitter have the same polarization. After passing through polariser P2, only one orthogonal polarization is transmitted to the cryostat. The intensity of the signal for two sources T_1 (300 K) and T_2 (77 K) from MPI is given by:

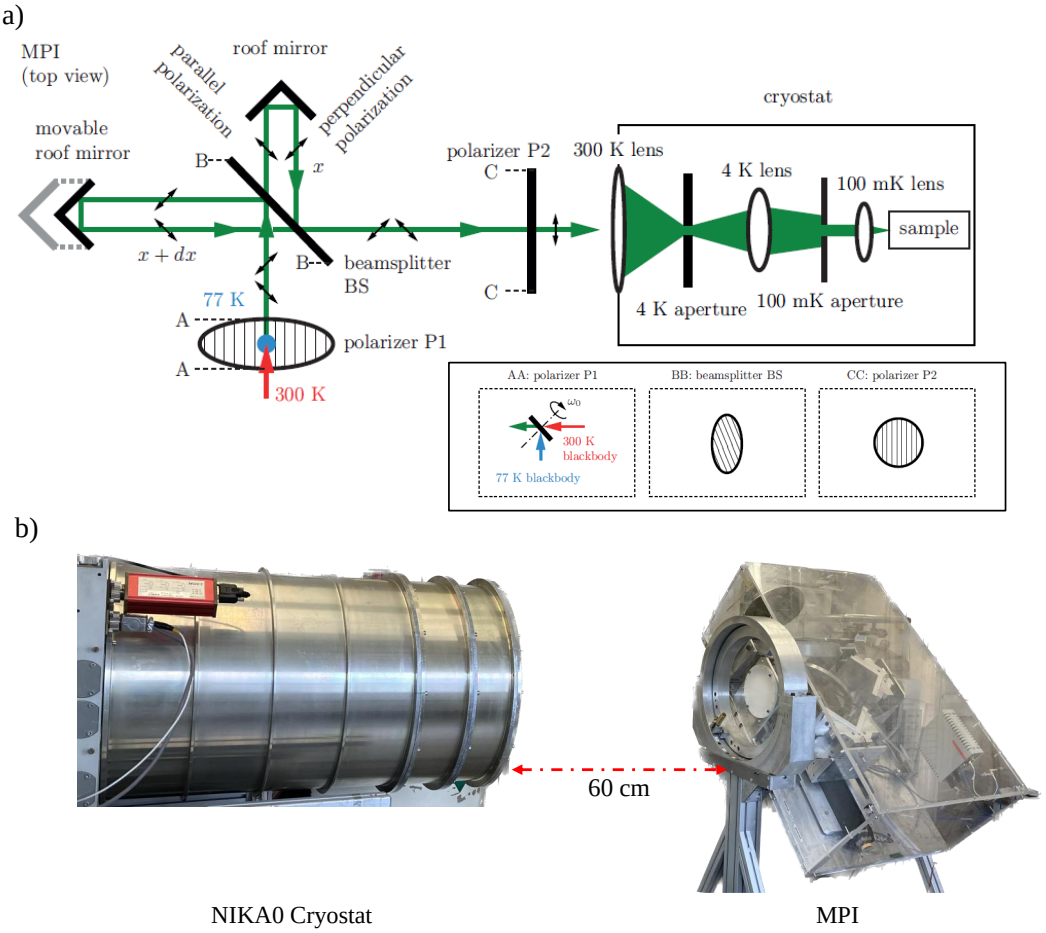

Figure 6.7: Martin Puplett Interferometer: (a) Optical diagram of the Martin Puplett Interferometer with the polarizing elements in the inset. The image is taken from the supplementary information of the article. [Maleeva et al., 2018](b) The MPI instrument positioned at the focal plane of NIKA0 cryostat and titled by 45° to select the needed polarization direction.

$$I_f(\delta x) = \frac{1}{4}(P_f(T_1) + P_f(T_2)) + \frac{1}{4}(P_f(T_1) - P_f(T_2))\cos(2\pi\omega_p t)\cos\left(2\pi f\frac{2\Delta d}{c}\right) \tag{6.2}$$

$I_f(\delta x)$ is the amount of output power for the incident monochromatic frequency f where the moving mirror is at a distance δx from the zero position, $P_f(T)$ is the power of a blackbody at temperature T and ω_p is the modulation frequency of the interferogram provided by the rotating polariser P1. The first term is constant and the second term directly affects the interferogram. The observed interferogram for all the frequencies is given by the integral,

$$I(\delta x) = \int_{f_{min}}^{f_{max}} I_f(\delta x) A_f \, df \tag{6.3}$$

where A_f is the absorption of the LEKIDs as a function of frequency. We convert the intensity from the optical domain to the frequency domain by applying a Fourier transform.
The resolution of the measured spectrum is determined by the maximum displacement of the moving arm, denoted as x, while the maximum detectable frequency is related to the minimum control step of the moving mirror. The displacement between the zero position of the mirror is -110 mm to 24mm. The resolution is given by the formula,

$$\delta f = \frac{c}{2x_{max}} = \frac{3 \times 10^8 \text{ m/s}}{2 \times 110 \times 10^{-3} \text{ m}} = 1.36 \text{ GHz} \tag{6.4}$$

The minimum displacement of the mirror is $\Delta x = 25\mu$m, which provides the maximum frequency $(f_{\max}) = 3000$ GHz which is deduced by the formula,

$$\Delta x = \frac{c}{4 f_{\max}} \tag{6.5}$$

The whole MPI can be tilted at different angles (-45°, -30°,-15° 0°, 15°30°, 45°) to select the desired polarization. In Fig. 6.7 (b), the MPI is positioned at 60 cm in front of the NIKA0 cryostat and tilted at -45° to provide a specific polarization.
The interferogram can be observed between 0 GHz to 3000 GHz. However, our interest lies below 120 GHz. Most of the measurements are carried out with both 3.9 cm^{-1} ($f_{\text{cut off}} = 120$ GHz) and 5.7 cm^{-1} ($f_c = 180$ GHz) low-pass filters.

6.6 mm Wave source

The millimetre wave source are commercially available modules, used to provide millimetre wave signals. Fig. 6.8(a) shows a schematic diagram of a module connected in the circuit. Usually, the module is connected directly to the RF output of a signal generator in order to extend the microwave outputs to frequencies in the millimetre wave range. The signal generator acts as a driver for an amplifier-multiplier chain. In this chain, the input signal is first multiplied and then amplified by an active monolithic microwave integrated circuit (MMIC) module. The amplified signal is then used internally to drive a separate passive multiplier, typically a doubler or a tripler. The frequency and power of the output are regulated by the synthesized signal source.
The mm wave source has an active component, millimetre wave source module, from *Keysight Technologies* connected with a passive component, horn antenna from *Fairview Microwave.*

Fig. 6.8 (c) shows the output power of the source module provided by the manufacturer, over the range of 75 GHz to 110 GHz. Thus, the maximum output power in linear scale is in between 6 mW to 10 mW.

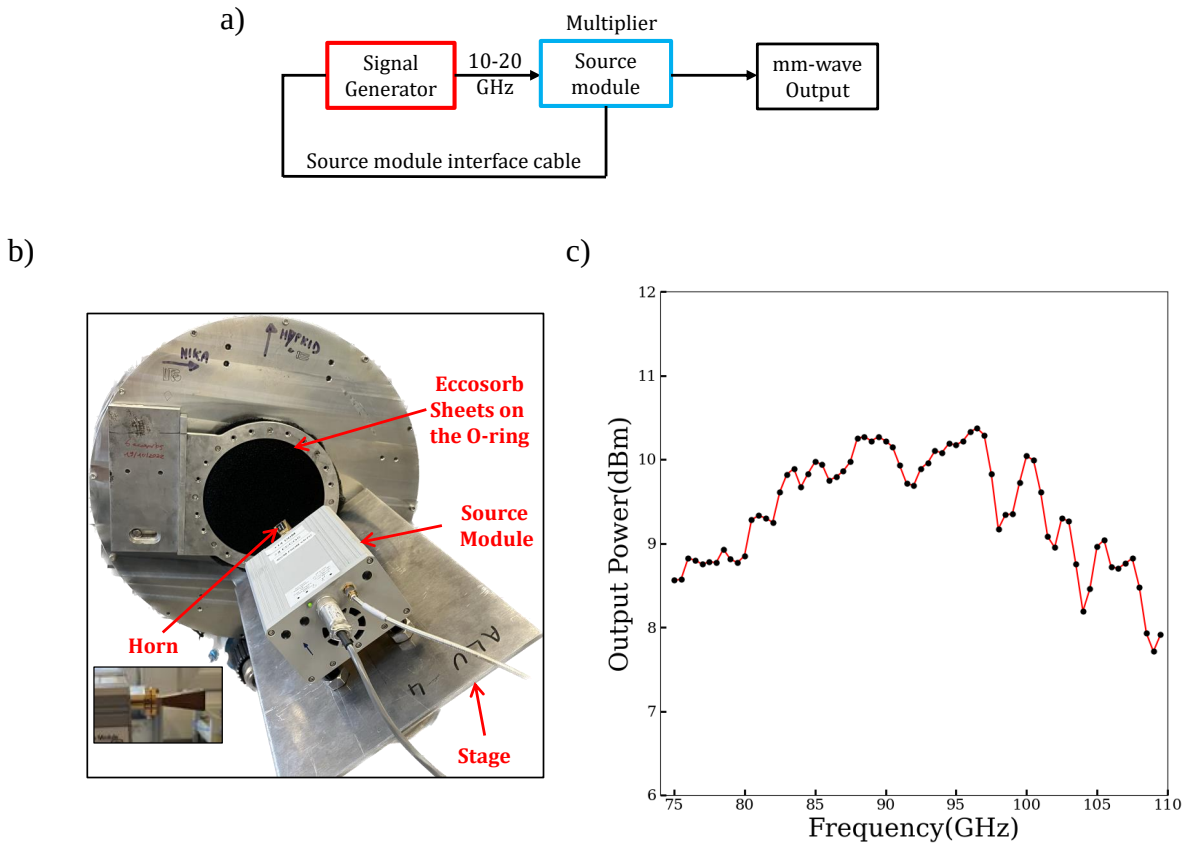

Figure 6.8: mm wave source: (a) The schematic of the electronic chain for the mm wave source, (b) The polarised mm wave source, mounted at 45° is installed in front of the cryostat with the attenuator eccosorb sheets on the window. (c) The graph shows the output power of the mm wave source module over the frequency range (from *Keysight* data sheet). It varies in between 8 dBm to 10 dBm over 75 GHz to 10 GHz.

The horn antenna is a commercial WR10 waveguide type horn antenna with nominal gain of 20 dBi across the operating frequency range. In the normalized far field view of the electric field pattern in gain, the main lobe is around 18° FWHM with gain of -5 dBi. In the measurement settings, the antenna is placed at the warm pupil of the NIKA camera, i.e., around 10 cm from the 300 K lens. The eccosorbs are sandwiched in a metal O ring and placed on the 300 K lens as shown in Fig. 6.8(b). Each eccosorb provides a 25-fold attenuation, so we estimate $25^6 \approx 10^8$ attenuation of the incoming signal from the mm wave source. The loop time was 100 ms

corresponding to 10 Hz, lower than the readout frequency (46 Hz).

6.7 Sky Simulator

a)

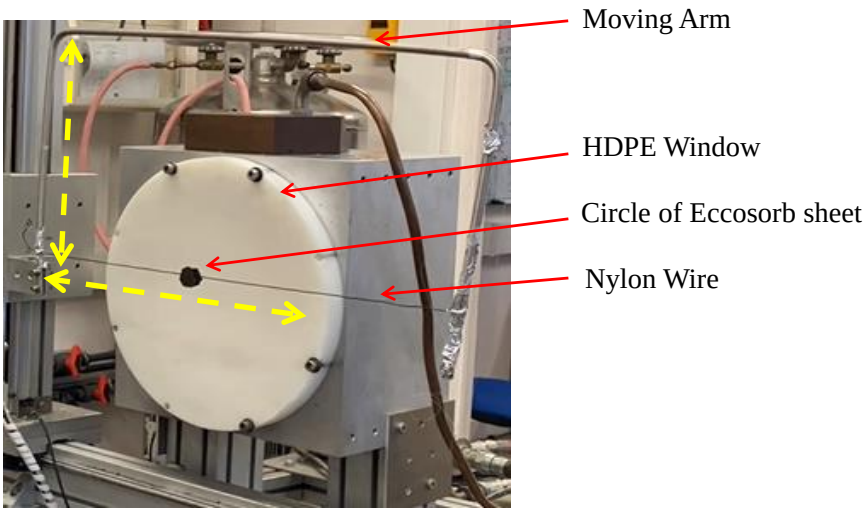

b)

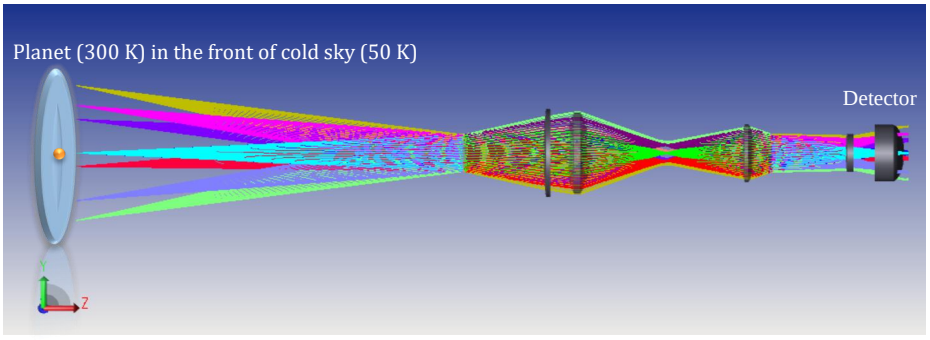

Figure 6.9: Sky Simulator: (a) The custom sky simulator with different components used in our measurement is shown. (b) A typical ZEMAX simulation of the optical diagram of a sky simulator for a 'Planet' placed in front of the background 'sky'.

The sky-simulator is a tool that can efficiently mimic the cold background of the Sky, due to the emissivity (ϵ) of the atmosphere at mm-waves. For a site such as Pico-Veleta, the emissivity is typically in the range of 10 to 30 %, so the sky can be approximated by a blackbody with a temperature in the range of (0.1-0.3)×300 K, i.e., roughly 30 K to 100 K. Our sky simulator [Monfardini et al., 2011] is based on a large disk, covered with a layer of black material ($\epsilon \sim 1$ at mm wave) with dimensions similar to the focal plane of the IRAM telescope in Pico Veleta, is cooled to 50 K down by a cryogenic-free system. The temperature of the

sky simulator can be varied with a heating resistor connected to the blackbody disk. This allows us to estimate the device response with different background temperatures. In order to reproduce an astronomical source, a smaller diameter ball with a high-emissivity , the 'Planet' was positioned in front of the window of the sky simulator. The source can move across the XY plane. The detectors located in front of the sky simulator detect this transition of a 300 K source in front of the cold back ground.
The sky simulator used for our measurement is shown in Fig. 6.9(a). For our measurements, the Planet was a circular eccosorb sheet with a 4 cm^2 area held by a Teflon wire at room temperature. It is placed at the focal plane of the NIKA camera, precisely 60 cm away from the cryostat window.
Fig. 6.9(b) shows the optical path diagram of the sky simulator for different beams of ray. The rays at the centre and extreme corners end up on the different positions on the detector.

Chapter 7

Measurements on OMKID Device

In this chapter, we describe the performance of the OMKID devices that we have designed and fabricated. Their performances via the OMKID approach have been evolved through successive measurements towards the concept of HYPKID.

7.1 List of OMKID devices

As explained in Chapter 3, the OMKID device has sixteen channels directly coupled to the mm wave line. Each of these channels comprises a c-shaped filter coupled with a LEKID resonator. The LEKIDs are then capacitively coupled to the readout line. These sixteen channels are referred to as "Spectral channels". Four other LEKIDs, directly coupled to the readout line, but not to the mm-wave line, are called "Dark channels". This design is referred to as 'M1'. The OMKID device was fabricated on silicon and sapphire of various thicknesses in five different batches using the same design, M1. A sixth batch uses a modified version of the original design. In this M2 design, three LEKIDs were directly coupled to the mm-wave line without any filter shapes. Each device underwent multiple cryostat cool-downs for testing purposes. Throughout the process, we encountered and resolved various technical issues to establish a standardized method for device characterization. Table 7.1 details the different fabrication batches.

Device No.	Dielectric (Thickness in μm)	Design	Fabrication procedure	No. of LEKIDs Identified/Designed
OM-D1	HR-Si (170)	M1	F1	16/20
OM-D2	Sapphire (170)	M1	F1	17/20
OM-D3	Sapphire (110)	M1	F1	19/20
OM-D4	Sapphire (165)	M1	F2	20/20
OM-D5	Sapphire (108)	M1	F1	20/20
OM-D6	Sapphire (110)	M2	F1	23/23

Table 7.1: List of devices made with OMKID design on high-resistivity silicon (HR-Si) and sapphire dielectrics. M1 is the basic design of our prototype OMKID device. M2 is the modified OMKID design with three LEKIDs directly coupled with the mm wave line (no filter). F1 is the fabrication method where HF was used for the etching of Ti layer whereas F2 is the fabrication procedure where a standard cleaning solution (H_2O_2+NH_4OH+H_20) was used. Out of 20 (23 for the batch six) designed LEKIDs, the identified LEKIDs during VNA frequency sweep measurement are given. The missing LEKIDs can be attributed to fabrication issues.

In the initial stages of the fabrication process, high resistivity silicon (HR-Si) was chosen as the substrate material. However, during the fabrication of the OM-D1 batch, we realized that it was

difficult to achieve a proper alignment of the slot antenna with respect to the mm wave line. In order to overcome this issue, the dielectric material was changed from HR-Si to c-cut sapphire, which is transparent. This makes the optical alignment between the different layers possible. We will present below the measurements, carried out on the OMKID devices on sapphire of different thicknesses.

7.1.1 VNA measurements

A standard VNA measurement serves several purposes:

- identifying the operational LEKIDs.
- assessing the quality factors of the LEKIDs.
- determining the frequency shift resulting from changes in the optical load.

A typical frequency sweep with VNA of the device OM-D6 is shown in Fig. 7.1.

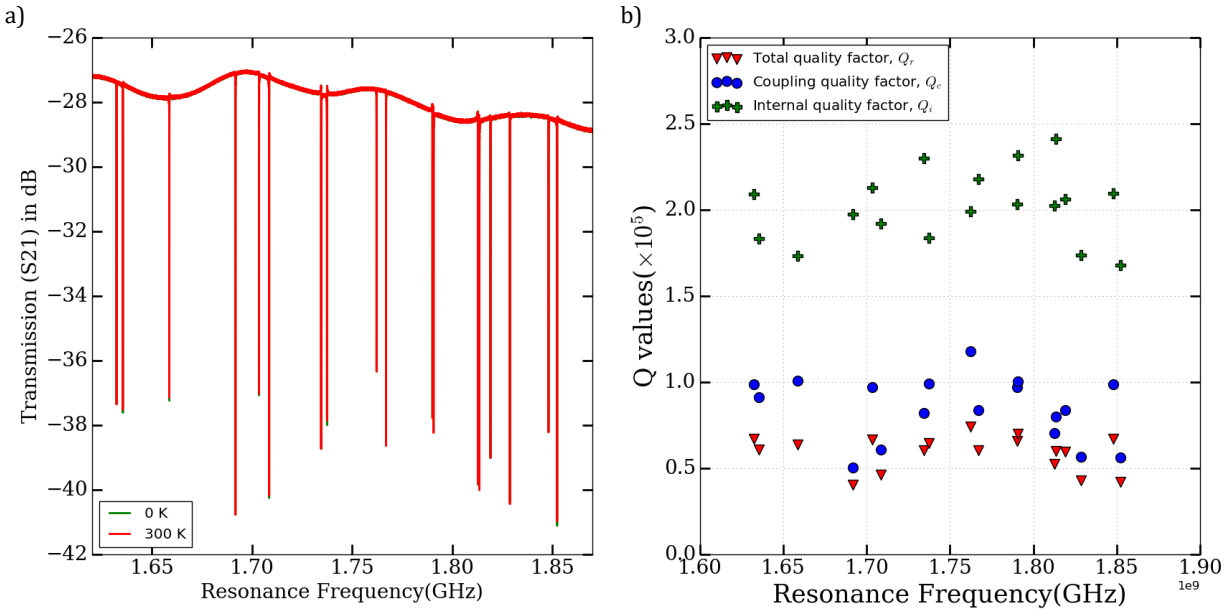

Figure 7.1: Response of LEKIDs for an excitation tone power of -100 dBm per LEKID: a) S21 Transmission frequency sweep for the OMKID device, OM-D6 where the resonances were taken for two optical loads "0 K" and "300 K". The device was illuminated through the horn, waveguide and slot antenna. The resonance frequencies do not vary in between the variation of the optical loads. b) The fitted quality factors for all the LEKIDs.

As a first step, all the devices were tested with VNA. We have chosen to present only the most relevant data for devices OM-D2 and OM-D3. In Table. 7.2, we show the parameters extracted from frequency sweeps at -95 dBm tone readout power for the device OM-D2 in different optical configurations.

Run No.	Illumination Through	Backshort/ Eccosorb	Cold Pupil Diameter (mm)	Averaged Q values at -95 dBm ($\times 10^4$)		$\delta f_{(0K-300K)}$ (kHz)
				Q_i	Q_c	
1	Slot antenna	Backshort	60	9.9 ± 0.7	6.5 ± 0.8	11.7 ± 0.1
2		Eccosorb		8.2 ± 1.5	6.4 ± 0.8	6.7 ± 0.1
3	Slot antenna with a small opening	Eccosorb		7.6 ± 0.1	9.2 ± 0.5	47.4 ± 0.2
4	Si lens on slot antenna	Backshort		9.9 ± 0.4	9.3 ± 0.1	12.0 ± 0.1
5	Direct	N.A		3.0 ± 0.1	6.9 ± 0.8	211.1 ± 1.5
6	Direct without slot	N.A	7	6.6 ± 0.1	5.9 ± 0.3	1.8 ± 0.1

Table 7.2: Channels' properties in average over sixteen spectral channels of the OMKID device OM-D2.

The optical configuration and the device set up was varied for the different runs. For most of the runs, the pupil used to illuminate the array was 60 mm in diameter. It was reduced to 7 mm during Run 6 for photo-metric cross-check. Runs 1-6 are described for OM-D2 (thickness of 170 μm). To illustrate different optical couplings, we use Table. 7.3 which displays the parameters extracted from the VNA measurements on OM-D3 (thickness of 110 μm).
We detail here the configurations for each run:

- In Run 1, the device was illuminated through the slot antenna. Behind the OMKID device, a reference backshort was used. As a side effect of this, the signal reflected from the backshort can be detected directly by the LEKIDs together with the genuine signal guided through the microstrip.

- In Run 2, the device was illuminated through the slot with an absorbing layer(eccosorb plate) replacing the backshort, to avoid the spurious signal induced by the backshort.

- In Run 3, we illuminate the device through a small area above the slot to further mitigate the unwanted reflection and to reduce the flux of the incoming signal, with again an eccosorb facing the detectors (as in Run 2).

- During Runs 4 and 8, the optical signal was focused on the slot by a hemispherical silicon lens of diameter 4 mm.

- In Runs 5 and 7, the detectors' side was directly illuminated. The signal is sent directly to the wafer side containing the c-shaped filters and the LEKIDs. (and is not sensed via the slot antenna)

- In Run 6, the slot was removed and the ground plane was changed by adding 100 nm Gold on the top of existing 200 nm Aluminum layer to check the thermalization of the device. The illumination is direct as in Run 5 and 7. Furthermore, in order to do a photometric cross-section, the pupil used to illuminate the array was reduced to a diameter of 7 mm, instead of standard 60 mm used for OM-D2 and 20 mm for OM-D3.
- In Run 9, the signal was concentrated on the slot-antenna by putting a conical horn followed by a circular waveguide.

Run No.	Illumination Through	Cold Pupil Diameter (mm)	Averaged Q values at -100 dBm ($\times 10^4$)		δ f$_{(0K-300K)}$ (kHz)
			Q_i	Q_c	
7	Direct	20	7.2 ± 0.1	8.9 ± 0.5	19.7 ± 0.1
8	Si lens on slot antenna	20	8.1 ± 0.1	8.4± 0.6	4.6 ± 0.1
9	Horn waveguide on the slot antenna	20	16.7 ± 0.3	10.6± 0.5	0.2 ± 0.1

Table 7.3: The quality factors for the OMKID device OM-D3 for different optical settings.

The frequency shift (δf) represents the signal. Therefore, ideally, a larger shift is preferable. However, it is important to emphasize that the observed δf is the combined effect of the signal resulting from the channel (i.e., the filtered response) and the undesired signal caused by stray light. Only through spectroscopy measurements, we can distinguish between these two contributions and thus identify the configuration that is performing better.

7.2 OMKID with star slot antenna

In this section, we discuss low resolution (MPI) spectroscopic measurements realized on OM-D2 during Run 1. The principle of MPI measurement is described in Section 6.5. The OMKID is illuminated through the slot with a backshort in front of the LEKIDs. For the backshort, we used a metal plate at 800 μm distance from the detectors. Fig. 7.2 corresponds to the spectrum for InPol polarization, i.e. the input polarization is aligned with the mm wave line. The spectrum exhibits several distinct features:

- The lower frequency cut-off corresponds to the superconducting gap frequency of 2Δ = 69 GHz. This value is determined using the BCS formula $2\Delta = 3.52 k_B T_c$, where k_B represents the Boltzmann constant and T_c is the transition temperature, approximately 1 K for TiAl.
- The upper frequency cut-off corresponds to the low-pass filter, specifically 3.9 cm^{-1} $\sim$ 118 GHz.
- The sharp peaks that are visible in the spectral responses and that are at different frequencies for different channels can be associated to the c-shaped filters. The presence of these peaks demonstrates the selective frequency response of the filters.

A characteristic observed across all detectors, including spectral and dark channels, is the presence of a common continuum mode with Fabry-Perot (FP) interferences. The interference phenomenon arises when an optical cavity with a specific length, denoted as L, is present. This length directly determines the frequency spacing between consecutive interference peaks, as given by the formula $\delta\nu = \frac{c}{2nL}$, where c represents the speed of light in a vacuum, and n indicates the refractive index of the medium. The FP signature is a spectral oscillation at frequency, $\delta\nu \sim 10.6$ GHz. While the presence of the cavity mode is not a significant concern, mitigating this effect can potentially enhance the quality of the spectral signals.

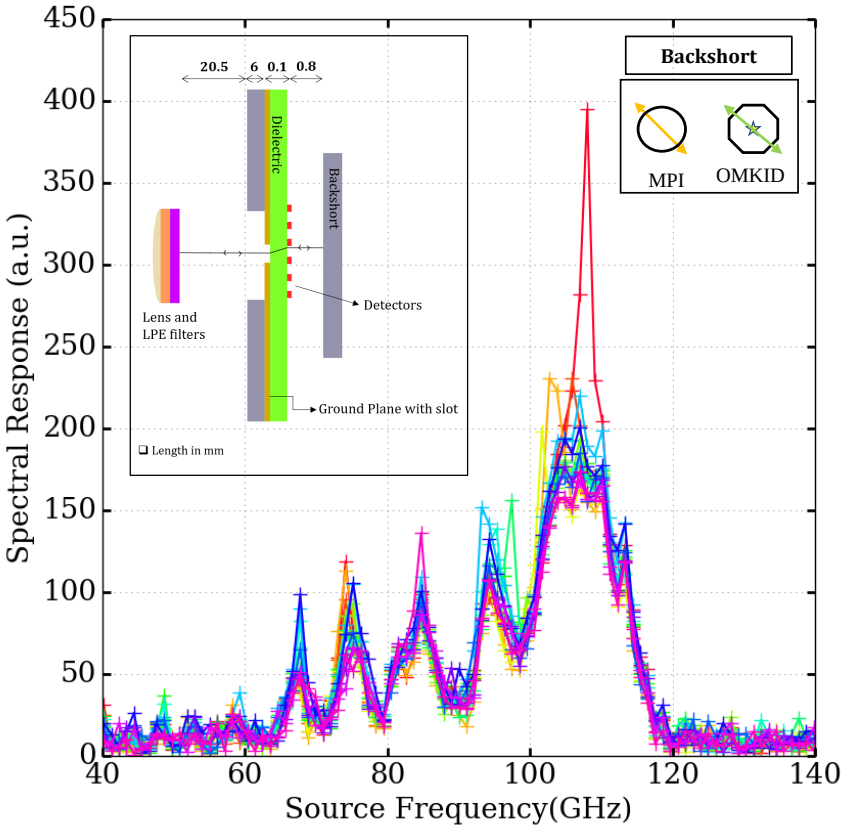

Figure 7.2: MPI data for OM-D2 (Run 1). Each color refers to each channel in the spectrometer. Inset Image: The device is illuminated through the slot antenna, with a metal backshort (in grey), which is kept in front of the detectors which are shown in red. The incoming signal passes through the lens and filter setup where two low-pass filters (shown in orange and violet) are in front of the slot shape in the ground plane (golden).

In the case of OM-D3 device, a sapphire component with a thickness of $t = 110$ μm and dielectric constant approximately equal to $\varepsilon_{r_s} = 10$ was used. The distance between the low pass filters-

lens setup in front of the optics slot measures approximately $L = 26.5$ mm. By using the formula and considering the refractive index of vacuum as $n_v = 1$, and for sapphire $n_s = \sqrt{\varepsilon_{r_s}} = 3.16$, we can calculate the total cavity path required to generate the Fabry-Perot behaviour. Taken into account the different refractive indices and thicknesses, $\Delta\nu = \frac{c}{2(n_v L + n_s t)} = 5.6$ GHz. In order to minimize the interference fringes, a replacement was made by introducing an eccosorb layer onto the metal plate instead of using a backshort. As observed in the Tab. 7.2, as a result there has been a decrease in the frequency shift from ~ 12 kHz to 6 kHz between Run 1 and 2 for OM-D2. We hypothesize that the extra variation between open ("300K") and close ("0K") windows primarily arose from the presence of stray light back reflected multiple times in the cavity. Thus, by substituting the backshort with an absorbing layer, the stray signal is minimized.
In conclusion, we have evidence of the spectrally filtered signal(peaks) and we have identified a first, major contribution to the stray light (continuum).

7.3 OMKID with Si lens

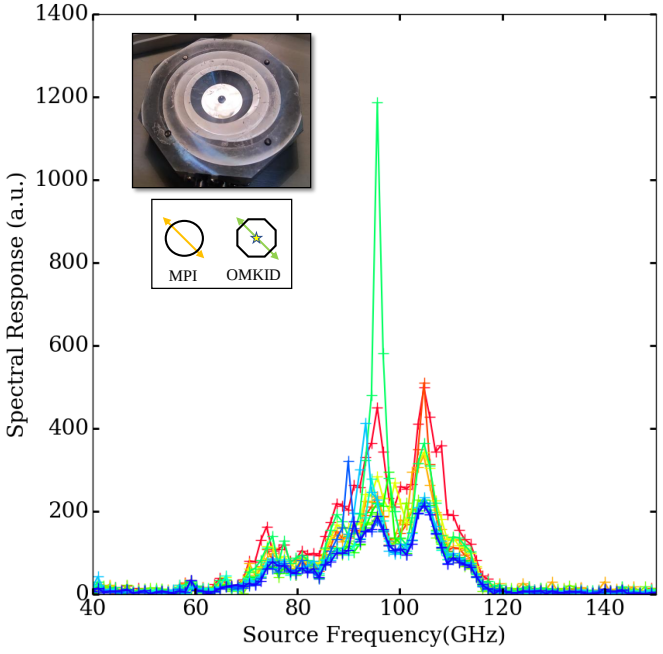

Figure 7.3: MPI data with the configuration of polarization InPol with the mm wave line for OM-D3. Inset: Si lens of 4 mm diameter on the top of the slot shape in the middle of the ground plane. Different colours refer to different channels.

In order to enhance the optical coupling between the slot and the incoming signal, one possible approach explored was the use of a silicon hemispherical lens placed on the slot in a way that

the center of the star-shape of the slot is lined up at the center of the hemisphere. To secure the lens in place, we applied GE varnish, an adhesive commonly used for establishing thermal contacts at low temperatures. In Fig. 7.3 for OM-D3, overall the sharp peaks associated with the c-shaped filter became more prominent compared to the common mode. The substrate was sapphire, with a thickness of 170 μm. It is important to note that this data was acquired with a reflection backshort, which accounts for the presence of peaks in the common mode. From this MPI measurement, we concluded that the Si lens indeed enhances the optical coupling. However, the Si lens option is impractical for upscaling. For this reason, we have investigated another solution described in the next section.

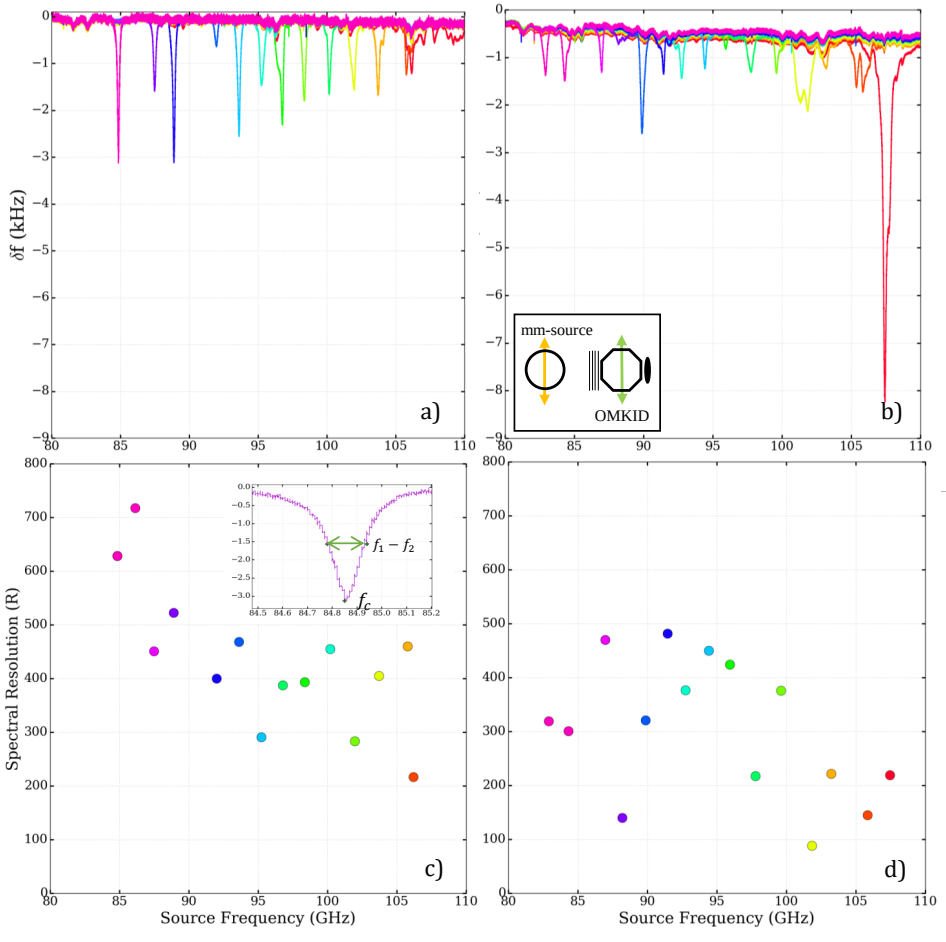

Figure 7.4: Spectral responses of the OMKID device with mm wave source in InPol Polarization. Four sheet of eccosorbs were used to attenuate the source signal. The device measured are the OM-D5 (108 μm) with M1 OMKID design in the left panel (a) and OM-D6(110 μm) with M2 design in the right panel (b). The spectral resolution(R = $\frac{f_c}{f_1 - f_2}$) decreases from 650 to 200 with increasing frequency for OM-D5. One of the channel response is zoomed in inset image (c). R is dispersed in the range 50-500 (d). Different colours refer to different channels.

7.4 OMKID with horn and slot antenna

As an alternative approach to the Si lens, a conical horn-circular waveguide feed was used to improve the coupling between the incoming signal and the slot. This feed enabled the effective transmission of the incoming signal to the slot. The resolution of the Interferogram is 1.2 GHz, thus it is worse than 0.5 GHz, the simulated resolution of the filters. As one of the key parameter of interest is the spectral resolution of the filters, we need a source with sufficient resolution. We therefore switched to the mm-wave source, which has a resolving power better than the designed resolution of the filters. The mm-wave source set-up is described in Section 6.6. The output power of the source was 8 mW, which is an excessive input power for the detectors. Multiple measurements were taken with varying number of eccosorbs in front of the source in order to modulate the signal sent into the cryostat. In the final configuration, the mm wave source is placed 10 cm away from the cryostat window and a series of eccosorbs sheets are fixed to the 300 K window which provides an input signal in the $\sim p$W range.
The signal observed with horn fed slot antenna is shown in Fig. 7.4. This measurement was taken in InPol condition with four sheets of eccosorb in front of the detectors in the device. On the optics system, the source signal was attenuated with four eccosorb sheets on the cryostat window.
The resolution is calculated by the ratio of the central frequency (f_c) and the full width half maxima (FWHM) (f_2 - f_1) for each spectral dip. As from Fig. 7.4 (c) and (d), the spectral resolution of most of the spectral channels lies between 200 and 500. Fourteen (a) and fifteen (b) out of sixteen channels are identified. The attenuator, eccosorb sheet thickness is not uniform over its mounting ring. This might be an explanation for the variation of intensity in Fig. 7.4(b).
For both devices, the higher response corresponds to the lowest side-length of the filter shape, which is also the closest to the open end of the mm wave line.
The high frequency signal may arise from the introduction of the normal sheet resistance of the aluminum filters near the superconducting gap frequency (106 GHz) or the power calibration of the source or the radiation because of the open end of the mm wave line.
The c-shaped filters are designed to respond to a single polarization. We have discussed the device behaviour in InPol polarization. At the similar optical configuration, with CrossPol, we found that the spectral channels are inactive in agreement with our simulations.

7.5 Thermalization improvement

One issue that was identified during the OMKID runs involved the thermalization of the substrate. When the optical power was varied in front of the cryostat window, a frequency shift as displayed in Fig. 7.5(a) showed a slow time constant of approximately 3 seconds in the response of the OMKID device. After considering the thermal heat capacity of sapphire and its thermal conductivity, it was determined that the observed phenomenon can be attributed to the wafer thermalization. The thermalization time, τ can be calculated as $\tau = c_p/\kappa$, where c_p is the specific heat and κ is the conductivity of thermal link. Thus, enhancing the thermal conductivity helps in reducing the time required for the system to recover the thermal equilibrium.

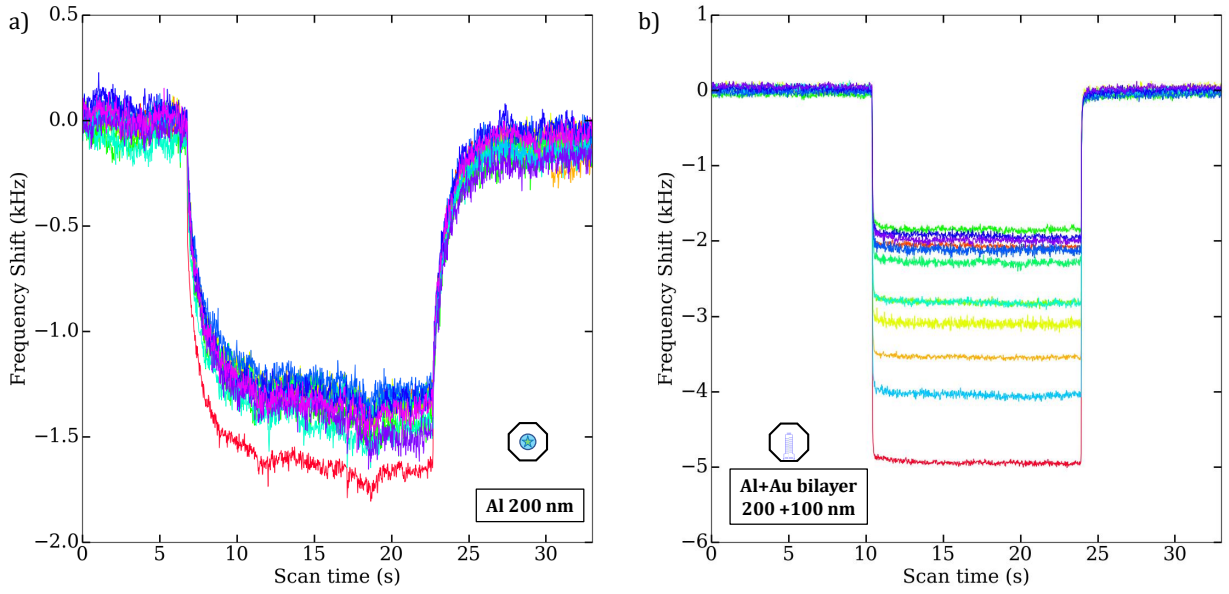

Figure 7.5: Step variation of the input signal to inspect the effect of thermalization for OM-D3. (a) The device was illuminated through the Si lens and the slot antenna. The ground plane was 200 nm of aluminum. (b) Direct illumination of OM-D3 (Run-6). The ground plane was, 100 nm gold on the top of 200 nm aluminum layer. Different colours refer to different channels.

For this reason, we decided to add a gold layer above the aluminum (superconducting) layer. As shown in Fig. 7.5, the addition of the gold layer effectively solved the problem. At low temperatures, the heat capacity in metals exhibits α T dependence, while phonon scattering (dielectrics and superconductors) follows a α T^3 dependence. In the superconducting state, the heat transfer is hindered by the unavailability of free electrons. Incorporating a gold layer solves this problem since gold is a normal metal.
The measurements shown in Fig. 7.5 panels (a) and (b) were done using the same optical configuration in the cryostat and on the same device, OM-D3. In panel (a), the device was illuminated through the Si lens. The data in panel (b) was taken after the Al ground plane with the slot antenna has been etched away and replaced with a 100 nm gold and 200 nm Aluminum bilayer. In this case, the device was front illuminated. The reduction in the response time proves that the validity of this solution. Nonetheless, bilayers made in this way turned out to age, visible with a change in colour of the ground plane. With time, an intermetallic alloy formed at the interface between the 100 nm gold and 200 nm aluminum layers, causing this variation in the colour of the deposited film. The interface properties changed due to the diffusion of Au atoms in the aluminum at the interface causing the formation of different inter metallics like AlAu, Al_2Au_5, $AlAu_2$ or $AlAu_4$. Most of these inter metallics behave differently from the pure metal counterpart. Thus, the behaviour of the alloy differed from that of pure aluminum,

potentially impacting its superconducting properties. A good quality superconducting ground plane is crucial to ensure the lossless behaviour of the microstrip mm wave line and the quality factors of the LEKIDs and the filters. To prevent this effect, we decided to add a 50 nm titanium layer between the 200 nm gold and the 200 nm aluminum layers, as titanium, a diffusion barrier prevents the formation of such intermetallic compounds. This effectively reduces the diffusion and has become our standard recipe.

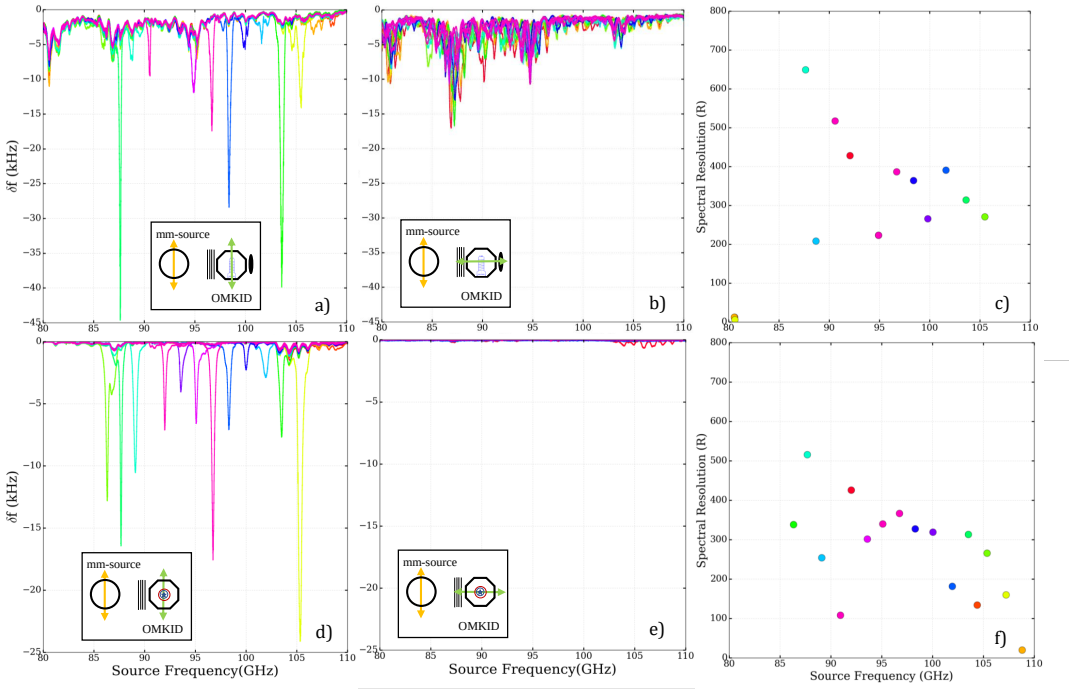

Figure 7.6: The spectral response and the resolution of OM-D4, illuminated with the mm wave source through four eccosorbs attenuated layers. The top panels of (a), (b) and (c) show the results for direct illumination. The panel below i.e., (d) , (e), (f) shows the measurement when the incoming signal is guided through horn and waveguide transition on the slot antenna. Different colours refer to different channels.

7.6 Fabrication optimization: F2 process

We discuss the OM-D4 device measurement separately, as instead of the typical HF solution for TiAl layer etching, we used an alternative solution (discussed in Section 5.5). This device marked the initial implementation of the horn-waveguide feed for the slot antenna. Out of the sixteen channels, twelve exhibited spectral responses when illuminated by the mm wave source. The measurements were conducted with a pupil diameter of 20 mm and four eccosorb absorbers as attenuator. A comprehensive description of this device was published in Chowdhury, Usasi, et al. "A horn-coupled millimetre-wave on-chip spectrometer based on lumped-element kinetic

inductance detectors." *Astronomy and Astrophysics* (2023). [Chowdhury, U. et al., 2023].
Fig. 7.6 shows the response of the device, obtained with the attenuated mm wave signal (a) when illuminated directly on the detectors and (b) when illuminated through horn, waveguide and slot antenna. The behaviour of the common (continuum) signal is varied in both cases. In OMKID design, all the channels have the same coupling distance between the mm wave line and the filter, as well as between the readout channel and the capacitors. Therefore, the spectral channels should be arranged in the same order as the LEKIDs. However, in this particular batch, the spectral channels were not sorted according to the readout frequency, unlike in previous (and subsequent)batches. We suspect that there may have been an impact on the surface due to the fabrication process. Nevertheless, the spectral response for each channel was higher compared to the channels fabricated using the "M1" method. These issues require further investigation.

7.7 OMKID with Front (Direct) Illumination

To check the behaviour of the LEKIDs, the OMKID device was illuminated directly from the LEKIDs side. The frequency shift ($\delta f_{0K-300K}$) changed from 6 kHz to 211 kHz for OM-D2 as shown in Table. 7.2 (Run 5). Signals were observed only in InPol polarization, i.e., when the MPI polarization is aligned with the filters.

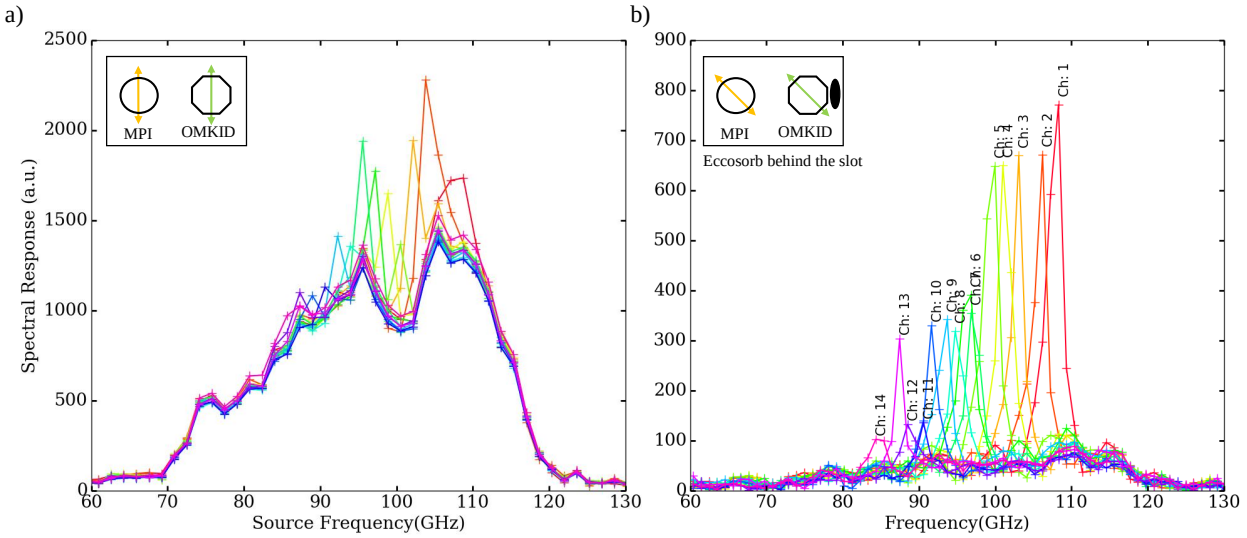

Figure 7.7: MPI data for the direct illumination on the OMKID device, both in InPol polarization with mm wave line for OM-D2 (a) and OM-D3 (b) sample. An eccosorb layer was placed at the backside of the LEKIDs to reduce the stray light. Different colours refer to different channels.

Fig. 7.7 shows the MPI low resolution (1.2 GHz) for direct illumination on OMKID devices fabricated on 170 μm thick sapphire (OM-D2) and 110 μm thick sapphire (OM-D3). The polarization was aligned with the filters and, thus, perpendicular to the LEKIDs. The visible peaks indicate that direct illumination of the c-shaped filters could be a promising option to consider instead of excitation through the mm wave line. The difference between panels (a) and (b) is that we switched from a backshort to an absorbing layer facing the LEKIDs. Interestingly, the continuum response decreased when the eccosorb was used. We also found that using a thinner dielectric helped reduce this continuum background. The observed amplification in response as the frequency increases can be attributed to the blackbody source power. According to Planck's law, in this range the energy emitted by a blackbody per unit time is directly proportional to the square of the frequency.

Chapter 8

Measurements on HYPKID Device

The OMKID device's response to direct illumination, as depicted in Fig. 7.7, indicated a potential pathway for a new device called "HYPKID". When directly illuminated, the c-shaped filters serve as frequency selective absorbers. A primary concern regarding the signal was the reduction of the common background signal across all channels when directly illuminated. This background mostly arises from the unwanted frequency shift due to the direct absorption of the incoming signal in the LEKIDs. To address this, the HYPKID device incorporates a circular waveguide coupled with a conical horn positioned in front of each filter, increasing the coupling of the incoming signal to the filters. In this configuration, only a portion of the LEKIDs is exposed to the incoming signal. Moreover, as the LEKIDs and absorbers are sensitive to opposite polarizations, the signal coupled with the filters in InPol polarization proves to be more effective than that of the LEKIDs in the same polarization.

Device Description The device fabrication involved using both sapphire (HY-Al1 and HY-Al2) and silicon substrates (HY-Si). The HY-Si device has been extensively tested under different conditions. In the initial HYPKID device on sapphire, two problems were observed. First, the spectral resolution was higher than the values predicted by simulations. Secondly, there was a gradual shift in the resonance frequency of the LEKIDs over time. Our hypothesis is that the first issue arose due to the vacuum gap between the feed horn and the superconducting absorber. To reduce this gap, a 275 μm thick silicon wafer with a metal layer called the "spacer" was introduced between the sample holder and the device. The metal layer consists of an Aluminum (200 nm)-Titanium(50 nm)- Gold (200 nm) trilayer. As for the second issue, which may have been caused by a non-standard fabrication process (referred to as the "F2" process described earlier), a new test device was fabricated with the same HYPKID layout on silicon wafers of 100 μm and 160 μm thickness, using a standard fabrication procedure ("F3").

8.1 Resonant Frequencies

Fig. 8.1 shows a typical VNA measurement for one of the HYPKID devices in typical '0 K' and '300 K' configurations discussed in Section. 6.3.

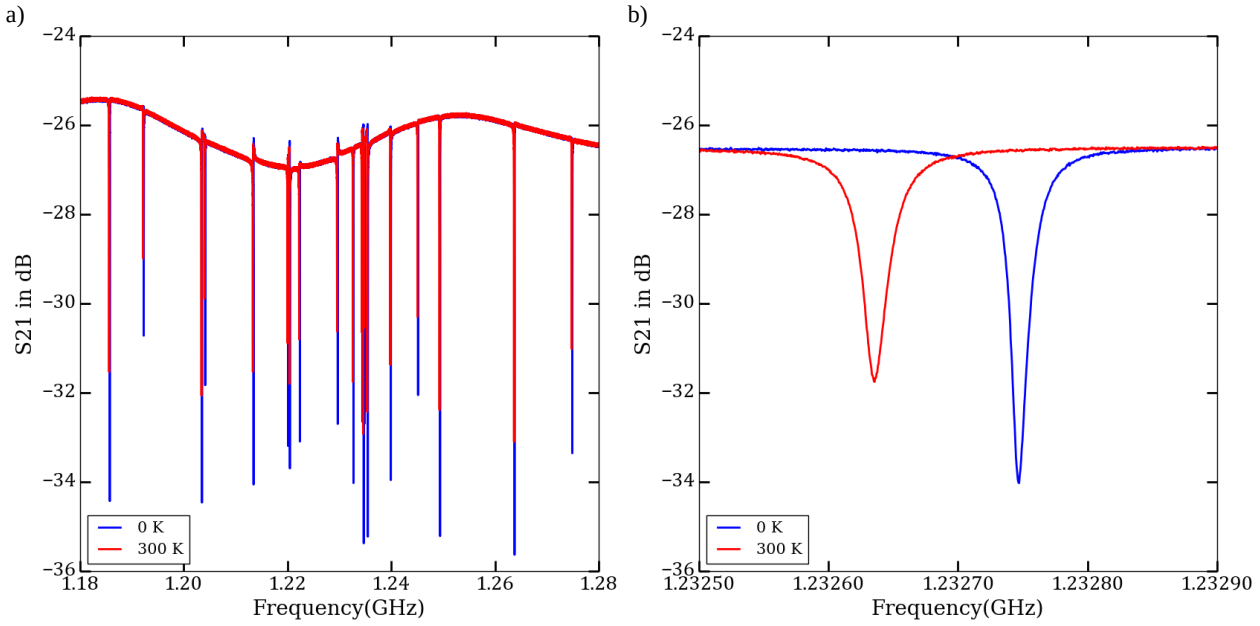

Figure 8.1: The frequency sweep: (a) of the LEKIDs with the metal plate in two configurations, T_{0K} (blue) and T_{300K} (red) on the cryostat optical window. (b) One of the resonances has been zoomed.

Table 8.1 and 8.2 show the frequency shifts and the quality factors for different optical configurations for HYPKID on sapphire and silicon estimated from the VNA measurements. The illumination of the channels occurred through distinct pupils. By incorporating a 45° wire-grid polariser in front of the device, the input signal is filtered, producing a polarised signal hitting the HYPKID focal plane. As seen in the Tables, all the LEKIDs were responding and exhibiting internal quality factors, Q_i and coupling quality factors, Q_c of similar order.

Table 8.1: Frequency sweep data for HYPKID on 110 μm thick Sapphire (HY-Al1 and HY-Al2).

Run No.	Device	Cold Pupil Diameter (mm)	Polariser	Spacer (275 μm)	Averaged Q values at -100 dBm ($\times 10^4$)		$\delta f_{(0K-300K)}$ (kHz)
					Q_i	Q_c	
1	HY-Al1	20	No	No	7.6 ± 0.1	9.3 ± 0.5	5.2 ± 0.2
2	HY-Al1	20	Yes	No	6.4 ± 0.2	8.5± 0.6	3.0 ± 0.0
3	HY-Al1	60	Yes	No	6.3 ± 0.2	9.1 ± 0.5	14.7 ± 0.3
4	HY-Al2	60	No	Yes	6.1 ± 0.3	10.2 ± 0.3	79.5 ± 1.2

Table 8.2: Frequency sweep data for HYPKID on 170 μm thick Silicon for device HY-Si1.

Run No.	Cold Pupil Diameter (mm)	Filter (cm^{-1})	Polariser	Averaged Q values at -100 dBm ($\times 10^4$)		$\delta f_{(0K-300K)}$ (kHz)
				Q_i	Q_c	
5	60	No	Yes	6.7 ± 0.1	9.7 ± 0.6	122.0 ± 2.9
6	60	Yes	Yes	13.8 ± 0.6	10.3 ± 0.5	37.7 ± 0.7
7	20	Yes	Yes	13.1 ± 0.5	10.0 ± 0.5	7.5 ± 0.1
8	60	Yes	No	6.4 ± 0.2	9.7 ± 0.4	97.3 ± 4.0

8.2 Low -Resolution Spectral Characterization

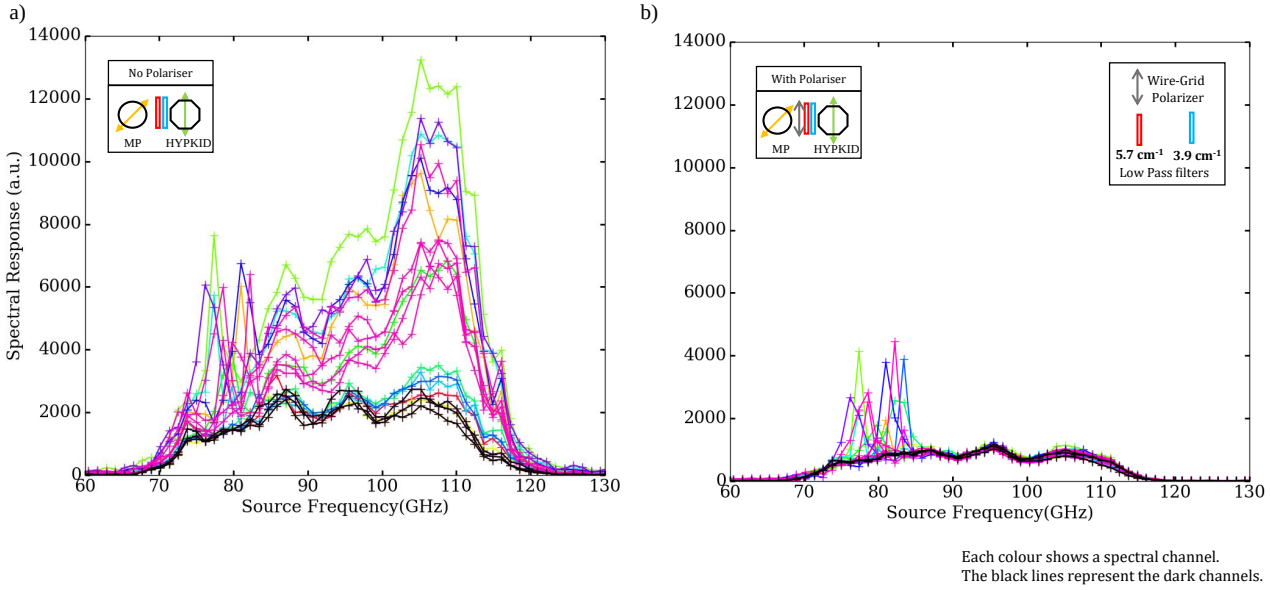

Figure 8.2: Spectral responses of the HYPKID device (HY-Si) using the MPI Fourier Transform Spectrometer (FTS) described in Section 6.5. Both measurements were done in the same optical configuration, apart from without (a) and with (b) the cold wire-grid polarisers in front of the array. Each of two polarizations, InPol and CrossPol are broadcasted inside by the position of the MPI. The polariser selects InPol signal in (b). The black signal represents the response of the channels without the filters. We see the effect of the polarisation filtering the common (continuum) mode is suppressed in (b). Different colours refer to different channels.

To verify the broadband characteristics of the device, a response spectrum, described in 6.5 has been taken with the Fourier transform MPI at a spectral resolution of around 1 GHz, i.e.

not resolving fully the HYPKID spectral response. The low frequency cut-off of the spectrum (69 GHz) is a consequence of the superconducting gap of the sensor (LEKID) material, TiAl, while the high frequency cut-off is fixed by the optical low-pass filters. The spectral responses for all the channels are shown in 8.2(a). We measure the spectrum keeping the MPI at a 45° position in which the input signal contains both polarizations (InPol and CrossPol). The spectral peaks are present together with a strong common background signal.
The common (continuum) mode can be reduced with the polariser. The wire-grid polariser is made by parallel metal wires. The polarisation component of the incoming signal which is parallel to the wires is reflected while the perpendicular component is transmitted. After the polariser, the device is kept in such a way that InPol is parallel to the transmitted polarization. Fig.8.2(b) shows the effect of the cold polariser to suppress the common (continuum) response while preserving the spectrally filtered one.
The residual common signal is due to the component of stray light, mostly absorbed directly by the LEKIDs. This hypothesis is confirmed by the fact that the common mode is also present in the dark channels (with no filters, black lines).

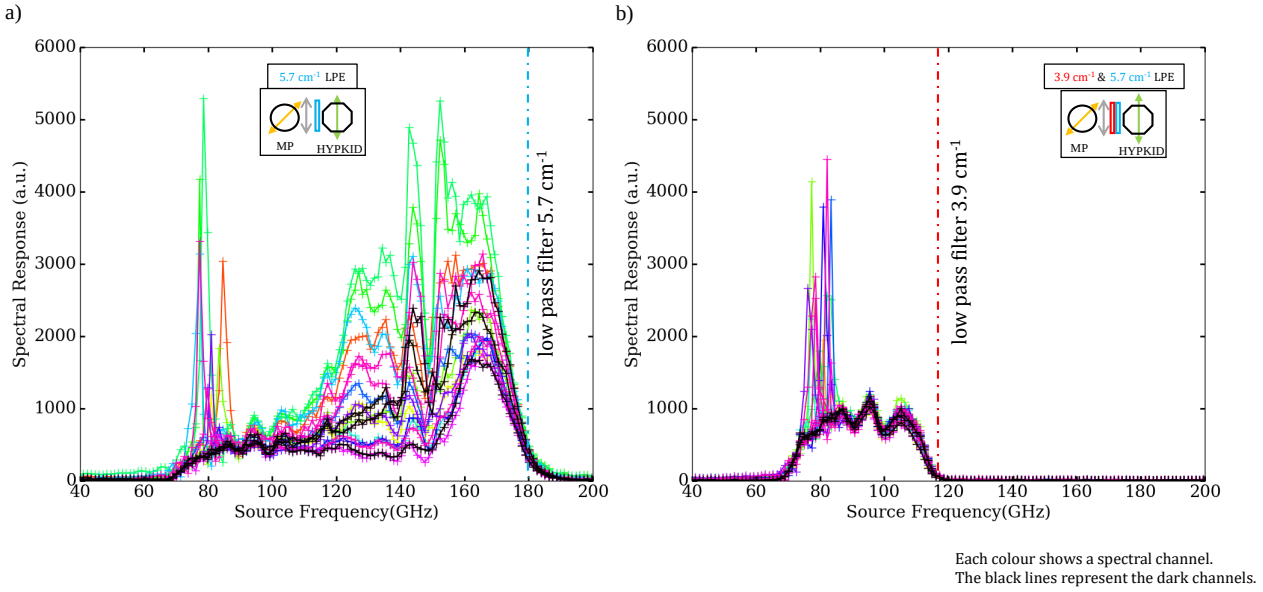

Figure 8.3: Spectral response of HYPKID device using a Fourier Transform MPI (a) with 5.7 cm^{-1} LPE filter and (b) with 5.7 cm^{-1} and 3.9 cm^{-1} filters. We see that the common(continuum) signal related to the stray light is increasing above 100 GHz. Different colours refer to different channels.

Besides filtering out the signal with the polariser, it is also crucial to employ the appropriate

low-pass filter, as depicted in Fig. 8.3. The inclusion of a 5.7 cm^{-1} low-pass filter results in a signal cut-off around 180 GHz, displaying a continuous signal within the high-frequency range of 120-180 GHz. By incorporating an additional low-pass filter of 3.9 cm^{-1}, the impact of high frequencies is eliminated, as any signal above 120 GHz is effectively filtered out. We stress that above 95 GHz the horns become multimodal, explaining the possible increase of stray light absorbed by the LEKIDs.
The spectral resolution of the MPI, in this chosen configuration, is $\sim$ 1.2 GHz, limited by the range of the moving mirror. The simulated resonance frequency of the absorber predicts a bandwidth of 0.2-0.4 GHz. Thus, the peaks observed in 70 GHz to 80 GHz for the device for InPol polarization are not resolved. However, the signal in the peak compared to the continuum can be used to estimate the contribution of the c-shaped absorber to the optical frequency shift observed with the blackbody sources (see $\delta f_{0K-300K}$ of Table. 8.1 and 8.2). We evaluate that 10-15% of the total signal between 69 GHz -120 GHz can be attributed to the peak.
Even in the InPol polarization, there is a non-negligible background most probably due to the stray light. This can be reduced by introducing mesh-like ground structure or adding absorber mesh patches at available empty spaces in future devices. On the top of that, we will add absorbing material around the waveguide end to suppress back-reflections in front of the array.

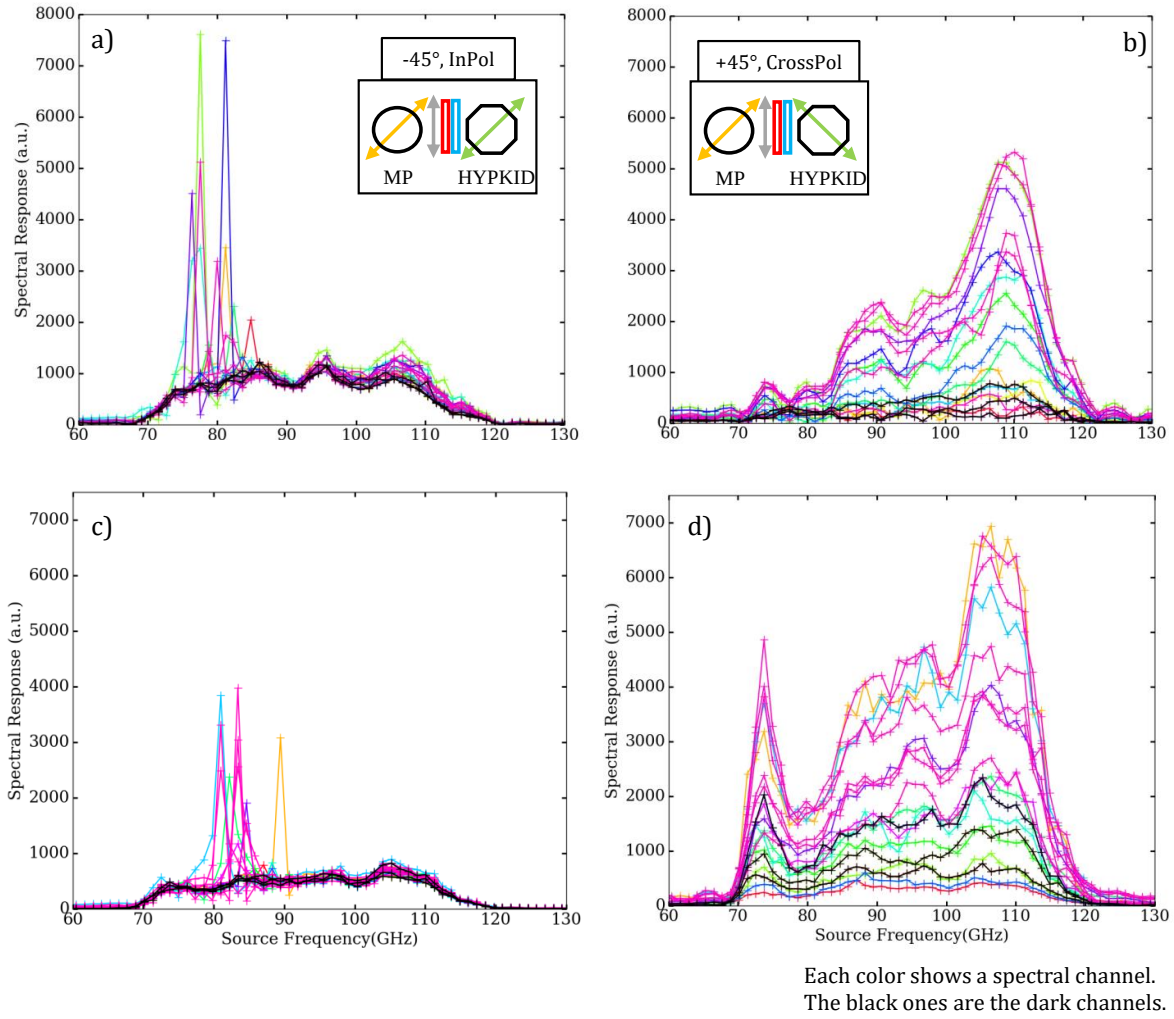

Figure 8.4: Spectral responses of the HYPKID devices on silicon for device HY-Si (top pannel) and on sapphire for device HY-Al2 (down panel) for MPI positioned in parallel (InPol) polarization (a, c) and perpendicular (CrossPol) polarization (b, d). Different colours refer to different channels.

8.3 High Resolution Spectral Characterization

The mm-wave source operating in the frequency range 75 GHz -110 GHz is used for the measurement of the spectral resolution of the peaks observed in the previous (lower resolution) MPI measurement. Fig. 8.5 illustrates the shift in the resonance frequency of the channels when the device is illuminated with the horizontally and vertically polarized incoming signal. The polarization selectivity is clearly evidenced. This device was made on sapphire. We test the device on silicon substrate as well.

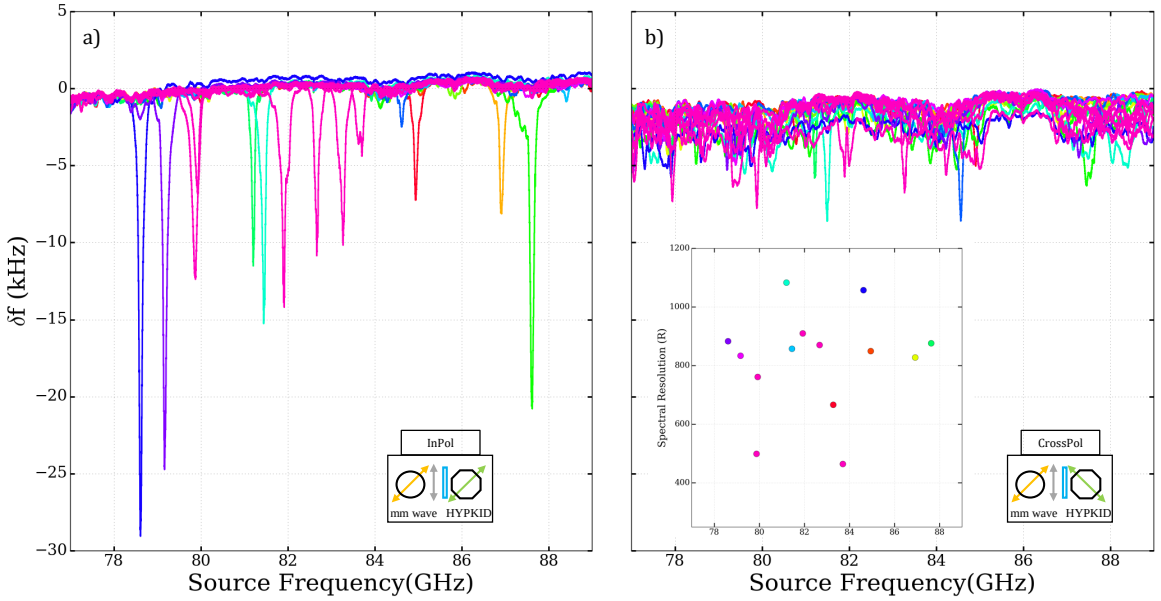

Figure 8.5: High resolution (10 MHz) spectral responses of the HYPKID on sapphire device HY-Al1 for (a) InPol and (b) CrossPol directions with five eccosorbs. Different colours refer to different channels.

The intensity of output signal of the source is not calibrated over the range. Hence, this source is not optimized for photometric measurements. The high source power of the mm wave source is attenuated using multiple Eccosorb^{TM} sheets, sandwiched in between two metal rings, placed in front of the cryostat window lens. Fig. 8.6 and 8.7 show the measurements on device HY-Si. The number of eccosorbs was decreased from six for Fig. 8.6 to five for Fig. 8.7. Sixteen out of sixteen of the spectral channels are showing distinguished minimums in the 76-87 GHz frequency range. A frequency shift of 2-5 kHz in average for all the channels with six eccosorbs. Simultaneously, when a single sheet of eccosorb is eliminated, there is a notable increase in the magnitude of the frequency shift. The spectral channels experience a frequency shift ranging from approximately 100-250 kHz for five eccosorbs. From this, we have estimated a factor 25 attenuation per sheet. Six eccosorbs provides an estimated attenuation factor of

$25^6 \sim 2.5 \times 10^8$. As shown in Fig. 8.7, the overall common signal in the background has also exhibited a significant rise compared to Fig. 8.6 varying for different channels. The spectral resolution of the channels varies in between 200-550 (in agreement with the simulations). The non-spectral channels provides the information on the continuum background that is observed also for the spectral channels. The common frequency shift is on average 200 Hz over the band. Thus, the integral of signal in the spectral dip compared to the integral of all the signal in the range of 75-110 GHz is 15 (lowest)-60 (highest)% across the 16 channels. In conclusion, the spectral resolution of each channel is demonstrated by the mm-wave source and it is in agreement with simulations.
In the case of the HYPKID device, each spectroscopy channel occupies a distinct position. To perform spectroscopic measurements on a specific object using the HYPKID device, it is necessary to determine the position of each channel on the array. Thus, we conduct the following measurement to determine the array's geometry.

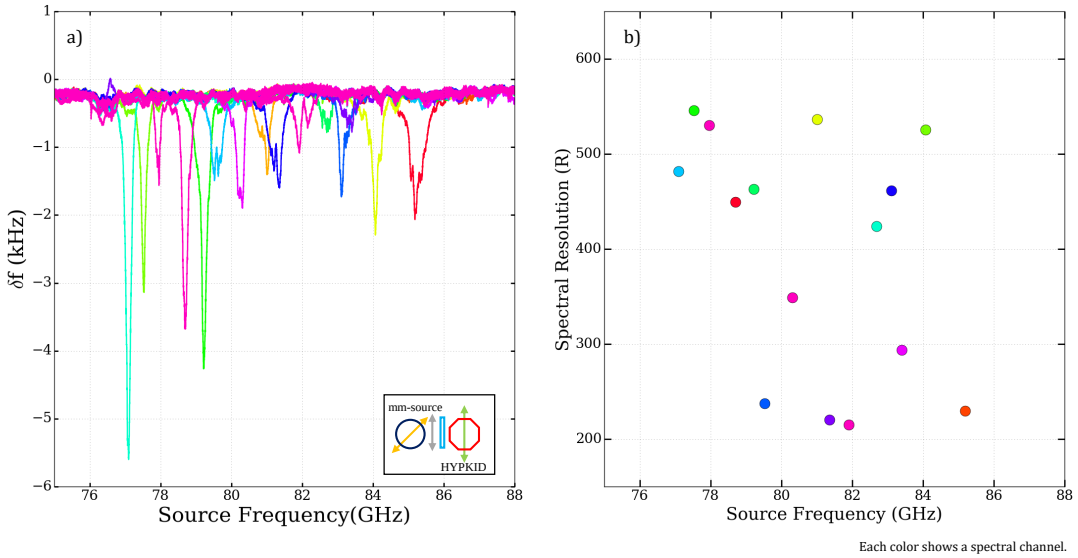

Figure 8.6: (a) Spectral responses in terms of frequency shift (δf) of the channels of HYPKID device HY-Si using mm wave source (with six eccosorbs) for both InPol and CrossPol polarized signal. Black line shows the average response of the three non-spectral LEKIDs. (b) The spectral responses of the channels 400±100 with large dispersion. Different colours refer to different channels.

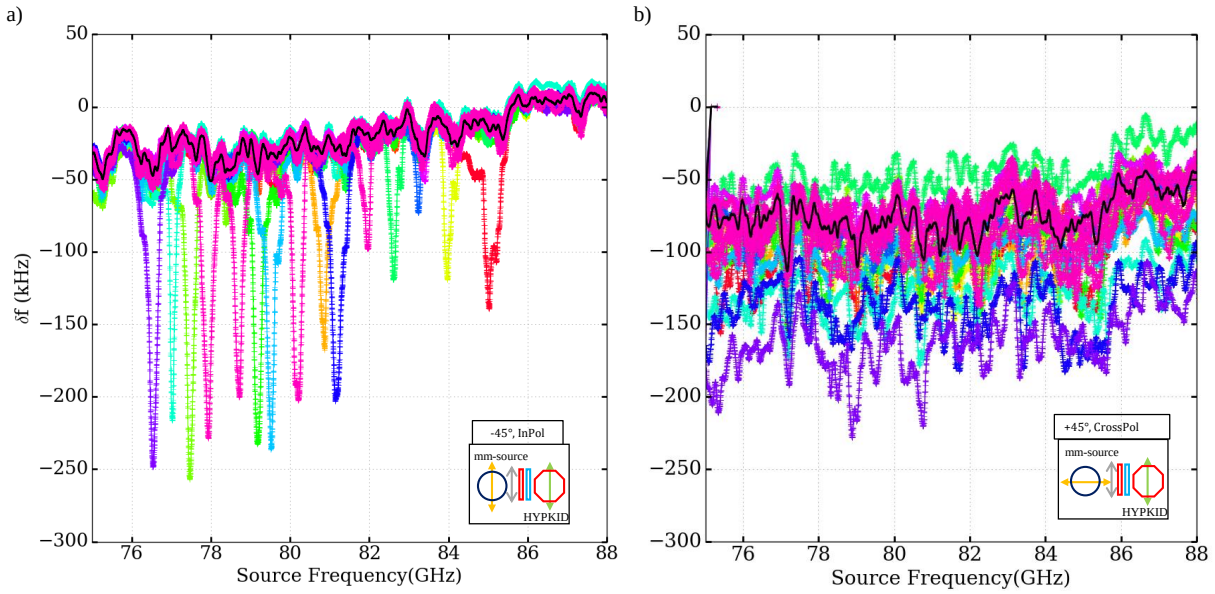

Figure 8.7: Spectral responses of HYPKID device HY-Si using mm wave source (with five eccosorb sheets) at parallel (InPol)(a) and perpendicular polarization(CrossPol)(b), the black line shows the average response of the three non-spectral (without filters) LEKIDs. Different colours refer to different channels.

8.4 Array Geometry and Spectral Imaging

The sky simulator allows to reconstruct the channels position in the array and demonstrates the spectral imaging. The measurement set-up is described in Section. 6.7. In Run 4, the HYPKID device (HY-Al2 and HY-Si) was placed at 45° with respect to the horizontal line. Two of the three dark channels' horns were closed with aluminum tape to suppress the stray signal. The XY scan was carried along the y position, keeping a fixed x position. The x position was changed by 11 mm at each sub-scan. Fig. 8.8 shows the response of one of the channels (typical pixel) with x movement and y movement. The maximum frequency shift corresponds to the "planet" aligned with the channel (horn) position. The vertical lines in the x position represents the particular x position during the y sub scan. Depending on the position of the channel, we observe a Gaussian profile in the frequency shift (signal). A constant frequency shift is observed corresponding to the wire used for hanging the "planet".
Fig. 8.9 shows all the channels responses over time while moving the planet. Multiple Gaussian curves is observed, showing clearly that each pixel is "seeing" a different portion of the sky simulator.

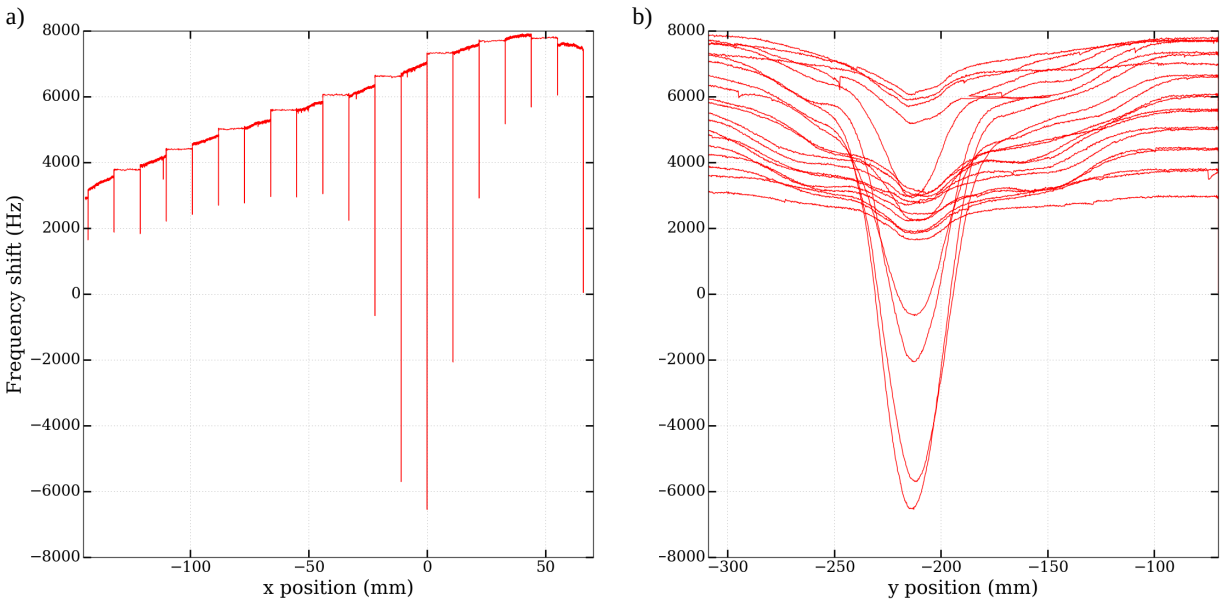

Figure 8.8: The frequency shift of the scan of the sky simulator for a typical channel as a function of the (a) X raw position and (b) Y raw position of the "Planet" sub scans.

To summarize, the dips represent the motion of the 300 K blackbody, named "the Planet", in front of each of the 16 channels. The XY position for the maximum frequency shift indicates the geometrical location of the particular channel in the array.
Fig. 8.10 presents the maximum frequency shift in the colour bar at the XY-channel position. The deduced array geometry exactly replicates the designed geometry. The two dark LEKIDs position show in white circles which were not illuminated because they were aluminum taped. Thus their positions are arbitrarily drawn (not measured).
An intensity variation of the frequency shifts is observed for the LEKIDs which were away from the centre of the device. This is due to focal plane size in the NIKA0 cryostat, smaller than the HYPKID array. In other words, the "Planet" signal is vignetted out of the inner focal plane part.
We discuss in this chapter the measurements done on the 19 channels HYPKID device. In the next chapter, we will provide the data analysis done to measure the sensitivity of the device.

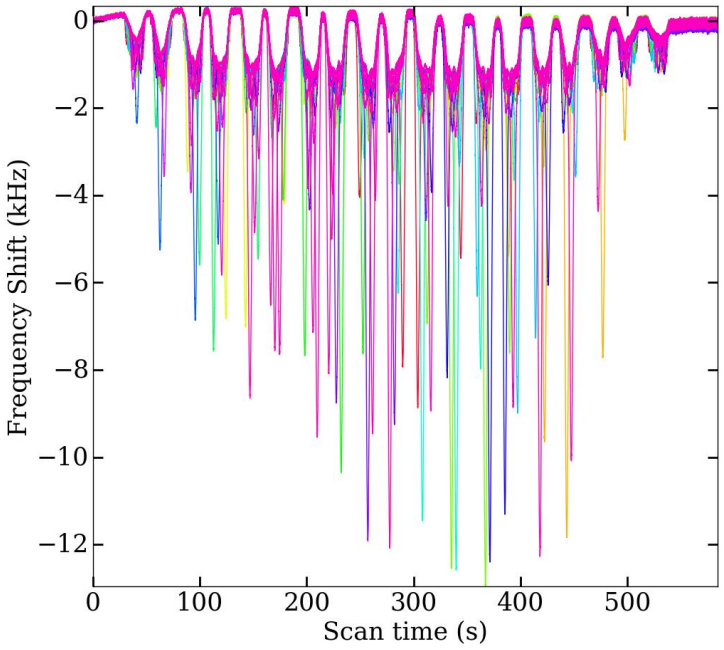

Figure 8.9: The time scan of the HYPKID array with the sky simulator. The scan speed is 11 mm/sec in y direction. Each color represents the frequency shift of a channel.

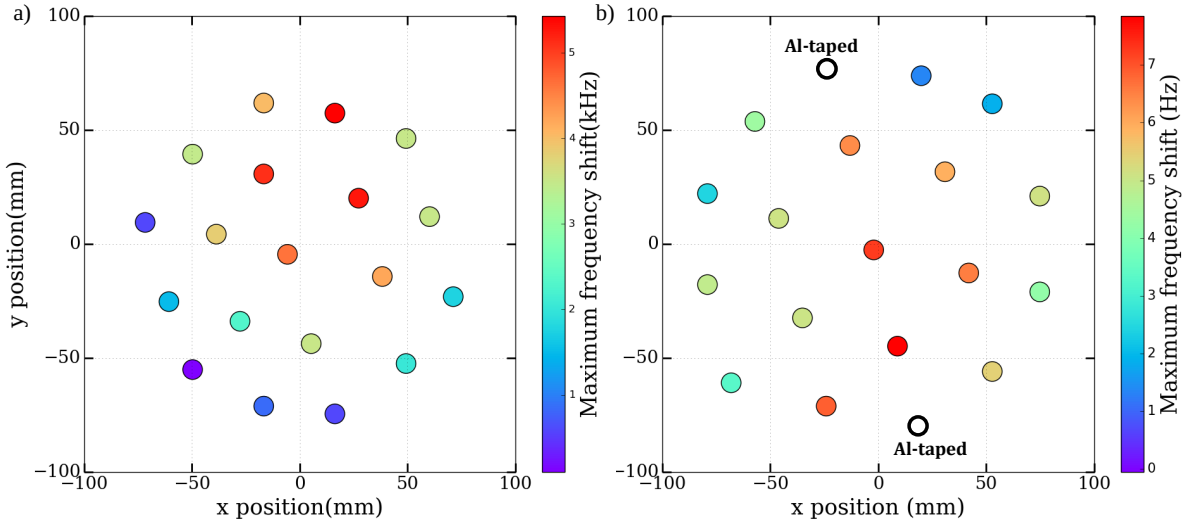

Figure 8.10: Array geometry deduced from the sky simulator measurement: The XY position of the maximum frequency shift of the LEKIDs for HYPKID on sapphire, HY-Al2 (a) and silicon, HY-Si (b). The colours indicate the frequency shift intensity: high(red) and low(blue). The variation of the intensity of the maximum frequency shift is most probably the result of the optical vignetting. On top of that, it seems that a slight misalignment affected the measurement. In Fig. (b), the two white circles at two end are the position where the dark LEKIDs were closed with Aluminum tapes (drawn only to clarify using their nominal designed positions).

Chapter 9

Data analysis

Based on the measurements presented in the preceding two chapters, we demonstrate that both OMKID and HYPKID serve as operational spectroscopic devices for detecting mm wave length. In this chapter, we progress further by evaluating how efficient our devices are. We gauge sensitivity through measurements of noise equivalent power and noise equivalent temperature. In both cases, a lower value signifies a higher sensitivity level for the device. Additionally, we discuss the superconducting characteristics of the titanium aluminum (TiAl) bilayer employed in LEKIDs. Furthermore, we explore the efficiency of the LEKIDs made with a 20 nm thick aluminum (Al) layer and a 35 nm thick TiAl bilayer used in our devices.

9.1 Noise Equivalent Power (NEP)

The device sensitivity behaviour is quantified by calculating the noise equivalent power (NEP), i.e., the amount of input power equivalent to the RMS noise per square root Hz. In other words, if the device is illuminated with a signal equivalent to this noise equivalent power, the signal to noise ratio will be one in a 1 Hz bandwidth. The NEP of the device for the incoming signal over the bandwidth and for a given pixel is given by:

$$\mathbf{NEP^{(10\ Hz)}} = \frac{\mathbf{\Delta W \times N^{(10\ Hz)}}}{\delta \mathbf{f}} \tag{9.1}$$

- ΔW is the change of the input power on a pixel.
- δf is frequency shift of the LEKIDs corresponding to ΔW.
- The noise spectral density (N) is the estimated by convention at a readout frequency of 10 Hz and is measured in Hz/$\sqrt{Hz}$.

As explained in Section 6.6, the millimeter-wave source intensity is not calibrated over the frequency. Therefore, a direct evaluation of the optical load for an illumination with the millimeter is not feasible. To overcome this difficulty, we used an illumination with a black-body source. In this method, we measured the frequency shift per channel for the 0 K-300 K temperature change of the black-body source. We estimated the corresponding change in the optical load per unit area using three-dimensional ray-tracing optical design software ($ZEMAX$), where the inputs are the spectral luminescence of the black-body source, the geometry of the cryostat (the apertures, the distances, and the curvatures and materials of the lenses), and the collecting surface. We simulate the optical load for a unit area and for a specific frequency.
The horn-waveguide feed is used as the optical coupler for both OMKID and HYPKID devices. In OMKID, all the channels received signals through the mm wave line and they got signals

through the horn-coupled slot shape. In HYPKID, each spectral channel receives the signal through the horn-waveguide set-up. The horn has an area of 50 mm^2 and the efficiency of the smooth flared surface of the horn is estimated at around 60%. Thus the effective area of the horn is 30 mm^2.
Considering a Lorentzian spectral profile, in the FWHM we have half the power with respect to the full integral. Making a simplified assumption of a constant illumination power over the whole band, 75-110 GHz for both sources(0 K, 300 K), we estimate that the common background signal contributes to about half the total response. We have calculated the optical load for the bandwidth of the spectral channel.
Another important aspect to consider is the presence of polarization in the optical transmission as only half of the signal is transferred to the array if polariser is used.
Total optical load = Optical load per unit area per frequency× Effective illumination surface × Polarization effect × Spectral channel bandwidth (Avg.)
The typical noise power spectral density is considered at a sampling frequency of 10 Hz and averaged over all the LEKIDs. The noise at lower f is mostly correlated across the pixels, and can thus be efficiently removed using an appropriate decorrelation technique during data analysis. The noise level is optimized by choosing an appropriate readout power.
In the NIKA0 cryostat, when the blackbody temperature varies between 300 K and 0 K in the 75-110 GHz band, the optical load varies with an average 0.4 ± 0.1 pW/mm^2 for a single polarization. In the 80-81 GHz band, it is 4.5-5 ± 3 fW/mm^2 for the 1 GHz band and in 100-101 GHz band, it is given by 7 fW/mm^2 with 20 mm diameter of the pupil. The error bar rises from the number of rays traced in the simulation. The transmission of the filters and lenses are assumed 35%. The pupil area at 100 mK is typically taken into account in the simulation. As the relative area between two pupils is $60^2/20^2 = 9$, we can expect a variation of 9 for the change in pupil size between the full 60 mm and the reduced 20 mm.
The total optical load is calculated for the OMKID and HYPKID. For OMKID, the filter resonances are over the full range of 80-110 GHz with a bandwidth of 0.2 GHz each. For HYPKID, they are in the 78-88 GHz range with a bandwidth of 0.4 GHz.

9.1.1 NEP for OMKID

We consider the horn-slot antenna configuration as baseline for this estimation. In Table. 9.1, we evaluate the NEP for two OMKID devices measured in this configuration, OM-D4 and OM-D6. The optical set-up was the same for these two measurements.
For OMKID, the spectral responses measured with the millimetre-wave source show a channel response with a peak of about -5 kHz over a 0.4 GHz band (on average). The continuum background is about -100 Hz.
The measured 0-300 K frequency shift (with the VNA) results from the combined monochromatic response and the continuum response.

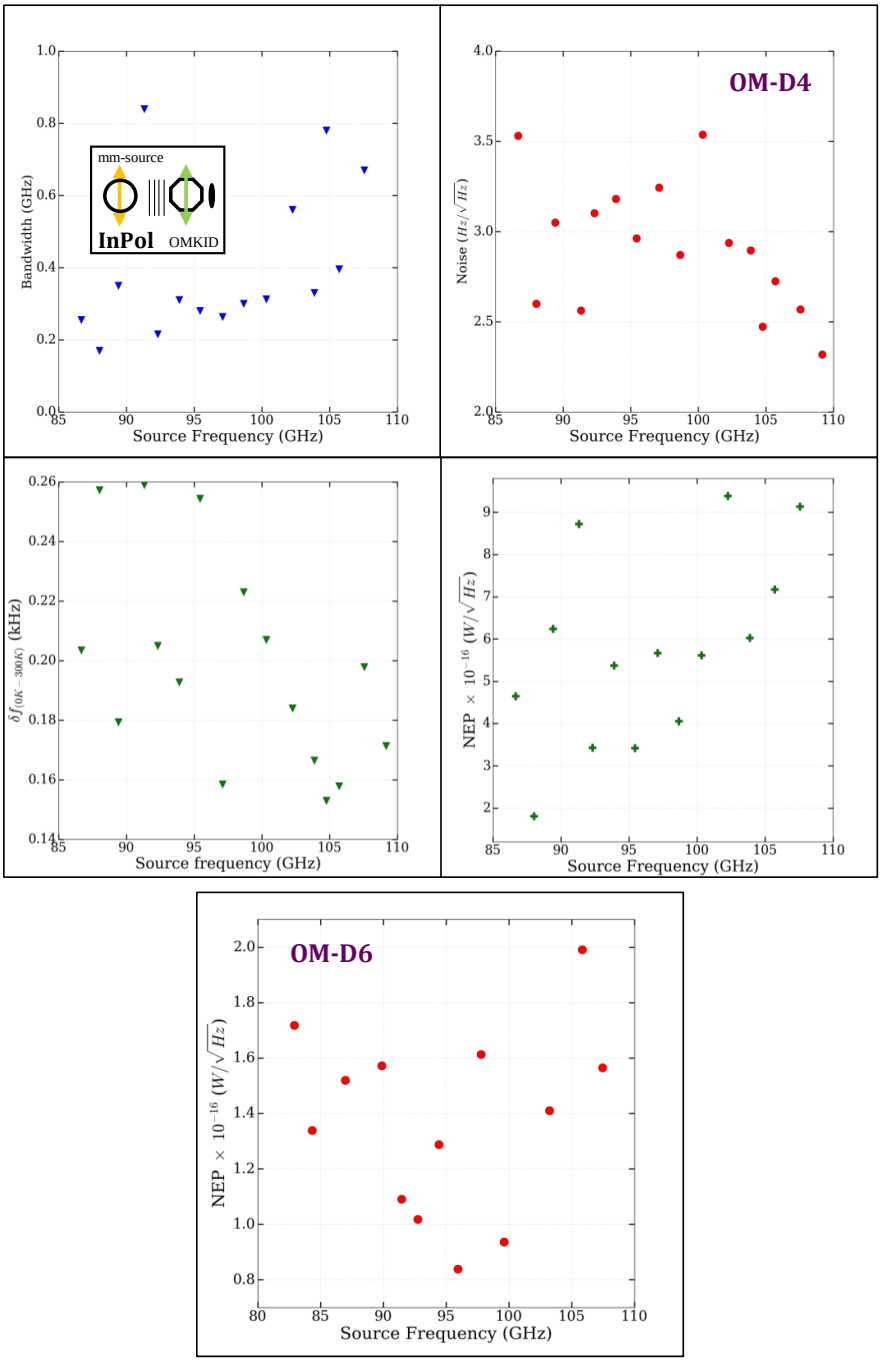

Figure 9.1: Calculation of NEP for OM-D4 and OM-D6 devices:

Table 9.1: Average Noise Equivalent Power for two OMKID devices, OM-D4 and OM-D6

Run No.	Cold Pupil (mm)	δW_{opt} (fW)	N (Hz/$\sqrt{\text{Hz}}$)	δf (0-300K) (kHz)	NEP^{bb} (W/$\sqrt{\text{Hz}}$)
OM-D4	20	42	3	0.2	5.8×10^{-16}
OM-D6	20	42	1.8	0.5	1.5×10^{-16}

In Table. 9.1, we conservatively use the optical load for the 1 GHz band as the spectral resolution of OMKID spectral channels varies in between 200-600. Thus, the bandwidth for the spectral channels is between 0.15-0.6 GHz . To be more conservative, we take into account the optical load for the frequency range of 100-101 GHz considering an upper limit in the band 80-110 GHz. For the single polarization and 20 mm pupil diameter, the optical load is given by 7 fW/mm^2/GHz $\times$ 30 mm^2 $\times$ 0.5 $\times$ 0.4 GHz = 42 fW. The noise is evaluated from the average of the pixels at 3 Hz/$\sqrt{\text{Hz}}$. Thus, we calculated NEP in the 0.5 fW/$\sqrt{\text{Hz}}$ range.

9.1.2 NEP for HYPKID

For HYPKID, the measurement set-up was optimized via many experiments. The spectral response of all channels is between 78-88 GHz. Depending on the presence of different sizes of pupil and polariser, we calculated the total optical load as shown in Table 9.2.

Table 9.2: Average Noise Equivalent Power for HYPKID devices, HY-Al1, HY-Al2 and HY-Si1

Run No.	Cold Pupil (mm)	Filter (3.9 cm^{-1})	Spacer	Cold Polarizer	ΔW_{opt} (fW)	N (Hz/$\sqrt{\text{Hz}}$) at 300K	δf – VNA 0-300 K (kHz)	NEP^{bb} (W/$\sqrt{\text{Hz}}$)
HY-Al1-1	20	Y	N	N	13.5	4.8	4.7	2.7×10^{-16}
HY-Al1-2	20	Y	N	Y	6.75	4.0	2.6	2.1×10^{-16}
HY-Al1-3	60	Y	N	Y	108	4.1	14.4	3.0×10^{-16}
HY-Al2-4	60	Y	Y	N	216	2.8	79.5	8.0×10^{-17}
HY-Si1-5	60	N	Y	Y	108	2.7	132	2.0×10^{-17}
HY-Si1-6	60	Y	Y	Y	108	4.4	51	9.0×10^{-17}
HY-Si1-7	20	Y	Y	Y	13.5	2.5	7.3	4.0×10^{-17}
HY-Si1-8	60	Y	Y	N	216	3.4	123	6.0×10^{-17}

The noise level varies between 2-5 Hz/$\sqrt{\text{Hz}}$. The frequency shift depends on the optical settings. Say, for 20 mm and single polarization, the optical load is calculated as 4.5 fW/mm^2 GHz $\times$ 30 mm^2 $\times$ 0.5 $\times$ 0.1 GHz = 6.75 fW.
For HYPKID, the LEKIDs are partially exposed and can directly absorb the incoming radiation. Thus, the effect of the common continuum on the channel response must be considered while calculating the NEP value. For this reason, we also use the MPI data for this estimation. Despite the fact that the MPI, with a resolution of 1.2 GHz is not resolving the peaks, we can use the spectra to evaluate the fraction of energy contained in the peaked spectral bin and compare it with the integral across the full band. From this, we have calculated that, on

average only 10% of the signal can be attributed to the filtered (peaked) response. This has been considered in the NEP calculation.

9.2 Noise equivalent Temperature (NET)

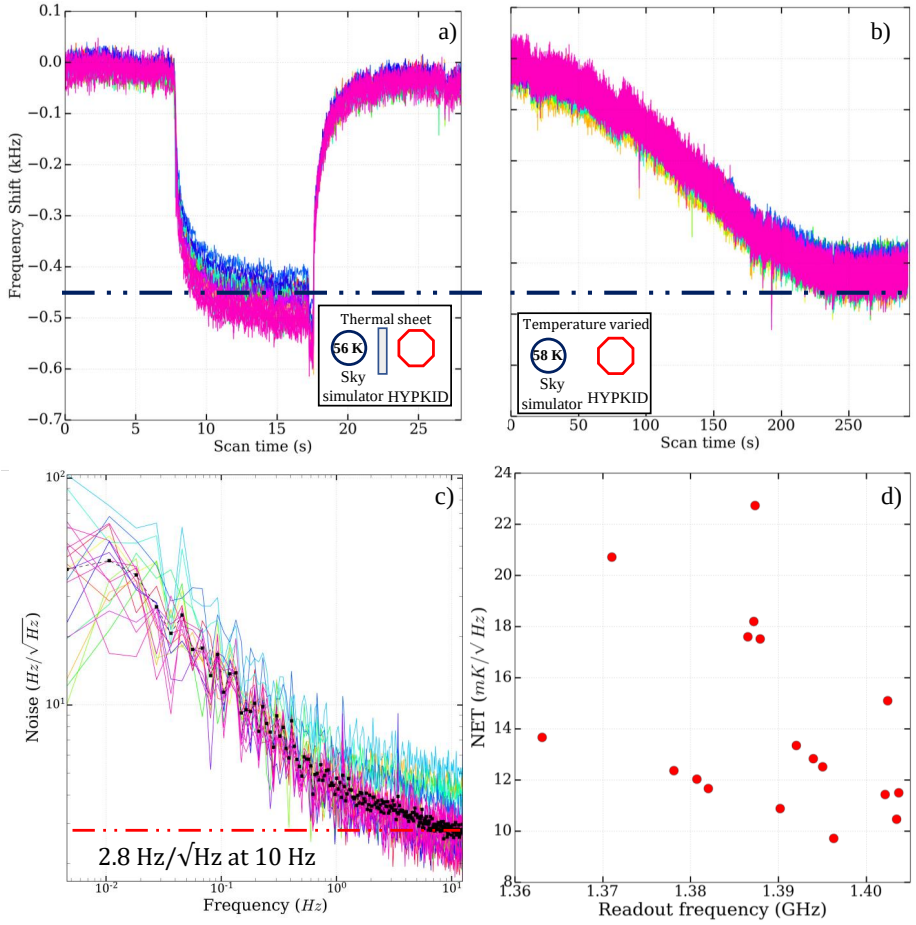

Figure 9.2: Measurement of the Noise Equivalent Temperature (NET): (a) A polystyrene sheet is inserted between the sky simulator and the cryostat. The temperature of the sky simulator at this condition was 56 K. The frequency shift of the resonance frequency of the LEKIDs was around 400 Hz to 550 Hz depending on the LEKIDs. (b) The temperature of the sky simulator was increased by 2 K to reproduce the same frequency shift of the LEKIDs and calibrate the background associated with the polystyrene sheet. (c) The average noise level of the detectors with the sky simulator was on average 2.8 Hz/$\sqrt{\text{Hz}}$ at 10 Hz. (d) The resulting NET of the HYPKID device averaged over the channels is around 12 mK/$\sqrt{\text{Hz}}$. This includes the continuum contribution.

While the NEP is usually adopted to establish the performance of the focal plane, the noise equivalent temperature (NET) is another convenient (less model dependent) quantity to describe the performance of a full photon detection system. The NET is defined as the ratio between the temperature difference (ΔT) of an extended source in front of the camera and the signal to noise ratio (SNR) measurement with which this ΔT is detected.

$$NET = \frac{\Delta T}{SNR} \left[\frac{\mathrm{mK}}{\sqrt{\mathrm{Hz}}}\right] \tag{9.2}$$

In other words, if the background, e.g., the sky temperature, varies by the NET value, the step is detected with a signal to noise ratio equivalent to 1 in 1 Hz bandwidth. We measure the NET of the HYPKID device on the basis of the available optics and system set-up and compare it with the NIKA camera (for example). The diameter of the (cold) focal plane of the NIKA0 camera is around 36 mm, whereas the horn diameter of one channel is around 8 mm. It can be assumed that the background temperature of the source is optimized for each channel. The sky simulator source is perturbed by a thin sheet of polystyrene, causing a frequency shift of 400-550 Hz on the detectors. This is produced due to the emissivity (or the absorption) of the sheet. The sky simulator temperature can be modulated with a heater to reproduce same frequency shift. In this way, we have determined that the equivalent of the polystyrene sheet has a temperature difference of around 2 K. Thus, the signal divided by the noise spectral density at 10 Hz with the temperature difference indicates the NET of the detector. The results of the measurement are shown in the Fig. 9.2. Using the equation 9.2, the NET value of the HYPKID device (HY-Al2-4) varies from 8-24 mK/$\sqrt{\mathrm{Hz}}$ depending on the pixels.

9.3 Evaluation of the efficiency

The efficiency of a detector is defined by the ratio between the number of detected photons and the number of incident photons. The optically generated quasi particles ($n_{qp}^{optical}$) is compared with the thermally generated quasi particles (n_{qp}) in this measurement. The HYPKID device is installed in the lowest temperature stage of the cryostat, called 100 mK stage. The temperature of the thermal bath is swept from the base temperature of 90 mK to 300 mK using a heater. Before taking the data with different probe powers, there was a waiting time of 10-15 minutes to thermalize the device with the mixing chamber temperature. Fig. 9.3 (a) shows the change in S21 parameter for different temperatures for one channel at -105 dBm probe power. The frequency shift (δf) with respect to the resonance frequency at base temperature (f_0) for different temperatures is shown in Fig. 9.3 (b).

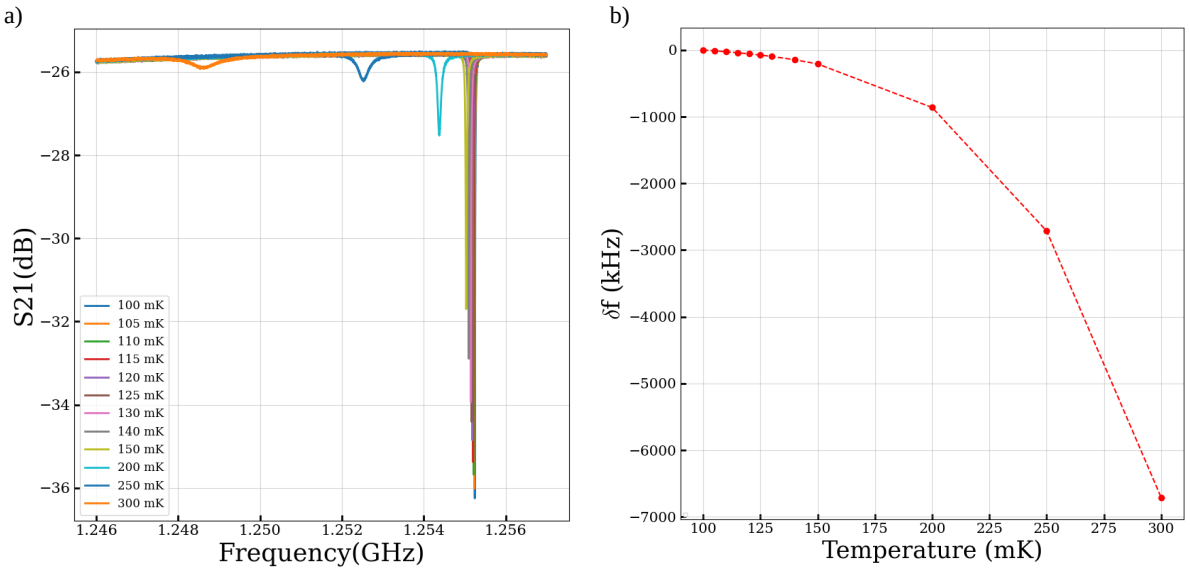

Figure 9.3: Temperature Sweep shown for one channel at -105 dBm probe power. (a) The S21 transmission of one channel for several temperatures shows a decrease in resonance frequency (a degradation of the Q factor) with increasing temperature. (b) The frequency shift with respect to the base frequency is shown for temperature.

The efficiency η is and is usually evaluated with the following formulas:

$$n_{qp}^{optical} = \eta \frac{\Delta W_{load} \tau_{qp}}{\Delta_0} \tag{9.3}$$

and

$$n_{qp} = \left[2N_0 \sqrt{2\pi k_B T \Delta} \exp(-\Delta/(k_B T)) \right] \tag{9.4}$$

We find that $T = 116$ mK is the temperature for which $\delta f^{qp}(T) = \delta f^{light}(\Delta W_{load})$ i.e., the optical shift equivalent. The thermally generated quasi particles can be modelled using the Mattis-Bardeen theory. The fractional change in resonator is given by $\frac{\delta f}{f} = \frac{f - f_0}{f_0}$ where f_0 is the centre frequency of a LEKID at the minimum base temperature reached.

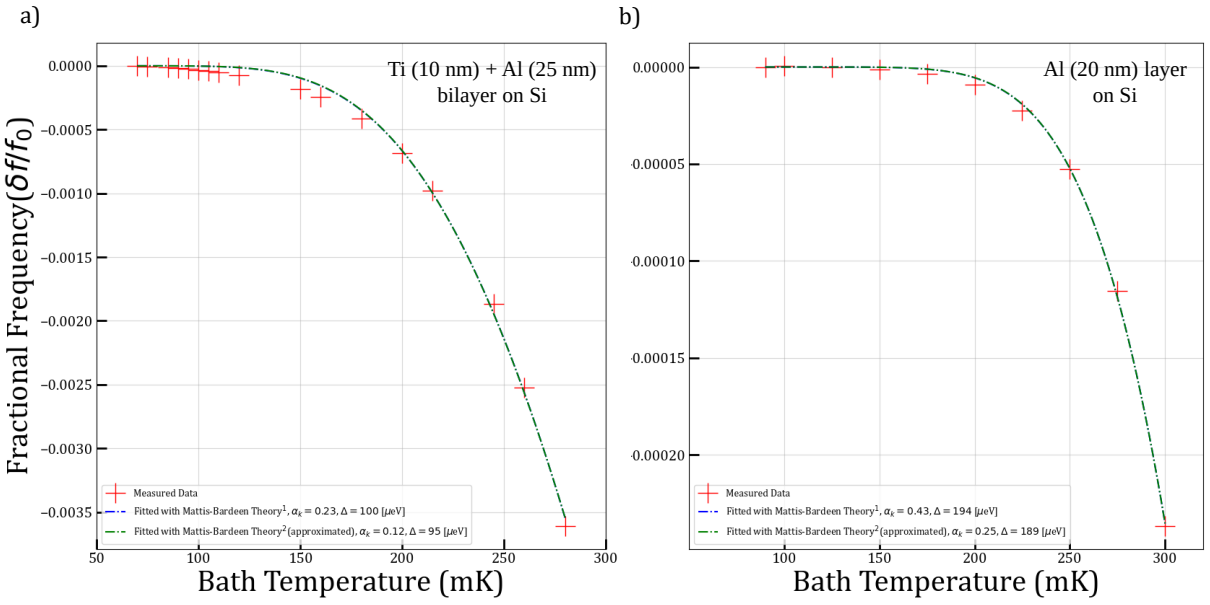

Figure 9.4: The fractional frequency shift is recorded for the TiAl bilayer (a) and thin Al layer (b) while the base temperature is swept. The data is fitted using Mattis-Bardeen theory.

For fitting the measured data, we use two equations [Diener et al., 2012] [McCarrick et al., 2014] relevant to extract the superconducting gap frequency and kinetic inductance fraction. The equations are both developed and approximated from Mattis-Bardeen Theory.
For dirty and thin superconductor films for $T < T_c/3$ and $hf \leq \Delta$, the change in resonance frequency as a function of bath temperature (T) is given by,

$$\frac{\delta f}{f_0} = -\alpha \left[\tanh\left(\frac{\Delta}{2k_B T}\right)^{-\frac{1}{2}} - 1 \right] \tag{9.5}$$

At temperature below $T \leq T_c/10$, the Mattis-Bardeen formula can be provided,

$$\frac{\delta f}{f_0} = -\frac{\alpha}{4N_0\Delta} \left[1 + \sqrt{\frac{2\Delta}{\pi k_B T}} e^{\left(-\frac{hf}{2k_B T}\right)} I_0\left(\frac{hf}{2k_B T}\right) \right] \times \left[2N_0 \sqrt{2\pi k_B T \Delta}\; e^{-\frac{\Delta}{k_B T}} \right] \tag{9.6}$$

As the bath temperature is varied, the number of thermally generated quasiparticles in the film increases. This increase in quasiparticle density leads to additional microwave losses, contributing to the resistive part (σ_1) and reducing the Q values. Simultaneously, the increasing kinetic inductance ($1/\sigma_2$) induces a shift in the resonance frequency.
To analyze the measured data, we attempted to fit the formulas using the aforementioned equations, considering two free parameters, α and Δ. However, both the bilayer and the Al

layer did not align well with the equations. The values of the free parameters reached saturation and differed from our measured values. The most likely reason for this discrepancy could be a thermalization issue in the sample holder or the films not being adequately described by the Mattis-Bardeen formula.

9.3.1 Superconducting properties of TiAl bilayer

The kinetic inductance is determined by the film thickness, penetration depth, and specific geometry. A thin wire of TiAl film deposited on silicon is used for the measurement of the transition temperature (T_c), transition width (ΔT_c) and residual resistivity ratio (RRR) using the four wire technique described in Section A.3. The data obtained are shown in Fig. 9.5. The effective parameters of the wire in this measurement are 3.6 mm in length (l), 40 μm wide (w) and 35 nm thick (d).

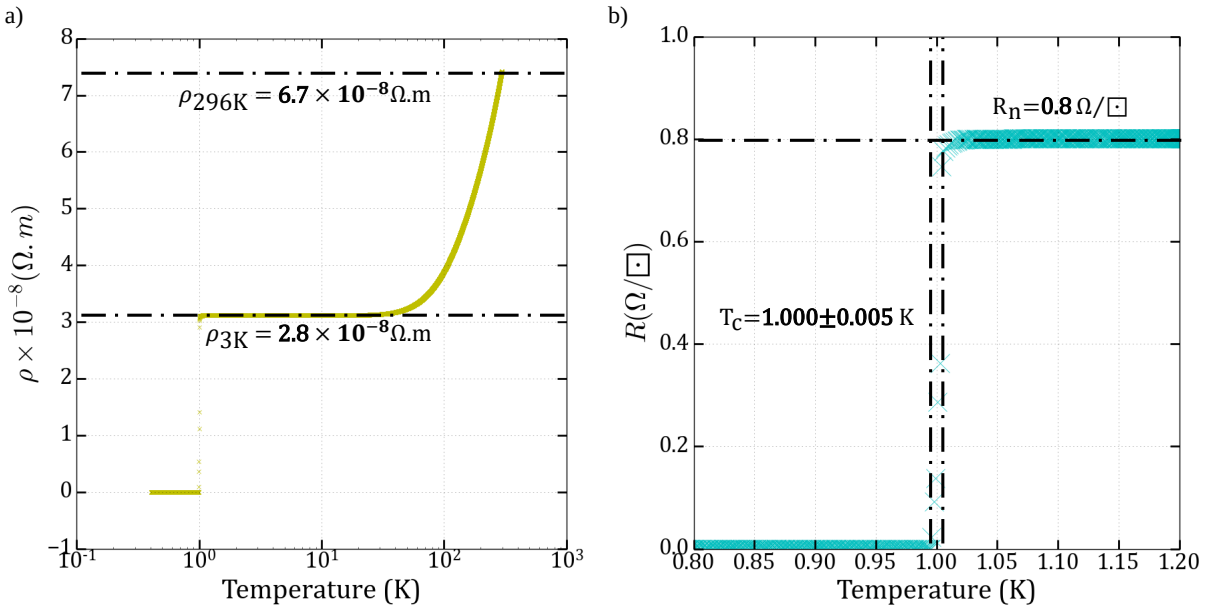

Figure 9.5: Resistance vs. temperature measurement of TiAl layer on Silicon wafer

From this measurement, we can extract information about the properties of the TiAl film used in the experiment. The wire used for the four-wire measurement is different from the array we use, but the fabrication process is the the same. The residual resistance ratio (RRR) is defined as the ratio of the residual resistivity at room temperature ($\approx$ 296 K) to that of just before the superconducting transition ($\approx$ 3 K). This is a signature of the purity of the film, i.e., the mean free path of the electrons. For our sample,

$$RRR = \frac{\rho_{296K}}{\rho_{3K}} = \frac{7.38 \times 10^{-10}\Omega.\mathrm{m}}{3.2 \times 10^{-10}\Omega.\mathrm{m}} = 2.4 \tag{9.7}$$

When the transition temperature is measured at exactly 1 K , we get the superconducting gap (2Δ) as, $\Delta = 1.764 k_B T_c$ where k_B is the Boltzmann constant. The optical gap frequency (ν_f) found in the MPI measurement is 68 $\pm$ 1 GHz which also corresponds to T_c = 1.08 $\pm$ 0.02 K. Assuming our film is well described by the Mattis Bardeen formula linking the real and imaginary contributions to the impedance, we can finally evaluate the kinetic inductance per square:

$$L_s = \hbar R_s / \pi\Delta = 1 \text{ pH}/\square \tag{9.8}$$

where $\hbar$ is the reduced Planck's constant and R_s is the normal sheet resistance per square. It is important to notice that the ageing of the film resulted in an evolution of these values. For example, the T_c went from 1 K to 930 mK over the time span of 150 days.
As discussed in 9.3.1, the evolution of the transition temperature with time is also noticed in the resonance frequencies. There was a shift of 8 MHz in 180 days as shown in Fig.9.6.

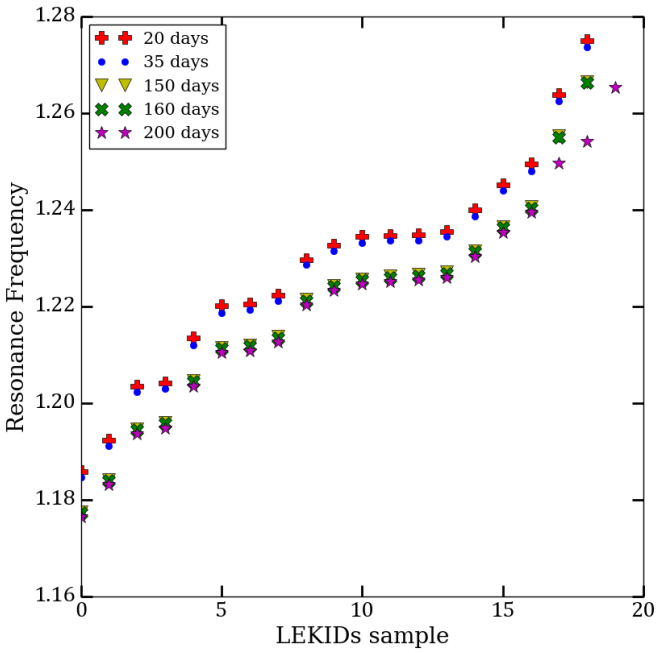

Figure 9.6: The shift in resonance frequencies of the HYPKID on silicon device as observed between various measurements, spanning almost 180 days.

This variation questions the aging behaviour of the TiAl bilayer itself. Even though we have not seen any variation of the transition temperature with time in the bilayer we used for the resistance measurement.

Chapter 10

Future prospects and conclusion

The primary goal of this thesis was to present an overview of the project on on-chip spectrometry. We have successfully developed *OMKID* and *HYPKID* detectors, which is a significant milestone as the first on-chip spectrometers employing LEKIDs in the 90 GHz frequency range. The prototypes have 16 spectral channels for which we can resolve widths of 0.2-0.5 GHz in the frequency band of 75 GHz to 110 GHz. The fabrication process employed was both straightforward and highly reproducible, consistently yielding a remarkable fabrication success rate of approximately 90% throughout the processing stages. The measurement procedures we have developed throughout the thesis timeline are described. We successfully identified nearly all resonances. The noise level was 2-5 Hz/$\sqrt{\text{Hz}}$ which is close to the state-of-the-art. We have found that the detectors are highly sensitive in the range of 10^{-16} W/$\sqrt{\text{Hz}}$. The NEP values are comparable with those of existing state-of-the-art devices in the field. On the basis of the work, we have published two articles describing *OMKID* [Chowdhury, U. et al., 2023] and *HYPKID* [Chowdhury et al., 2023], each showing the achievements and innovations of our research. While our developed measurement setup has proven to be effective, it is vital to emphasize the need for precise calibration of the mm-wave source. This calibration process remains an essential aspect of our ongoing work, ensuring the higher accuracy of the input power.

The concepts of *OMKID* and *HYPKID* are easily adaptable to other atmospheric windows. Currently, we have proposed the development of a 300-channel *HYPKID* design, shown in Fig. 10.1 for 2 mm atmospheric window. The detection frequency range is 120-170 GHz. The device is in the process of being tested. With higher frequencies, the horn radius decreases, introducing a bottleneck for upscaling to a higher frequency band. For *OMKID*, the significant challenge is the transition from the horn-waveguide to the antenna shape. The optimization of the star-slot antenna is also a critical area of focus.

To improve our devices, achieving uniform resolution across the entire frequency band is essential. However, we have observed variations in this aspect. There are multiple hypotheses to explain these discrepancies, and gaining a deeper understanding of this phenomenon is a priority.

Throughout this thesis, a fundamental insight was that designing such a device demands specialized knowledge of each component and aspect of the system. Each of these components has the potential for further optimization. Therefore, enhancements in every section through comprehensive further analysis are a promising avenue for future research and improvement.

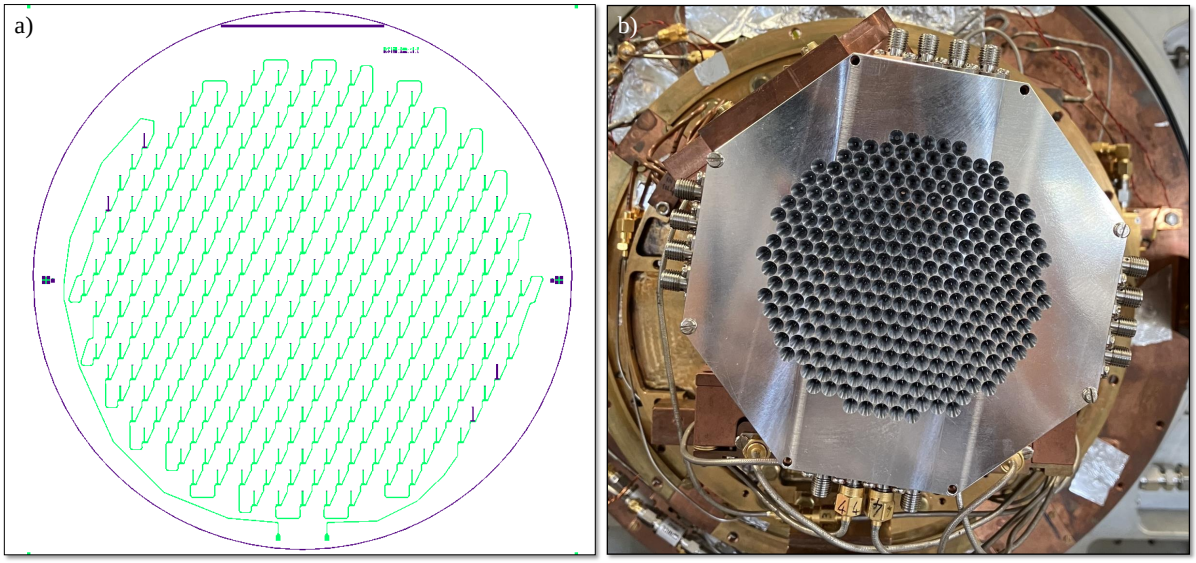

Figure 10.1: HYPKID for 2 mm atmospheric band: (a) The design with 300 channels. (b) The horn-waveguide set-up

Appendix A

Appendix

A.1 Microstrip line

The properties of a planar structure are determined by the dimensions of a single plane. One widely used planar structure for microwave integrated circuits is the microstrip line due to its simplicity. The microstrip consists of a rectangular metal strip of width w_{ms} placed on a grounded dielectric of relative permittivity ε_r and thickness h_d, as depicted in Fig. A.1.

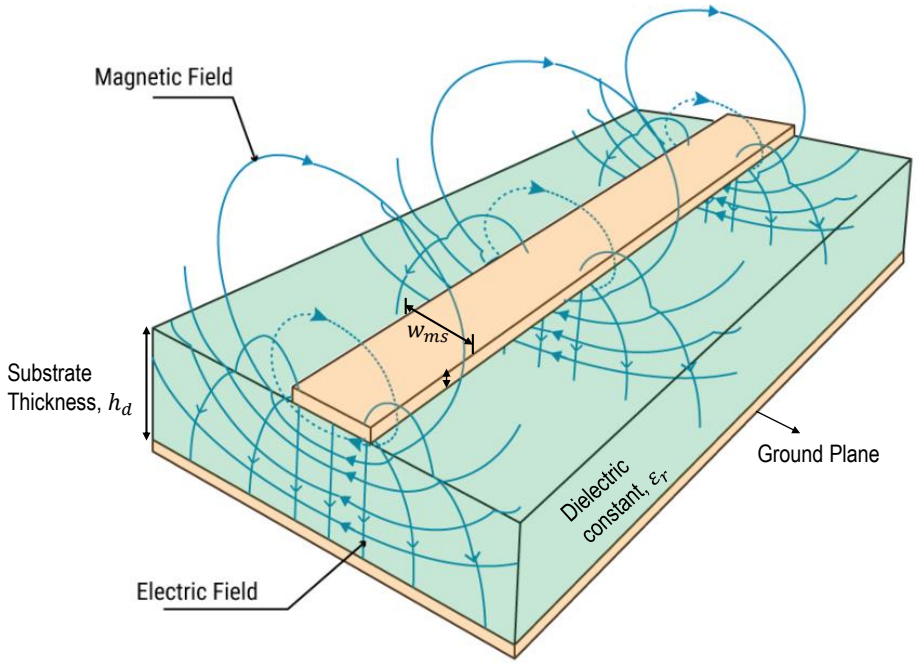

Figure A.1: Electromagnetic fields in a microtrip line of width, w_ms on a substrate with dieletric constant, ε_r and thickness, h_d, taken from *Sierra circuits, Inc.*

Considering the microstrip line and the ground plane as two conductor transmission line with a dielectric in between, the transverse electromagnetic (TEM) mode describes how signals or waves travel along. In this mode, the electric and magnetic fields associated with the signal are perpendicular to the direction in which the wave moves along the microstrip line. However, as the microstrip is a narrow line placed on a much wider ground plane, the line exhibits quasi-TEM propagation modes with fringing fields at the interface. The analysis of the microstrip line

relies on quasi-static methods, assuming pure TEM propagation and making certain parameter approximations afterwards.
The wavelength propagating in the microstrip, called the guided wavelength (λ_g), differs from the vacuum wavelength (λ). It can be expressed as:

$$\lambda_g = \frac{c}{f\sqrt{\varepsilon_{eff}}} \tag{A.1}$$

where c is the speed of light, f is the frequency, and ε_{eff} is the effective dielectric constant of the microstrip line. The value of ε_{eff} is approximated based on the dielectric thickness and the width of the microstrip. For narrow strips ($w_{ms}/h_d \ll 2$), ε_{eff} can be determined using the following expression:

$$\varepsilon_{eff} = \frac{\varepsilon_r + 1}{2} + \frac{\varepsilon_r - 1}{2}\frac{\ln(\pi/2) + (1/\varepsilon_r)\ln(4/\pi)}{\ln(8h_d/w_{ms})} \tag{A.2}$$

It's important to note that the effective dielectric constant (ε_{eff}) is generally less than the relative dielectric constant (ε_r), falling within the range $1 < \varepsilon_{eff} < \varepsilon_r$.
The intrinsic impedance of free space is approximately 377 Ω. When transitioning between vacuum and any component, the impedance must be taken into consideration to avoid impedance mismatch, which can adversely affect device behaviour.
The characteristic impedance of a microstrip line depends on its width, dielectric constant, and substrate thickness. Various approximations exist for calculating the characteristic impedance based on the strip width to substrate height ratio (w_{ms}/h_d), and these are extensively discussed in [Pozar, 2005] [Garg et al., 2013]. The simplified formula usually used is,

$$\begin{aligned} Z_0 &= \frac{60}{\sqrt{\varepsilon_{eff}}}\ln\left(\frac{8h_d}{w_{ms}} + \frac{w_{ms}}{4h_d}\right) \qquad w_{ms}/h_d \leq 1 \\ &= \frac{120\pi}{\sqrt{\varepsilon_{eff}[\frac{w_{ms}}{h_d} + 1.393 + 0.667\ln(\frac{w_{ms}}{h_d} + 1.444)]}} \qquad w_{ms}/h_d \geq 1 \end{aligned} \tag{A.3}$$

For an accurate evaluation of microstrip properties, non-TEM parameters must be considered, providing the dispersion behaviour of the effective dielectric constant and characteristic impedance as a function of frequency. However, within the frequency range of interest (1-2 GHz with 200 MHz band for the readout line and 30 GHz band with 75-110 GHz frequency range for direct detection), calculations show that ε_{eff} and Z_0 (characteristic impedance) remain relatively constant.
Microstrip lines exhibit two sources of attenuation: conductor loss and dielectric loss. Conductor loss is the ratio of power loss in the conductor to the transmitted power and is determined by the series surface resistance (R) per unit length and the total inductance (L) per unit length. In the case of superconducting microstrip lines, resistive losses are nearly zero due to superconductivity, resulting in negligible conductor loss.
Dielectric loss, on the other hand, is independent of the line's geometry and can be managed using low-loss dielectric materials. Materials like sapphire or silicon monocrystalline substrates at very low temperatures have relatively low but not insignificant dielectric losses. However, in this thesis, the focus is on the spectral behaviour of the device rather than an in-depth study

of losses.
The maximum operational frequency of a microstrip is constrained by several factors, including the excitation of undesirable spurious modes, increased losses, notable effects of signal disruptions, low quality factor (Q) due to radiation from discontinuities, pulse distortion from dispersion, stringent fabrication tolerances, susceptibility to handling damage, and technological limitations.
The frequency at which significant coupling occurs between the quasi-TEM mode and the lowest-order surface wave spurious mode can be calculated using the following formula:

$$f_T[\text{ in GHz}] = \frac{150}{\pi h_{ms}[\text{in mm}]}\sqrt{\frac{2}{\varepsilon_r - 1}}\tan^{-1}(\varepsilon_r) \tag{A.4}$$

To avoid the excitation of higher-order modes in a microstrip, it should be operated below the cut-off frequency of the first higher-order mode, approximately given by:

$$f_{c1}[\text{ in GHz}] = \frac{300}{\sqrt{\epsilon_r}(2w_{ms}[\text{in mm}] + 0.8h_{ms}[\text{in mm}])} \tag{A.5}$$

In an infinitely long microstrip, no radiation occurs because there is no coupling between the dominant mode and higher-order radiating modes. However, when there is a discontinuity in the line, such as an open end, slit, change in width, bend, or gap, higher-order radiating modes are excited, depending on the substrate thickness and frequency of operation.
Furthermore, the dielectric thickness of the microstrip is much smaller than the wavelength of the signals it carries ($h_d \ll \lambda$). Also, the ground plane is thick superconducting layer compared to the microstrip line for taking advantage of the superconducting properties. In summary, the microstrip line's characteristics are influenced by its geometrical parameters and dielectric properties, with important implications for its impedance, wavelength, and frequency limitations. Now we will introduce various properties of the superconductors which will take us into the kinetic inductance detectors and $\lambda/2$ resonators using microstrip properties.

A.2 Components of a LEKID

Meander Inductors For LEKIDs, thin long conducting wires are meandered is such a way that leads to even distribution of current across the inductor. For specific applications, the meander acts as the direct light absorber, therefore, regardless of the position of a pair breaking event in the circuit, the resultant shift in the resonant frequency stays consistent.
The total inductance of the inductor is composed of two types of inductance, the geometric inductance (L_g), which depends on how the meanders are designed and the kinetic inductance(L_k), which depends on the material properties. The geometrical inductance of the meander-shaped inductance is well described in [Chen et al., 2023]. The total geometrical inductance of the meander is due to the effect of the self-inductance of each line and the mutual inductance between the parallel lines. Taking account of the uniform distribution of the current and neglecting the skin effect, the self inductance for a metal strip of length l, width w and thickness t can be formulated as,

$$L_{self} = \frac{\mu_0 l}{2\pi}\left[ln\left(\frac{2l}{w+t} + \frac{1}{2} + \frac{w+t}{3l}\right)\right] \tag{A.6}$$

The mutual inductance between two metal strips are calculated with the formula,

$$L_m(l,s) = \pm\frac{\mu_0 l}{2\pi}Q(l,s) \tag{A.7}$$

where

$$Q(l,s) = ln\left[1+\sqrt{1+\left(\frac{s}{l}\right)}-ln\left(\frac{s}{l}\right)+\left[\frac{s}{l}-\sqrt{1+(\left(\frac{s}{l}\right)^2}\right]\right] \tag{A.8}$$

for s is the geometrical mean distance between two strips or pitch distance. If the meander is formed with N number of lines,

$$L^t_{self} = NL_s(w+s)+(N+1)L_s(l) \tag{A.9}$$

$$L^t_{mutual} = 2\sum_{n=1}^{N}(N+1-n)L_m[l,n(w+s)] \tag{A.10}$$

The total geometrical inductance value is given by,

$$L_g = L^t_{self} + L^t_{mutual} \tag{A.11}$$

The kinetic inductance of the meander lines is related to the normal sheet resistance, R_n of the superconducting material and ρ_n is the normal resistivity of nano strip and given by Mattis Bardeen formula. In general expression, it can be given by [Mawatari, 2023],

$$L_k = \mu_0\lambda^2\frac{R_n}{\rho_n} = \frac{\mu_0\lambda^2}{d}(\frac{l_0}{w}+\alpha_c) \tag{A.12}$$

where the correction factor α_c arises from the effect of turns.

Interdigitated Capacitors The interdigitated capacitor is made of a comb of superconducting thin strips of thickness h, combed with each other on a dielectric of thickness t. The length of each strip, called the finger is l_c and the finger width and the gap width, w_c. If the number of fingers is N and the total width of the IDC is W_c, the total capacitance is calculated using conformal mapping technique,

$$C = (N-3)\frac{C_1C_2}{C_1+C_2}+2C_E \qquad [\text{F}] \tag{A.13}$$

where C_1 and C_2 are the capacitances between interior fingers and C_E is defined as the capacitance between the interior finger and exterior finger in each unit cell. All these parameters are well-described and taken from [Chen et al., 2023].

A.3 Four Wire Resistance measurement

A precise measurement of the resistivity is essential to monitor the onset of the superconductivity. The superconductor has zero dc resistance below the transition temperature. The standard

two wires resistance measurement technique is not suitable for low resistivity of thin films because of the finite resistance of the soldered contacts and the readout wires. To correct such effects, we measure the resistance using a four wire readout method. As shown in Fig.A.2, the current (I_A) is applied to two external wires (C1 and C2) and the voltage is measured across a separate pair (P1 and P2).

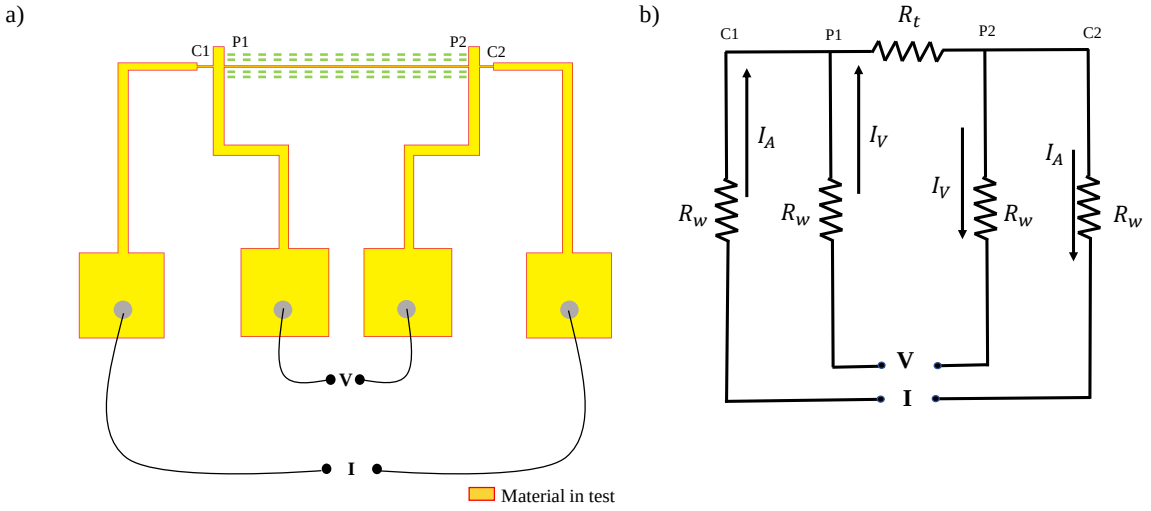

Figure A.2: Four Wire Measurement: (a) The measurement chip used. The current (I) is applied between the two current probes (C1 and C2). The voltage (V) is taken in between the potential probes (P1 and P2). The grey circles are the micro-bonds of the Al wires connecting the material under test and the wires of the dilution refrigerator. (b) The equivalent circuit. R_t is the resistance of the material (in this case, the wire of the thin film, highlighted in green) and R_w is the resistance of the measurement wires including the contact resistance and any parasitic component. I_A is the current sent into the circuit via current probes and I_V is the small current circulating in the voltage measurement branch.

The voltage and current probes are connected to the square pads used for micro-bonding. The equivalent circuit is shown in Fig. A.2(b). Applying the Kirchoff's law to the voltage probe loop, it can be shown that the voltage measured is,

$$V = I_A R_t + I_V(R_t + 2R_w) \tag{A.14}$$

where R_t is the resistance of the material, R_w is the resistance of the measurement wires including the contact resistance and any parasitic component, I_A is the current sent into the

circuit via current probes and I_V is the current circulating in the voltage measurement branch. The current across the voltage probe (I_V)is much smaller than the bias current, I_A and its contribution can be neglected. Therefore, we can measure the resistance of the test material (R_t) as following,

$$R_t = \frac{V}{I_A} \tag{A.15}$$

When measuring the voltage, an off-set component is usually observed due to the thermally induced voltages appearing at the junctions between dissimilar materials (Seebeck's effect). To cope with this offset, the measurement are carried out using an ac current. The voltage measured applying a positive current will be:

$$V^+ = I_A^+ R_t + V_{offset} \tag{A.16}$$

While when the current is negative,

$$V^- = I_A^- R_t + V_{offset} = -I_A^+ R_t + V_{offset} \tag{A.17}$$

By calculating the difference of the two measurements, we get,

$$R_t = \frac{(V^+ + V^-)}{2I_A^+} \tag{A.18}$$

We operate our lock-in and amplifier with AC current about 100 Hz.
In this method, the resistance is measured for the section of the wire highlighted in green. As the length (l), width (w) , and thickness (d) is known, we calculate the resistance per square for the wire and resistivity ($\rho = R \times \frac{dw}{l} = R$ (in per $\square$) $\times d$) where $\square = \frac{l}{w}$.

Bibliography

Adam, R., Adane, A., Ade, P. A. R., André, P., Andrianasolo, A., Aussel, H., Beelen, A., Benoît, A., Bideaud, A., Billot, N., Bourrion, O., Bracco, A., Calvo, M., Catalano, A., Coiffard, G., Comis, B., De Petris, M., Désert, F.-X., Doyle, S., Driessen, E. F. C., Evans, R., Goupy, J., Kramer, C., Lagache, G., Leclercq, S., Leggeri, J.-P., Lestrade, J.-F., Macías-Pérez, J. F., Mauskopf, P., Mayet, F., Maury, A., Monfardini, A., Navarro, S., Pascale, E., Perotto, L., Pisano, G., Ponthieu, N., Revéret, V., Rigby, A., Ritacco, A., Romero, C., Roussel, H., Ruppin, F., Schuster, K., Sievers, A., Triqueneaux, S., Tucker, C., and Zylka, R. The nika2 large-field-of-view millimetre continuum camera for the 30 m iram telescope. *A&A*, 609:A115, 2018. doi: 10.1051/0004-6361/201731503. URL `https://doi.org/10.1051/0004-6361/201731503`.

N Aghanim, Mark Ashdown, J Aumont, C Baccigalupi, M Ballardini, AJ Banday, RB Barreiro, N Bartolo, Suman Basak, K Benabed, et al. Planck intermediate results-xlviii. disentangling galactic dust emission and cosmic infrared background anisotropies. *Astronomy & Astrophysics*, 596:A109, 2016.

B Aja, L De La Fuente, A Fernandez, Juan P Pascual, E Artal, MC De Ory, MT Magaz, Daniel Granados, J Martin-Pintado, and A Gomez. Bi-layer kinetic inductance detectors for w-band. In *2020 IEEE/MTT-S International Microwave Symposium (IMS)*, pages 932–935. IEEE, 2020.

N.W. Ashcroft and N.D. Mermin. *Solid State Physics*. HRW international editions. Holt, Rinehart and Winston, 1976. ISBN 9780030839931. URL `https://books.google.fr/books?id=oXIfAQAAMAAJ`.

Constantine A Balanis. *Antenna theory: analysis and design*. Wiley-Interscience, 2005.

J. Bardeen, L. N. Cooper, and J. R. Schrieffer. Theory of superconductivity. *Phys. Rev.*, 108: 1175–1204, Dec 1957. doi: 10.1103/PhysRev.108.1175. URL `https://link.aps.org/doi/10.1103/PhysRev.108.1175`.

John Bardeen. Two-fluid model of superconductivity. *Physical Review Letters*, 1(11):399, 1958.

M Bethermin, A Gkogkou, M Van Cuyck, G Lagache, A Beelen, M Aravena, A Benoit, J Bounmy, M Calvo, A Catalano, et al. Concerto: High-fidelity simulation of millimeter line emissions of galaxies and [cii] intensity mapping. *Astronomy & Astrophysics*, 667:A156, 2022.

A. W. Blain and M. S. Longair. Submillimetre cosmology. *Monthly Notices of the Royal Astronomical Society*, 264(2):509–521, 09 1993. ISSN 0035-8711. doi: 10.1093/mnras/264.2.509. URL `https://doi.org/10.1093/mnras/264.2.509`.

O Bourrion, C Vescovi, JL Bouly, Alain Benoit, M Calvo, L Gallin-Martel, JF Macias-Perez, and Alessandro Monfardini. Nikel: Electronics and data acquisition for kilopixels kinetic inductance camera. *Journal of Instrumentation*, 7(07):P07014, 2012.

G Brammertz, A Poelaert, Alexandre Avraamovitch Golubov, P Verhoeve, A Peacock, and Horst Rogalla. Generalized proximity effect model in superconducting bi-and trilayer films. *Journal of Applied Physics*, 90(1):355–364, 2001.

Sean Bryan, James Aguirre, George Che, Simon Doyle, Daniel Flanigan, Christopher Groppi, Bradley Johnson, Glenn Jones, Philip Mauskopf, Heather McCarrick, Alessandro Monfardini, and Tony Mroczkowski. WSPEC: A waveguide filter-bank focal plane array spectrometer for millimeter wave astronomy and cosmology. *Journal of Low Temperature Physics*, 184(1-2):114–122, dec 2015. doi: 10.1007/s10909-015-1396-5. URL https://doi.org/10.1007%2Fs10909-015-1396-5.

Sean Bryan, Jason Austermann, Daniel Ferrusca, Philip Mauskopf, Jeff McMahon, Alfredo Montaña, Sara Simon, Giles Novak, David Sánchez-Argüelles, and Grant Wilson. Optical design of the toltec millimeter-wave camera. In *Millimeter, Submillimeter, and Far-Infrared Detectors and Instrumentation for Astronomy IX*, volume 10708, pages 48–55. SPIE, 2018.

Bruno T Buijtendorp, Juan Bueno, David J Thoen, Vignesh Murugesan, Paolo M Sberna, Jochem JA Baselmans, Sten Vollebregt, and Akira Endo. Characterization of low-loss hydrogenated amorphous silicon films for superconducting resonators. *Journal of Astronomical Telescopes, Instruments, and Systems*, 8(2):028006–028006, 2022a.

B.T. Buijtendorp, S. Vollebregt, K. Karatsu, D.J. Thoen, V. Murugesan, K. Kouwenhoven, S. Hähnle, J.J.A. Baselmans, and A. Endo. Hydrogenated amorphous silicon carbide: A low-loss deposited dielectric for microwave to submillimeter-wave superconducting circuits. *Phys. Rev. Appl.*, 18:064003, Dec 2022b. doi: 10.1103/PhysRevApplied.18.064003. URL https://link.aps.org/doi/10.1103/PhysRevApplied.18.064003.

M Carter, B Lazareff, D Maier, J-Y Chenu, A-L Fontana, Y Bortolotti, C Boucher, A Navarrini, S Blanchet, A Greve, et al. The emir multi-band mm-wave receiver for the iram 30-m telescope. *Astronomy & Astrophysics*, 538:A89, 2012.

A Catalano, J Goupy, Hélène Le Sueur, A Benoit, O Bourrion, M Calvo, A D?addabbo, L Dumoulin, F Levy-Bertrand, J Macías-Pérez, et al. Bi-layer kinetic inductance detectors for space observations between 80–120 ghz. *Astronomy & Astrophysics*, 580:A15, 2015.

T Cecil, C Albert, AJ Anderson, PS Barry, B Benson, C Cotter, C Chang, M Dobbs, K Dibert, R Gualtieri, et al. Fabrication development for spt-slim, a superconducting spectrometer for line intensity mapping. *IEEE Transactions on Applied Superconductivity*, 33(5):1–6, 2023.

Qi-Ming Chen, Priyank Singh, Rostislav Duda, Giacomo Catto, Aarne Keränen, Arman Alizadeh, Timm Mörstedt, Aashish Sah, András Gunyhó, Wei Liu, et al. Compact inductor-capacitor resonators at sub-gigahertz frequencies. *arXiv preprint arXiv:2304.12744*, 2023.

U Chowdhury, M Calvo, J Goupy, F Levy-Bertrand, and A Monfardini. A millimetre-wave superconducting hyper-spectral device. *RAS Techniques and Instruments*, 2(1):562–566, 08 2023. ISSN 2752-8200. doi: 10.1093/rasti/rzad038. URL https://doi.org/10.1093/rasti/rzad038.

Chowdhury, U., Levy-Bertrand, F., Calvo, M., Goupy, J., and Monfardini, A. A horn-coupled millimetre-wave on-chip spectrometer based on lumped-element kinetic inductance detectors. *A&A*, 672:A7, 2023. doi: 10.1051/0004-6361/202244887. URL `https://doi.org/10.1051/0004-6361/202244887`.

PN Chubov, VV Eremenko, and Yu A Pilipenko. Dependence of the critical temperature and energy gap on the thickness of superconducting aluminum films. *SOV PHYS JETP*, 28(3): 389–395, 1969.

Leon N. Cooper. Bound electron pairs in a degenerate fermi gas. *Phys. Rev.*, 104:1189–1190, Nov 1956. doi: 10.1103/PhysRev.104.1189. URL `https://link.aps.org/doi/10.1103/PhysRev.104.1189`.

AT Crites, JJ Bock, CM Bradford, TC Chang, AR Cooray, L Duband, Y Gong, S Hailey-Dunsheath, J Hunacek, PM Koch, et al. The time-pilot intensity mapping experiment. In *Millimeter, submillimeter, and far-infrared detectors and instrumentation for astronomy VII*, volume 9153, pages 613–621. SPIE, 2014.

CST. Cst microwave studio advanced topics. Technical report, CST-Computer Simulation Technology, 2002.

Peter K Day, Henry G LeDuc, Benjamin A Mazin, Anastasios Vayonakis, and Jonas Zmuidzinas. A broadband superconducting detector suitable for use in large arrays. *Nature*, 425(6960): 817–821, 2003.

PJ De Visser, JJA Baselmans, P Diener, SJC Yates, A Endo, and TM Klapwijk. Generation-recombination noise: The fundamental sensitivity limit for kinetic inductance detectors. *Journal of Low Temperature Physics*, 167:335–340, 2012.

SR Dicker, PAR Ade, J Aguirre, JA Brevik, HM Cho, R Datta, MJ Devlin, B Dober, D Egan, J Ford, et al. Mustang 2: a large focal plane array for the 100 m green bank telescope. *Journal of Low Temperature Physics*, 176(5):808–814, 2014.

P Diener, H Schellevis, and JJA Baselmans. Homogeneous superconducting phase in tin film: A complex impedance study. *Applied Physics Letters*, 101(25), 2012.

Simon Doyle, Philip Mauskopf, J Naylon, Adrian Porch, and C Duncombe. Lumped element kinetic inductance detectors. *Journal of Low Temperature Physics*, 151:530–536, 2008.

Thomas Durand. *Réalisation d'un interféromètre de Martin-Puplett pour le développement d'une caméra bolométrique.* PhD thesis, Université Joseph-Fourier-Grenoble I, 2007.

G Ejlali, R Adam, P Ade, H Ajeddig, P André, E Artis, H Aussel, A Beelen, A Benoît, S Berta, et al. Dust emission in galaxies at millimeter wavelengths: Cooling of star forming regions in ngc6946. In *EPJ Web of Conferences*, volume 257, page 00016. EDP Sciences, 2022.

Sonnet em. Sonnet electromagnetic simulator (17.56).

Akira Endo, Kenichi Karatsu, Yoichi Tamura, Tai Oshima, Akio Taniguchi, Tatsuya Takekoshi, Shinichiro Asayama, Tom J. L. C. Bakx, Sjoerd Bosma, Juan Bueno, Kah Wuy Chin, Yasunori Fujii, Kazuyuki Fujita, Robert Huiting, Soh Ikarashi, Tsuyoshi Ishida, Shun Ishii, Ryohei Kawabe, Teun M. Klapwijk, Kotaro Kohno, Akira Kouchi, Nuria Llombart, Jun Maekawa, Vignesh Murugesan, Shun ichi Nakatsubo, Masato Naruse, Kazushige Ohtawara, Alejandro Pascual Laguna, Junya Suzuki, Koyo Suzuki, David J. Thoen, Takashi Tsukagoshi, Tetsutaro Ueda, Pieter J. de Visser, Paul P. van der Werf, Stephen J. C. Yates, Yuki Yoshimura, Ozan Yurduseven, and Jochem J. A. Baselmans. First light demonstration of the integrated superconducting spectrometer. *Nature Astronomy*, 2019.

Akira Endo, Kenichi Karatsu, Yoichi Tamura, Tai Oshima, Akio Taniguchi, Tatsuya Takekoshi, Shin'ichiro Asayama, Tom J. L. C. Bakx, Sjoerd Bosma, Juan Bueno, Kah Wuy Chin, Yasunori Fujii, Kazuyuki Fujita, Robert Huiting, Soh Ikarashi, Tsuyoshi Ishida, Shun Ishii, Ryohei Kawabe, Teun M. Klapwijk, Kotaro Kohno, Akira Kouchi, Nuria Llombart, Jun Maekawa, Vignesh Murugesan, Shunichi Nakatsubo, Masato Naruse, Kazushige Ohtawara, Alejandro Pascual Laguna, Junya Suzuki, Koyo Suzuki, David J. Thoen, Takashi Tsukagoshi, Tetsutaro Ueda, Pieter J. de Visser, Paul P. van der Werf, Stephen J. C. Yates, Yuki Yoshimura, Ozan Yurduseven, and Jochem J. A. Baselmans. First light demonstration of the integrated superconducting spectrometer. *Nature Astronomy*, 3:989–996, August 2019. doi: 10.1038/s41550-019-0850-8.

Hanno Essén and Miguel CN Fiolhais. Meissner effect, diamagnetism, and classical physics?a review. *American Journal of Physics*, 80(2):164–169, 2012.

DJ Fixsen. The temperature of the cosmic microwave background. *The Astrophysical Journal*, 707(2):916, 2009.

Daniel Flanigan. *Kinetic inductance detectors for measuring the polarization of the cosmic microwave background*. Columbia University, 2018.

Ramesh Garg, Inder Bahl, and Maurizio Bozzi. *Microstrip lines and slotlines*. Artech house, 2013.

A. R. Gillespie. CO Observations in Galactic Clouds. *The Messenger*, 21:20, September 1980.

Adam Ginsburg, Jason Glenn, Erik Rosolowsky, Timothy P Ellsworth-Bowers, Cara Battersby, Miranda Dunham, Manuel Merello, Yancy Shirley, John Bally, Neal J Evans II, et al. The bolocam galactic plane survey. ix. data release 2 and outer galaxy extension. *The Astrophysical Journal Supplement Series*, 208(2):14, 2013.

RE Glover III and M Tinkham. Transmission of superconducting films at millimeter-microwave and far infrared frequencies. *Physical Review*, 104(3):844, 1956.

Eric Herbst. The chemistry of interstellar space. *Chem. Soc. Rev.*, 30:168–176, 2001. doi: 10.1039/A909040A. URL `http://dx.doi.org/10.1039/A909040A`.

Paul TP Ho, James M Moran, and Kwok Yung Lo. The submillimeter array. *The Astrophysical Journal*, 616(1):L1, 2004.

WS Holland, D Bintley, EL Chapin, Antonio Chrysostomou, GR Davis, JT Dempsey, WD Duncan, M Fich, P Friberg, M Halpern, et al. Scuba-2: the 10 000 pixel bolometer camera on the james clerk maxwell telescope. *Monthly Notices of the Royal Astronomical Society*, 430 (4):2513–2533, 2013.

Amber Hornsby. *Development of microstrip-coupled Lumped-Element Kinetic Inductance Detectors for astronomy*. PhD thesis, Cardiff University, 2020.

Yuh-Jing Hwang, Chau-Ching Chiong, Yau-De Huang, Chi-Den Huang, Ching-Tang Liu, Yue-Fang Kuo, Shou-Hsien Weng, Chin-Ting Ho, Po-Han Chiang, Hsiao-Ling Wu, et al. Band-1 receiver front-end cartridges for atacama large millimeter/submillimeter array (alma): design and development toward production. In *Millimeter, Submillimeter, and Far-Infrared Detectors and Instrumentation for Astronomy VIII*, volume 9914, pages 462–473. SPIE, 2016.

Steven B Kaplan, CC Chi, DN Langenberg, Jhy-Jiun Chang, S Jafarey, and DJ Scalapino. Quasiparticle and phonon lifetimes in superconductors. *Physical Review B*, 14(11):4854, 1976.

K. S. Karkare, P. S. Barry, C. M. Bradford, S. Chapman, S. Doyle, J. Glenn, S. Gordon, S. Hailey-Dunsheath, R. M. J. Janssen, A. Kovács, H. G. LeDuc, P. Mauskopf, R. McGeehan, J. Redford, E. Shirokoff, C. Tucker, J. Wheeler, and J. Zmuidzinas. Full-Array Noise Performance of Deployment-Grade SuperSpec mm-Wave On-Chip Spectrometers. *Journal of Low Temperature Physics*, 199(3-4):849–857, February 2020. doi: 10.1007/s10909-020-02407-4.

K. S. Karkare, A. J. Anderson, P. S. Barry, B. A. Benson, J. E. Carlstrom, T. Cecil, C. L. Chang, M. A. Dobbs, M. Hollister, G. K. Keating, D. P. Marrone, J. McMahon, J. Montgomery, Z. Pan, G. Robson, M. Rouble, E. Shirokoff, and G. Smecher. Spt-slim: A line intensity mapping pathfinder for the south pole telescope. *Journal of Low Temperature Physics 2022*, pages 1–8, 3 2022. ISSN 1573-7357. doi: 10.1007/S10909-022-02702-2. URL `https://link.springer.com/article/10.1007/s10909-022-02702-2`.

Katsioli, S., Adam, R., Ade, P., Ajeddig, H., André, P., Artis, E., Aussel, H., Beelen, A., Benoît, A., Berta, S., Bing, L., Bourrion, O., Calvo, M., Catalano, A., De Looze, I., De Petris, M., Désert, F.-X., Doyle, S., Driessen, E.F. C., Ejlali, G., Galametz, M., Galliano, F., Gomez, A., Goupy, J., Jones, A.P., Hughes, A., Kéruzoré, F., Kramer, C., Ladjelate, B., Lagache, G., Leclercq, S., Lestrade, J.-F., Macías-Pérez, J.-F., Madden, S.C., Maury, A., Mauskopf, P., Mayet, F., Monfardini, A., Muñoz-Echeverría, M., Nersesian, A., Perotto, L., Pisano, G., Ponthieu, N., Revéret, V., Rigby, A.J., Ritacco, A., Romero, C., Roussel, H., Ruppin, F., Schuster, K., Shu, S., Sievers, A., Smith, M. W. L., Tabatabaei, F., Tucker, C., Xilouris, E. M., and Zylka, R. Exploring the millimetre emission in nearby galaxies: Analysis of the edge-on galaxy ngc 891. *EPJ Web Conf.*, 257:00023, 2022. doi: 10.1051/epjconf/202225700023. URL `https://doi.org/10.1051/epjconf/202225700023`.

Richard L Kautz. Picosecond pulses on superconducting striplines. *Journal of Applied Physics*, 49(1):308–314, 1978.

Ely D Kovetz, Marco P Viero, Adam Lidz, Laura Newburgh, Mubdi Rahman, Eric Switzer, Marc Kamionkowski, James Aguirre, Marcelo Alvarez, James Bock, et al. Line-intensity mapping: 2017 status report. *arXiv preprint arXiv:1709.09066*, 2017.

M Yu Kuprianov and VF Lukichev. Influence of boundary transparency on the critical current of ?dirty? ss?s structures. *Zh. Eksp. Teor. Fiz*, 94(6):139–149, 1988.

Guilaine Lagache, Jean-Loup Puget, and Hervé Dole. Dusty infrared galaxies: Sources of the cosmic infrared background. *Annual Review of Astronomy and Astrophysics*, 43(1):727–768, 2005. doi: 10.1146/annurev.astro.43.072103.150606. URL `https://doi.org/10.1146/annurev.astro.43.072103.150606`.

Guilaine Lagache, Morgane Cousin, and Marios Chatzikos. The [cii] 158 μm line emission in high-redshift galaxies. *Astronomy & Astrophysics*, 609:A130, 2018.

A Pascual Laguna. On-chip solutions for future thz imaging spectrometers. 2022.

J-F Lestrade, R Adam, P Ade, H Ajeddig, P Andre, E Artis, H Aussel, A Beelen, A Benoit, S Berta, et al. Overdensity of submillimiter galaxies in the gj526 field mapped with the nika2 camera. In *EPJ Web of Conferences*, volume 257, page 00027. EDP Sciences, 2022.

William A. Little. Decay of persistent currents in small superconductors. *Phys. Rev.*, 156: 396–403, Apr 1967. doi: 10.1103/PhysRev.156.396. URL `https://link.aps.org/doi/10.1103/PhysRev.156.396`.

B Magnelli, A Karim, J Staguhn, A Kovács, EF Jiménez-Andrade, CM Casey, JA Zavala, E Schinnerer, M Sargent, M Aravena, et al. The iram/gismo 2 mm survey in the cosmos field? *The Astrophysical Journal*, 877(1):45, 2019.

Maiolino, R., Nagao, T., Grazian, A., Cocchia, F., Marconi, A., Mannucci, F., Cimatti, A., Pipino, A., Ballero, S., Calura, F., Chiappini, C., Fontana, A., Granato, G. L., Matteucci, F., Pastorini, G., Pentericci, L., Risaliti, G., Salvati, M., and Silva, L. Amaze* - i. the evolution of the mass-metallicity relation at z. *A&A*, 488(2):463–479, 2008. doi: 10.1051/0004-6361:200809678. URL `https://doi.org/10.1051/0004-6361:200809678`.

Nataliya Maleeva, Lukas Grünhaupt, T Klein, F Levy-Bertrand, O Dupre, M Calvo, F Valenti, P Winkel, F Friedrich, W Wernsdorfer, et al. Circuit quantum electrodynamics of granular aluminum resonators. *Nature communications*, 9(1):3889, 2018.

DH Martin and E Puplett. Polarised interferometric spectrometry for the millimetre and submillimetre spectrum. *Infrared Physics*, 10(2):105–109, 1970.

D. C. Mattis and J. Bardeen. Theory of the anomalous skin effect in normal and superconducting metals. *Phys. Rev.*, 111:412–417, Jul 1958. doi: 10.1103/PhysRev.111.412. URL `https://link.aps.org/doi/10.1103/PhysRev.111.412`.

PD Mauskopf. Transition edge sensors and kinetic inductance detectors in astronomical instruments. *Publications of the Astronomical Society of the Pacific*, 130(990):082001, 2018.

Yasunori Mawatari. Kinetic inductance of superconducting nanostrips with turns. *Journal of Applied Physics*, 133(17), 2023.

Benjamin A Mazin. *Microwave kinetic inductance detectors*. California Institute of Technology, 2005.

H McCarrick, D Flanigan, G Jones, BR Johnson, P Ade, D Araujo, K Bradford, R Cantor, G Che, P Day, et al. Horn-coupled, commercially-fabricated aluminum lumped-element kinetic inductance detectors for millimeter wavelengths. *Review of Scientific Instruments*, 85 (12), 2014.

Robert Meservey and Paul M Tedrow. Measurements of the kinetic inductance of superconducting linear structures. *Journal of Applied Physics*, 40(5):2028–2034, 1969.

A Misiriotis, EM Xilouris, J Papamastorakis, P Boumis, and CD Goudis. The distribution of the ism in the milky way-a three-dimensional large-scale model. *Astronomy & Astrophysics*, 459(1):113–123, 2006.

Alessandro Monfardini and Guilaine Lagache. A magnum opus on the chajnantor plateau. *Nature Astronomy*, 5(9):970–970, 2021.

Alessandro Monfardini, Alain Benoit, Aurélien Bideaud, L Swenson, A Cruciani, P Camus, C Hoffmann, FX Désert, S Doyle, P Ade, et al. A dual-band millimeter-wave kinetic inductance camera for the iram 30 m telescope. *The Astrophysical Journal Supplement Series*, 194 (2):24, 2011.

R Neri, P Cox, A Omont, A Beelen, S Berta, T Bakx, M Lehnert, AJ Baker, V Buat, A Cooray, et al. Noema redshift measurements of bright herschel galaxies. *Astronomy & Astrophysics*, 635:A7, 2020.

Aaron D OConnell, M Ansmann, Radoslaw C Bialczak, Max Hofheinz, Nadav Katz, Erik Lucero, C McKenney, Matthew Neeley, Haohua Wang, Eva Maria Weig, et al. Microwave dielectric loss at single photon energies and millikelvin temperatures. *Applied Physics Letters*, 92(11), 2008.

Alain Omont, Alexandre Beelen, Frank Bertoldi, Pierre Cox, Chris L Carilli, Robert S Priddey, Richard G McMahon, and Kate G Isaak. A 1.2 mm mambo/iram–30 m study of dust emission from optically luminous 2 quasars. *A&A*, 398(3):857–865, 2003.

Heike Kamerlingh Onnes. *Through measurement to knowledge: The selected papers of Heike Kamerlingh Onnes 1853–1926*, volume 124. Springer Science & Business Media, 2012.

Robert O'Rourke. 3d electromagnetic simulation vs. planar mom. *Microwave Journal*, 58(7), 2015.

A Paiella, A Coppolecchia, MG Castellano, I Colantoni, A Cruciani, A D?Addabbo, P de Bernardis, S Masi, and G Presta. Development of lumped element kinetic inductance detectors for the w-band. *Journal of Low Temperature Physics*, 184(1-2):97–102, 2016.

Alfred Brian Pippard and William Lawrence Bragg. An experimental and theoretical study of the relation between magnetic field and current in a superconductor. *Proceedings of the Royal Society of London. Series A. Mathematical and Physical Sciences*, 216(1127):547–568, 1953.

David M Pozar. *Microwave engineering; 3rd ed.* Wiley, Hoboken, NJ, 2005. URL `https://cds.cern.ch/record/882338`.

Uwe S Pracht, Eric Heintze, Conrad Clauss, Daniel Hafner, Roman Bek, David Werner, Sergey Gelhorn, Marc Scheffler, Martin Dressel, Daniel Sherman, et al. Electrodynamics of the superconducting state in ultra-thin films at thz frequencies. *IEEE Transactions on Terahertz Science and Technology*, 3(3):269–280, 2013.

Ruslan Prozorov and Russell W Giannetta. Magnetic penetration depth in unconventional superconductors. *Superconductor Science and Technology*, 19(8):R41, 2006.

Vincent Revéret, Philippe André, Jean Le Pennec, Michel Talvard, Patrick Agnèse, Agnès Arnaud, Laurent Clerc, Carlos de Breuck, Jean-Charles Cigna, Cyrille Delisle, et al. The artémis wide-field sub-millimeter camera: preliminary on-sky performance at 350 microns. In *Millimeter, Submillimeter, and Far-Infrared Detectors and Instrumentation for Astronomy VII*, volume 9153, pages 75–85. SPIE, 2014.

G Siringo, E Kreysa, A Kovács, F Schuller, A Weiß, W Esch, H-P Gemünd, N Jethava, G Lundershausen, A Colin, et al. The large apex bolometer camera laboca. *Astronomy & Astrophysics*, 497(3):945–962, 2009.

Giorgio Siringo, Ernst Kreysa, Carlos De Breuck, Attila Kovacs, Andreas Lundgren, Frederic Schuller, Thomas Stanke, Axel Weiss, Rolf Guesten, Nikhil Jethava, et al. A new facility receiver on apex: the submillimetre apex bolometer camera, saboca. *The Messenger*, 139: 20–23, 2010.

George Smoot. Cosmic microwave background radiation anisotropies: their discovery and utilization. In *APS April Meeting Abstracts*, pages J5–002, 2007.

Gordon J Stacey, M Aravena, K Basu, N Battaglia, B Beringue, F Bertoldi, JR Bond, P Breysse, R Bustos, S Chapman, et al. Ccat-prime: science with an ultra-widefield submillimeter observatory on cerro chajnantor. In *Ground-based and airborne telescopes VII*, volume 10700, pages 482–501. SPIE, 2018.

AA Starobinskii. Spectrum of relict gravitational radiation and the early state of the universe. *JETP Letters*, 30(11):682–685, 1979.

M. C. Steele and R. A. Hein. Superconductivity of titanium. *Phys. Rev.*, 92:243–247, Oct 1953. doi: 10.1103/PhysRev.92.243. URL `https://link.aps.org/doi/10.1103/PhysRev.92.243`.

Katrin Steinberg, Marc Scheffler, and Martin Dressel. Quasi-particle dynamics in superconducting aluminum. *arXiv preprint arXiv:0712.3391*, 2007.

RA Sunyaev and Ya B Zel'Dovich. Microwave background radiation as a probe of the contemporary structure and history of the universe. *Annual review of astronomy and astrophysics*, 18(1):537–560, 1980.

Markus Thiemann, Martin Dressel, and Marc Scheffler. Complete electrodynamics of a bcs superconductor with μ ev energy scales: Microwave spectroscopy on titanium at mk temperatures. *Physical Review B*, 97(21):214516, 2018.

Michael Tinkham. Energy gap interpretation of experiments on infrared transmission through superconducting films. *Physical Review*, 104(3):845, 1956.

Michael Tinkham. *Introduction to Superconductivity*. Dover Publications, 2 edition, June 2004. ISBN 0486435032. URL `http://www.worldcat.org/isbn/0486435032`.

Carolyn G. Volpert, Emily M. Barrentine, Mona Mirzaei, Alyssa Barlis, Alberto D. Bolatto, Berhanu T. Bulcha, Giuseppe Cataldo, Jake A. Connors, Nicholas Costen, Negar Ehsan, Thomas Essinger-Hileman, Jason Glenn, James P. Hays-Wehle, Larry A. Hess, Alan J. Kogut, Harvey Moseley, Jonas Mugge-Durum, Omid Noroozian, Trevor M. Oxholm, Maryam Rahmani, Thomas Stevenson, Eric R. Switzer, Joeseph Watson, and Edward J. Wollack. Developing a new generation of integrated micro-spec far-infrared spectrometers for the experiment for cryogenic large-aperture intensity mapping (EXCLAIM). In Laura E. Coyle, Shuji Matsuura, and Marshall D. Perrin, editors, *Space Telescopes and Instrumentation 2022: Optical, Infrared, and Millimeter Wave*, volume 12180, page 121804Z. International Society for Optics and Photonics, SPIE, 2022. doi: 10.1117/12.2629502. URL `https://doi.org/10.1117/12.2629502`.

GW Wilson, JE Austermann, TA Perera, KS Scott, Peter AR Ade, JJ Bock, J Glenn, SR Golwala, S Kim, Y Kang, et al. The aztec mm-wavelength camera. *Monthly Notices of the Royal Astronomical Society*, 386(2):807–818, 2008.

Xiaolong Xu, Jinjin Li, Xueshen Wang, Qing Zhong, Yuan Zhong, Wenhui Cao, Wei Li, Jian Chen, Zhiwei Zhao, Ying Gao, et al. Investigation of superconducting titanium films for transition edge sensors. In *2020 Conference on Precision Electromagnetic Measurements (CPEM)*, pages 1–2. IEEE, 2020.

Songyuan Zhao, David J Goldie, Chris N Thomas, and Stafford Withington. Calculation and measurement of critical temperature in thin superconducting multilayers. *Superconductor Science and Technology*, 31(10):105004, 2018.

Songyuan Zhao, Stafford Withington, David J Goldie, and Chris N Thomas. Nonlinear properties of supercurrent-carrying single-and multi-layer thin-film superconductors. *Journal of Low Temperature Physics*, 199(1-2):34–44, 2020.

Jonas Zmuidzinas. Superconducting microresonators: Physics and applications. *Annu. Rev. Condens. Matter Phys.*, 3(1):169–214, 2012.

Abstract

In millimeter-wave astronomy, there is a need for innovative focal plane arrays that facilitate observations with low to medium spectral resolution and allow astronomers to identify a set of potentially interesting sources, such as high-redshift galaxies with moderate mapping speed. These spectrally-resolving arrays can also support the Line Intensity Mapping (LIM) technique, which can help researchers disentangle the emission lines as a function of redshift. To achieve the intermediate spectral resolution (i.e. 100-1000) while preserving the high sensitivity, there are recent developments in designing multiple on-chip spectrometers based on kinetic inductance detectors (*KIDs*) like DESHIMA, SuperSpec, μ-Spec, etc. In this thesis, we will discuss the simulation, design, fabrication, and optical characterization of focal-plane on-chip spectrometers of two different types, On-chip spectrometer using Microstrip based Kinetic Inductance Detector (*OMKID*)[1], and HYPer-spectral device with Kinetic Inductance Detector (*HYPKID*)[2], both are sensitive in the 75-110 GHz range. These are prototype designs where the incoming signal is split over different sub-bands using filters and each filter is capacitively coupled to a lumped-element kinetic inductance detector (*LEKID*) to identify the spectral responses. Both devices are designed based on microstrip configuration which provides the benefit of low loss, due to the mono-crystalline substrate. The prototype spectrometers exhibit a spectral resolution (R) of 200 - 1000. The optical noise equivalent power is around 10^-17 $W/\sqrt{Hz}$ which is in the range of an incoming power of pW per channel, confirming the gain in quantum efficiency as predicted by the electromagnetic simulations. This work affirms the reliability of both the proposed on-chip spectrometer designs while keeping an open possibility of significant improvement of the overall efficiency in future iterations of these devices.

Publications

1. U. Chowdhury, F. Levy-Bertrand, M. Calvo, J. Goupy and A. Monfardini, A horn-coupled millimetre-wave on-chip spectrometer based on lumped-element kinetic inductance detectors, A&A, 672 (2023) A7, DOI : https://doi.org/10.1051/0004-6361/202244887

2. U Chowdhury, M Calvo, J Goupy, F Levy-Bertrand, A Monfardini, A millimetre-wave superconducting hyper-spectral device, RAS Techniques and Instruments, Volume 2, Issue 1, January 2023, Pages 562–566, https://doi.org/10.1093/rasti/rzad038

Doctoral Thesis, L'université Grenoble Alpes, 2023